

Infrared and Ultraviolet Star Formation in Brightest Cluster Galaxies in the ACCEPT Sample

Aaron S. Hoffer

Michigan State University, Physics & Astronomy Dept., East Lansing, MI 48824-2320

`hoffer.aa@msu.edu`

Megan Donahue

Michigan State University, Physics & Astronomy Dept., East Lansing, MI 48824-2320

`donahue@pa.msu.edu`

Amalia Hicks

Michigan State University, Physics & Astronomy Dept., East Lansing, MI 48824-2320

`hicksam@msu.edu`

R.S. Barthelemy

Western Michigan University, Physics Dept., Kalamazoo, MI 49008-5252

`ramon.s.barthelemy@wmich.edu`

ABSTRACT

We present infrared (IR) and ultraviolet (UV) photometry for a sample of brightest cluster galaxies (BCGs). The BCGs are from a heterogeneous but uniformly characterized sample, the Archive of *Chandra* Cluster Entropy Profile Tables (ACCEPT), of X-ray galaxy clusters from the *Chandra* X-ray telescope archive with published gas temperature, density, and entropy profiles. We use archival *Galaxy Evolution Explorer* (*GALEX*), *Spitzer* Space Telescope, and Two Micron All Sky Survey (*2MASS*) observations to assemble spectral energy distributions (SEDs) and colors for BCGs. We find that while the SEDs of some BCGs follow the expectation of red, dust-free old stellar populations, many exhibit signatures of recent star formation in the form of excess UV or mid-IR emission, or both. We establish a mean near-UV (NUV) to *2MASS* K color of 6.59 ± 0.34 for quiescent BCGs. We use this mean color to quantify the UV excess associated with star formation in the active BCGs. We use both fits to a template of an evolved stellar population and library of starburst models and mid-IR star formation relations to estimate the obscured star formation rates. We show that many of the BCGs in X-ray clusters with low central gas entropy exhibit enhanced UV (38%) and

mid-IR emission (43%) from 8-160 microns, above that expected from an old stellar population. These excesses are consistent with on-going star formation activity in the BCG, star formation that appears to be enabled by the presence of high density, X-ray emitting intergalactic gas in the the core of the cluster of galaxies. This hot, X-ray emitting gas may provide the enhanced ambient pressure and some of the fuel to trigger the star formation. This result is consistent with previous works that showed that BCGs in clusters with low central gas entropies host H α emission-line nebulae and radio sources, while clusters with high central gas entropy exhibit none of these features. *GALEX* UV and *Spitzer* mid-IR measurements combined provide a complete picture of unobscured and obscured star formation occurring in these systems. We present IR and UV photometry and estimated equivalent continuous star formation rates for a sample of brightest cluster galaxies.

Subject headings: galaxies: elliptical and lenticular, cD

1. Introduction

The basic story underlying our current models for the formation of galaxies and clusters of galaxies is that baryonic matter falls into dark matter potential wells, cools to make cold molecular clouds, which then form stars and supermassive black holes. The state of the gas as it falls, the morphology of the accretion, the source of the dust that catalyzes formation of molecular clouds, the physical processes determining the gas temperatures and phases are all uncertain. Simply put, we do not know the full story of how intergalactic gas eventually forms stars and black holes.

Brightest Cluster Galaxies (BCGs) provide unique opportunities for the investigation of the role of hot intergalactic gas in galaxy formation, and in particular its role in affecting the evolution of the star formation and active galactic nucleus (AGN) activity in the central galaxy in the most massive dark matter halos in the universe. The intergalactic gas bound to a massive cluster of galaxies – its intracluster medium (ICM) – outweighs the stars in those galaxies by a factor of 5-10 (e.g., David et al. 1990; Arnaud et al. 1992; Gonzalez et al. 2007). The BCGs in the centers of X-ray clusters where the gas has a short cooling time (or equivalently, low gas entropy) exhibit signs of activity (e.g. radio sources, emission-line nebulae, excess blue or ultraviolet light) that are rare in BCGs in other clusters of galaxies (Hu et al. 1985; Burns 1990; Cavagnolo et al. 2008; Rafferty et al. 2008; Sanderson et al. 2009; Sun 2009). The activity in the BCGs of this category of clusters has been presented as evidence that hot ICM condenses into cold dusty gas that subsequently forms stars. Such BCGs may be hosting real-life versions of late-time ($z < 1$) accretion onto supermassive black holes in central galaxies; but the role of the hot ICM in AGN or star formation activity is not entirely clear.

The simplest hypothesis for how hot gas cools when it is confined to a massive dark halo fails. The first X-ray observations of the ICM in galaxy clusters indicated that some clusters have

a high central gas densities and central cooling times shorter than the age of the universe (e.g., Fabian & Nulsen (1977); Cowie & Binney (1977)). In this scenario, such gas cools slowly, loses pressure support, compresses, allowing gas from the outer parts of the cluster to settle gently into the center. The inferred mass accretion rates could be as large as $1000 M_{\odot} \text{ yr}^{-1}$ (Fabian 1994). Such clusters were dubbed "cooling flows." However, higher resolution X-ray spectroscopy showed that the luminous emission lines one would expect from gas cooling smoothly from 10^8 K to non-X-ray emitting temperatures were not present (Peterson et al. 2003). Nevertheless, such clusters do exhibit cool cores with radii $\sim 50 - 100 \text{ kpc}$, where $kT_{\text{core}} \sim 1/2 - 1/3$ of that found in the outer radii. These clusters are now often called "cool core" clusters.

With spatially resolved X-ray spectroscopy, cool core clusters can be classified by the distribution of gas entropy of the galaxy cluster. The cluster entropy is a thermodynamic quantity. Conveniently, in a gas of pure hydrogen emitting thermal bremsstrahlung radiation, the cooling time can be written down solely in terms of the gas entropy. The gas entropy S is proportional to the logarithm of the quantity $K = T_X n_e^{-2/3}$, conventionally reported in units of keV cm^2 . Donahue et al. (2006) radially fit entropy profiles with a functional form $K(r) = K_0 + K_x (r/r_x)^\alpha$, where K_0 is the central entropy in excess above the power law fit. Cavagnolo et al. (2008) extended this procedure to the entire *Chandra* archive, creating the Archive of *Chandra* Cluster Entropy Profile Tables¹ (ACCEPT). Galaxy clusters with high central entropy often contain quiescent brightest cluster galaxies (BCGs) or exhibit evidence for significant merger or interactions. The empirical boundary between clusters which occasionally host active BCGs and clusters which never host them is $K_0 \sim 30 \text{ keV cm}^2$, an entropy associated with an ICM cooling time of $\sim 1 \text{ Gyr}$ (Voit et al. 2008). Furthermore, about 70% of the BCGs in those cool core clusters host radio sources, and about half of those host extended emission-line nebula characteristic of low-ionization nuclear emission-line regions (LINERs; but are more extended) (Heckman et al. 1989; Crawford et al. 1999; Donahue et al. 2010). Cavagnolo et al. (2008) and Rafferty et al. (2008) have shown that only those BCGs inhabiting clusters with low central gas entropies (short central gas cooling times, high central gas densities) present low-ionization emission-line nebulae ($\text{H}\alpha$), blue gradients, or radio sources.

In this paper, we look for signatures strongly associated with star formation, ultraviolet (UV) excesses and mid-infrared (mid-IR) emission from dust, in the ACCEPT sample of well-studied X-ray clusters. Since even an evolved stellar population emits some UV (and mid-IR), we characterize the stellar content of the BCG using Two Micron All Sky Survey (*2MASS*) K-band photometry and photometry from the IRAC instrument on the *Spitzer* Space Telescope, short-wavelength 3.6 and 4.5 micron bands, where available. To estimate the contribution of recent star formation we measure the ultraviolet (UV) emission with the *Galaxy Evolution Explorer* (*GALEX*) observations. The UV samples the peak of emission in short-lived O and B stars, thus tracking recent, unobscured star formation. Most of the star formation in the universe occurs hidden within cold, dusty

¹<http://www.pa.msu.edu/astro/MC2/accept/>

molecular clouds. The dust in these clouds absorbs the UV and optical light of buried stars and re-emits this light as mid-IR thermal radiation typical of dust at ~ 100 K. Some of this reprocessed emission emerges in the form of features, such as the emission complexes associated with polycyclic aromatic hydrocarbons (PAHs) (Donahue et al. 2011). Puzzlingly, powerful H_2 features appear to be nearly ubiquitous in systems with $\text{H}\alpha$ nebulae, at levels unlikely to be associated with typical star formation processes (Elston & Maloney 1994; Jaffe & Bremer 1997; Donahue et al. 2000, 2011; Egami et al. 2006). Even colder dust (20-30K) in the far-IR has been seen with *Herschel* (Edge et al. 2010a)(Edge et al. 2010b), and Edge (2001) detected significant masses of CO.

The measurements of star formation in BCGs based on UV or mid-IR information to date have been relatively limited. For example, Catinella et al. (2010) report that star formation efficiency varies little over a wide range of galaxy masses in a massive galaxy sample. However, while that sample includes 190 massive galaxies observed with *GALEX* and *Arecibo*, it has very few BCGs. Donahue et al. (2010) assessed the UV properties of the BCGs in a representative sample of 30 X-ray selected clusters from the Representative XMM-Newton Cluster Structure Survey (REXCESS) (Böhringer et al. 2007), while most UV studies are of a limited set of the most extreme emission-line BCGs (e.g., Hicks et al. 2010; O’Dea et al. 2010). Quillen et al. (2008) and O’Dea et al. (2008) studied 62 BCGs with *Spitzer*, selected for their luminous $\text{H}\alpha$. To expand upon these studies, we present an assessment of the UV, near-IR and mid-IR properties of BCGs in a well-studied sample of X-ray clusters. This sample is larger and more diverse than previous studies, as it includes quiescent BCGs along with the most extreme cool-core BCGs. In Section 2 we briefly describe the original X-ray cluster sample, and give an overview of the *GALEX* and *Spitzer* observations. We describe how the BCGs are identified. In Section 3 we discuss the data reduction process for the images in the *Spitzer*, *GALEX*, and *2MASS* archives. Our discussion and analysis of the data is in Section 4. We present estimates of the equivalent continuous UV and IR star formation rates in this section. UV colors are compared to those in Wang et al. (2010). We present a summary of the observations, detections, and emission excesses in Table 1. We conclude the paper in Section 5. For all calculations the assumed cosmology is $H_0 = 70 \text{ km s}^{-1} \text{ Mpc}^{-1}$, $\Omega_M = 0.3$, $\Omega_\Lambda = 0.7$.

2. Observations

2.1. *Chandra* X-Ray Observations

The original galaxy cluster sample is from the ACCEPT database (Cavagnolo et al. 2009), which includes 239 galaxy clusters. This sample is a selection of all galaxy clusters in the *Chandra* archive as of August 2008 that met a minimum flux criterion. The clusters were selected to construct entropy profiles and provide central entropy estimates. To be able to accurately measure the entropy profiles, temperature gradients were required to have a precision better than $\Delta kT_X \approx \pm 1.0$ keV. Cavagnolo et al. (2009) therefore required at least three concentric annuli with a minimum of 2500 counts each. The search resulted in 317 observations of 239 galaxy clusters. Six groups from the flux-

limited Highest X-ray Flux Galaxy Cluster Sample (HIFLUGCS) sample (Reiprich & Böhringer 2002) were added to the collection and a number of clusters with analysis complications were removed. (All additional objects are listed in Cavagnolo et al. (2009).) This sample is not a formally complete sample, but, by and large, these clusters were not selected to be included in the Chandra program because of the UV and mid-IR properties of their brightest cluster galaxies. An interestingly large fraction of these clusters now have been observed by GALEX and Spitzer, and so the time is right for a uniform analysis of the X-ray, UV, and mid-IR properties of the BCGs in the sample.

2.2. *2MASS* Observations - BCG identification

We used the *2MASS* archive and previous literature to determine the locations of the the BCGs in these galaxy clusters (Table 2). The brightest cluster galaxies were initially identified by their *2MASS* position. The locations of the BCGs were determined using a visual inspection (including source brightness and morphology) with *2MASS* J-band images $5' \times 5'$ in size centered on the X-ray centroid to determine the brightest galaxy in the cluster. This visual inspection was followed up with NASA/IPAC Extragalactic Database (NED)² and the Set of Identifications, Measurements, and Bibliography for Astronomical Data (SIMBAD)³ object searches within $2'$ of the X-ray centroid to verify the redshifts of the candidate BCGs. All objects in the *2MASS* Extended Source Catalog (Jarrett et al. 2003) were checked for redshift information and any other indication that they are the brightest galaxy in the cluster. Some BCGs were too distant to have associated *2MASS* catalog entries. The BCGs of these distant clusters were identified using a literature search for journal articles indicating the location of the BCG in the cluster, and are named by their right ascension and declination. For the clusters in the Sloan Digital Sky Survey (SDSS) footprint, color information and brightness in the optical (u'g'r'i'z') from the data release 7 (DR7) were used to verify the BCG selections (Leisman et al. 2011). In a small number of cases we revised the original selection of *2MASS* location (Abell 2034, RXJ1022.1+3830, 4C+55.16, Abell 2069, Abell 368, and Abell 2255). Table 2 gives each cluster and the *2MASS* coordinate for the brightest cluster galaxy.

In Table 3 we list the physical separation of the BCGs from the X-ray centroid of their host galaxy clusters. While most BCGs lie near the X-ray centroid of their galaxy cluster, consistent with their identification as cD galaxies, there are a few that are very far from the center. The physical distance between the X-ray centroid and the BCG is plotted as a histogram in Figure 1. The BCG we identified is twice as likely to be within 10 projected kpc of its X-ray centroid in low entropy clusters (74%) compared to high entropy clusters (37%). Note that all BCGs in a low K_0 system are within 40 kpc of their cluster's X-ray centroid.

²<http://nedwww.ipac.caltech.edu/>

³<http://simbad.u-strasbg.fr/simbad/>

2.3. *GALEX* Observations

The Galaxy Evolution Explorer (*GALEX*) obtains images in the near UV (NUV) at $\lambda_{eff} = 2267 \text{ \AA}$ (bandpass with a full width at half maximum (FWHM) of 269 \AA) and the far UV (FUV) at $\lambda_{eff} = 1516 \text{ \AA}$ (FWHM of 616 \AA) (Martin et al. 2005). There are a total of 168 BCGs in our initial sample with *GALEX* observations in the *GALEX* archive as of 2011 October. We then searched the *GALEX* Release Six (GR6) catalog for a UV source within $5''$ of the *2MASS* BCG location. In the cases where there were multiple observations, the observation with the highest signal to noise was used. Table 2 gives the *GALEX* object identifiers for each BCG detected. Note that not all observations will have an object identifier as the BCG may have gone undetected in the *GALEX* archive.

2.4. *Spitzer* Observations

We analyzed archival *Spitzer* Infrared Array Camera (IRAC) and the Multiband Imaging Photometer for SIRTf (MIPS) observations. IRAC has four near infrared wavebands at 3.6 , 4.5 , 5.8 , and $8.0 \mu\text{m}$ (Fazio et al. 2004). MIPS (Rieke et al. 2004) operates in the mid-IR and has three wavebands at 24 , 70 , and $160 \mu\text{m}$. The *Spitzer* imaging observations selected for analysis were aimed within $1'$ from the X-ray centroid. The Astronomical Observing Request (AOR) numbers are given in Table 2. There are 79 brightest cluster galaxies in ACCEPT with IRAC observations and 100 ACCEPT BCGs with MIPS observations as of 2010 December.

3. Aperture Photometry and Colors

3.1. *GALEX* UV Photometry

We used *GALEX* aperture photometry provided in the *GALEX* catalog and GALEXView⁴. We chose apertures to match *GALEX* measurements and derive colors with photometry from other catalogs (e.g. *2MASS*, SDSS) and with our *Spitzer* aperture photometry. The optimal aperture for the UV is determined by comparing the estimate of the total flux given in GALEXView to the circular aperture flux. The circular aperture chosen is the one with the flux measurement nearest to the estimated total flux value. For most BCGs the two largest aperture radii ($12.8''$ and $17.3''$) were used. The minimum allowed aperture radius was $9.0''$ to avoid aperture correction (the FWHM of *GALEX* observations are $\sim 4.5''$ - $6''$). The *GALEX*-detected UV emission is usually centrally concentrated so generally, the UV emission lies within a radius of $9''$ even when the angular size, as seen in the optical, of the galaxy is larger. Therefore, the *GALEX* aperture size is an approximate upper limit on the size of the UV star formation region. Some of the UV

⁴<http://galex.stsci.edu/GalexView/>

light is produced by evolved stars (e.g., O’Connell 1999) so we use the NUV-K color to estimate how much UV comes from recent star formation. We make photometric measurements within sufficiently large apertures to minimize the degree to which aperture corrections could affect our conclusions. The magnitudes are converted from the magnitudes given in the *GALEX* catalog to AB magnitudes using zeropoints of 20.08 magnitudes for the NUV and 18.82 magnitudes for the FUV (Morrissey et al. 2007). The Galactic extinction corrections are applied from Schlegel et al. (1998) assuming a ratio of 3.1 for A_V/E_{B-V} . The NUV correction assumed is $3.25A_V$ and the FUV correction is $2.5A_V$. UV photometry is presented in Table 4.

3.2. *GALEX* UV Upper Limits

To estimate the detection threshold for *GALEX* observations, we evaluated the cataloged fluxes of all the well-detected sources with a magnitude error < 0.35 ($S/N \gtrsim 3$) within 1° of the BCG targets. Our *GALEX* upper limits are based on detections of peaked sources, i.e. point sources and compact emission regions. A uniform, extended source that fills the aperture will have a higher detection threshold than this estimate. We plot these fluxes as a function of their individual exposure times in Figure 2. The estimated detection threshold is inferred from the upper envelope of these points, which is approximated here by curves $\propto t^{1/2}$. For the exposure times typical of the all-sky imaging survey (AIS) the estimate for the upper limit in AB magnitudes is $19 + 1.25 \times \log t_{NUV}$ for an exposure time t_{NUV} in seconds. Similarly the function for AB magnitude upper limit for the FUV is $18.5 + 1.25 \times \log t_{FUV}$. This relation underestimates the *GALEX* sensitivity for longer exposure times, longer than ~ 500 seconds. There are 9 BCGs (Abell 2319, 3C 295, Abell 611, Abell 665, Abell 1942, Abell 2631, CL J1226.9+3332, HCG 62, and Abell 2219) which had UV exposure times greater than 500 seconds and have a nondetection. For these objects we looked in the field and set the upper limit to be equal to the dimmest source that was detected (with a magnitude error less than 0.35). We report this estimated 3σ upper limit for all cases where the BCG was undetected and when the *GALEX* source flux had a large error (> 0.35 mag), indicating a highly uncertain detection. For BCGs with NUV upper limits, the *2MASS* fluxes are matched with a $7''$ aperture such that they are similar in size to the *GALEX* PSF.

3.3. *Spitzer* Near and Mid IR Photometry

For the vast majority of the observations, *Spitzer* photometry was measured from the final pipeline product post-Basic Calibration Data (pbcd). The pipeline data were flux calibrated in units of MJy steradian $^{-1}$ (Reach et al. 2005) from the IRAC pipeline version S18.7.0 and the MIPS pipeline version 16.1.0. For the four IRAC wavebands, fluxes were measured inside a circular aperture with a radius of $r = 14.3$ kpc h_{70}^{-1} . We wrote an IDL program to perform all aperture flux measurements for *Spitzer* (Donahue et al. 2010). The circular aperture is centered on the BCG location in Table 2. The backgrounds were computed from an annulus with an inner radius of

35'' and an outer radius of 45'' for objects which have an angular radius smaller than 35''. For objects with flux beyond the nominal aperture, the background was computed with an annulus with an inner radius of $1.1\times$ the radius for the object and an outer radius $1.3\times$ the radius of the object. To estimate the mean background counts we fit a Gaussian to a histogram of counts per pixel in the background annulus. This procedure provides a background estimate that is robust to possible sources of contamination (e.g. foreground stars) that increase the counts in a small number of background pixels but do not significantly influence the mean of the Gaussian.

Most of the galaxies detected by MIPS are essentially point sources because the FWHM of the point spread function (PSF) for 24, 70, and 160 μm are 6'', 18'', and 40'', respectively. We measure MIPS fluxes using the same IDL code. Since not all of the flux from the PSF falls in the aperture, MIPS aperture fluxes are corrected using the same aperture correction methods in §4.3.4 of the MIPS Handbook⁵. The 24 micron aperture radius is fixed at 13'' with a background annulus of 15-25'' giving a flux correction factor of 1.167. Similarly, the 70 micron aperture radius is fixed at 35'' with a background annulus of 40-60'', and a correction factor, assuming a 30K source, of 1.22. The 160 micron observations were measured at an aperture radius of 40'' with a background annulus of 64-128'', and a correction factor of 1.752 (also assuming a 30K source). We also derived flux estimates using software provided by the *Spitzer Science Center*, APEX in MOPEX (Makovoz & Marleau 2005), to cross-check our aperture flux measurements. The standard input parameters were used and residual images were created to assess whether the source was completely subtracted. For all sources with proper subtraction, the flux measurement from APEX was compared to the aperture measurement and we verified they were consistent within the cited errors. Only the flux values calculated from apertures are included in Table 5. In Table 1 detections and excesses are equivalent for the 70 and 160 micron observations as we do not have an *a priori* belief that quiescent BCGs should exhibit 70 and 160 micron emission.

For the closest and, likely, spatially-extended BCGs, the fluxes from APEX were systematically lower than the aperture flux estimates. To determine whether any BCG had extended emission or contamination from unrelated point sources, we compared aperture-corrected flux measurements with 13'' and 35'' apertures, and we inspected the 24 micron images for point source contamination within the 35'' radius aperture. Visible contamination was classified as either insignificant, because the difference between the two aperture-corrected estimates was smaller than the statistical uncertainty of those fluxes, or significant. We inspected all detections for possible contamination inside 35'' but we only found potential contamination in the annulus between the 13'' and the 35'' radii (i.e. we saw no obvious sources of contamination inside 13''). Therefore, we do not expect contamination to affect the 24 micron point source flux measurements listed in Table 5. However, the existence of any contaminating source seen at 24 microns is flagged for our 70 and 160 micron photometry in Table 5, which uses larger apertures. (Refer to the footnotes in Table 5 for a description of the contamination categories.)

⁵<http://irsa.ipac.caltech.edu/data/SPITZER/docs/mips/mipsinstrumenthandbook/>

BCGs which did not have point source contamination visible at 24 microns but showed an increase in flux over that expected for a point source in the larger $35''$ aperture are considered extended. All the objects which have been identified as such are, unsurprisingly, nearby galaxies. Instead of correcting the fluxes of these objects as if they were point sources at 24 microns, the fluxes for these galaxies are reported for the large apertures we used for the IRAC photometry. (One exception, the BCG NGC 4636, was measured at a $35''$ radius instead because of significant point source contamination beyond this aperture.)

To more directly account for 70 micron contamination, if a 70 micron source was listed as a detection and the 24 micron measurement indicated contamination, the 70 micron image was inspected for contaminating sources. If a 70 micron detected source inside the aperture appears to come from an object other than the BCG (i.e. its centroid is consistent with that of a non-BCG galaxy) then the detection was downgraded to a conservative upper limit. However, these 70 micron upper limits are based on photometry using a smaller, $16''$ aperture radius with the corresponding point source correction of 1.94 to avoid including flux from extraneous point sources in the upper limit. The 70 micron upper limits estimated through this method are noted in the table. There are two BCGs, Abell 2744a and MS 04516-0305, that are contaminated at 70 microns as well as 160 microns. Upper limits for their 160 micron photometry were found using the same $16''$ aperture radius with the corresponding point source correction of 4.697.

The standard photometric error of 5% is used for the IRAC points as the systematic errors were always much larger than the statistical errors. For MIPS the standard errors are 10%, 20%, 20% for 24, 70, and 160 microns, respectively. These standard errors are usually good estimates except in the case of lower S/N detections for which statistical uncertainties are important (i.e. $S/N = 5 - 20$). We report the total errors (including statistical and systematic uncertainties) for MIPS with the flux measurements in Table 5.

For MIPS, upper limits were estimated for detections that are below 5σ . The standard deviation of the observation was calculated in the same manner as Donahue et al. (2010). If the standard aperture flux had a $S/N < 5$ the filtered data were used instead. The background on these data are better controlled, but the MIPS Handbook warns that low surface brightness emission in the filtered data will be lost. Therefore, the filtered data were only used when the standard source detection fell below the 5σ limit. Those filtered images that are still below the 5σ detection threshold were assigned a 5σ upper limit for that detection. If a BCG is undetected with the standard mosaic but is detected ($>5\sigma$) using the filtered data it is considered a filtered detection and is labelled as such in the Table 5. There were many observations that were considered filtered detections in our first pass through the data, but were revised to upper limits because of 70 micron contamination from non-BCG sources.

For a few of the nearest and brightest BCGs there was an issue with the final data products in the *Spitzer* pipeline. In these cases, the BCG contained a spurious point source that was much brighter than the rest of the galaxy. These very bright artifacts proved to not be physical because

the anomalous levels were not detected in the individual BCD frames. We mosaicked the individual BCD frames with the MOPEX software using the standard mosaicking procedure and settings. The new mosaic images did not exhibit the spurious point sources. The fluxes were then calculated from the new images and were in agreement with the original images if the point source was masked out. Those AORs which required remosaicking are noted in Table 2.

3.4. *2MASS* Near IR Observations

2MASS J, H and K fluxes and errors are extracted from the *2MASS* Extended Object Catalog (Jarrett et al. 2003). The catalog provides aperture photometry between $5''$ and $60''$ in radius. For a few large galaxies (e.g. M87, M49, NGC 4696) the aperture photometry was taken from the *2MASS* Large Galaxy Atlas. The measurements were converted from the system’s Vega magnitudes to Janskys using the AB magnitude conversions (0.9, 1.37, and 1.84 mag for J, H, and K bands, respectively) provided in Cohen et al. (2003). We correct *2MASS* magnitudes for Galactic extinction: $A_K = 0.112A_V$, $A_J = 0.276A_V$, $A_H = 0.176A_V$ (Schlegel et al. 1998). In order to derive flux ratios normalized to emission dominated by the old stellar population sampled in the near-infrared, we matched apertures in the near-IR with those at other wavelengths. Therefore we estimated *2MASS* photometry (presented in Table 6) for each source in three apertures: (1) the *GALEX* aperture for $NUV - K$, (2) the IRAC aperture of $r = 14.3h_{70}^{-1}$ kpc for IRAC to near-IR flux ratios, and (3) the 24 micron aperture (for K-band only). After extinction and k-correction, Figure 3 shows that the BCGs have no trend in their K band luminosity (the mean is $1.6_{-0.4}^{+0.7} \times 10^{44}$ erg s $^{-1}h_{70}^{-2}$) as a function of redshift or K_0 of these galaxy clusters.

4. Discussion

4.1. UV Excess and Color

The UV excess is determined by comparing $NUV - K$ colors, plotted in Figure 4 against excess entropy K_0 from Cavagnolo et al. (2009). The baseline for quiescent BCGs is visible in this figure. The BCGs with excess UV emission, over and above the UV found in quiescent BCGs, are only in the low K_0 galaxy clusters in the ACCEPT sample. While we find no BCGs with excess UV emission in galaxy clusters with high central entropy, there are many quiescent BCGs in low central entropy clusters. From our sample we estimate the typical $NUV - K$ color for quiescent BCGs from the mean and standard deviation of all BCGs with central entropies above 30 keV cm^2 . We derive a mean color of inert BCGs is 6.59 ± 0.34 . In contrast, the mean color for BCGs in clusters with central entropies less than 30 keV cm^2 is 6.11 ± 0.99 . We define a color excess $\Delta_c = 6.59 - (NUV - K)$. This excess will be used in § 4.3 to estimate the equivalent continuous star formation rate. The color excess is simply defined such that blue light in excess of quiescent BCGs in high entropy clusters can easily be translated into a UV luminosity associated

with continuous unobscured star formation. BCGs are considered to have a NUV excess in Table 1 if their NUV-K color is at least 1σ bluer than the mean color of inert BCGs. We see that 38% of low central entropy clusters in our sample have a NUV-K excess. The BCGs with the bluest colors are in Abell 426, Abell 1664, and RX J1504.1-0248 which have colors around 3.0.

We plot the $FUV - NUV$ and $NUV - K$ colors for BCGs in Figure 5. Contamination from line emission from $Ly\alpha$ may occur if the redshifted $Ly\alpha$ line is included in the FUV bandpass (within the FWHM (269 Å) of the effective wavelength (1516Å) of the FUV filter), at redshifts between 0.15 – 0.36. The right figure plots only nearby BCGs ($z < 0.15$) to address this possible effect. Excluding the BCGs which may be contaminated by line emission ($z > 0.15$), we do not detect a significant FUV-NUV color difference between bluer BCGs (with NUV-K colors less than 6.3) and redder BCGs (with NUV-K colors greater than 6.3). The mean of the FUV-NUV color for bluer BCGs is 0.73 ± 0.57 while the mean of redder BCGs is 0.79 ± 0.30 .

Wang et al. (2010) uses GALEX and SDSS to measure colors on a sample of 113 nearby ($z < 0.1$) optically selected BCGs and compare them to a sample of field galaxies. Also, they compare their results to a sample of 21 X-ray selected BCGs from Rafferty et al. (2008) which included BCGs in both cool-core and non-cool-core clusters. From Figure 7 in Wang et al. (2010), the distribution of the FUV-NUV color is consistent with ours with a mean that better matches the photometry from their outer apertures (radius covers 90% of the light) than that measured within their inner apertures (radius covers 50% of the light). Similarly, their NUV-r colors are consistent with our NUV-K colors, after transformation between SDSS r and 2MASS K bands, assuming those bands are only affected by emission from the old stellar population.

4.2. IR Color

The ratios of 8.0 to 3.6 micron fluxes track the ratios of infrared emission from polycyclic aromatic hydrocarbons (PAHs), stochastically heated hot dust grains, and possibly rotationally excited molecular hydrogen and other emission lines (e.g., Donahue et al. 2011) to emission from stars. We plot these ratios as a function of redshift in Figure 6. The line shows the expectation for a passively evolving stellar population with an age of 10 Gyr at $z = 0$. After normalizing the ratio for the stellar population, we determine the total number that are at least 1σ above the normalized mean for BCGs in high K_0 clusters (1.014 ± 0.061) and refer to those as BCGs with excess 8.0 micron emission in Table 1. The points that lie well above this line are likely to have some form of hot dust and/or PAH emission as the observed IRAC 8.0 micron color is sensitive to only strong PAH features. In Figure 7 the IRAC ratio of 4.5 to 3.6 micron fluxes from *Spitzer* are plotted against redshift, similarly to the plot from Quillen et al. (2008). Similar to what we have done for the 8.0 to 3.6 micron ratio, we normalize the 4.5 to 3.6 micron ratio for a passively evolving stellar population with an age of 10 Gyr at $z = 0$. We then determine a mean of the normalized ratio for BCGs in high K_0 clusters (1.048 ± 0.019). All BCGs at least 1σ in excess of the mean are considered to have excess 4.5 micron emission.

For both the 8.0 to 3.6 micron flux ratio and the 4.5 to 3.6 micron flux ratio, the only BCGs with excesses over and above a passively evolving old stellar population are those that inhabit clusters with low central entropies, as shown in Figure 7 and Figure 6. In Figure 8 the 8.0 to 3.6 micron ratio and the 4.5 to 3.6 micron ratio are strongly correlated ($r = 0.92, 15\sigma$ for objects with mid-IR detections and/or NUV-K excesses), which is expected if the excess 4.5 micron emission is generated by processes related to that producing the 8.0 micron emission. The functional fit plotted is

$$\log_{10}(F_{8.0\mu\text{m}}/F_{3.6\mu\text{m}}) = (0.153 \pm 0.002) + (5.422 \pm 0.021) \times \log_{10}(F_{4.5\mu\text{m}}/F_{3.6\mu\text{m}}). \quad (1)$$

Both the ratios have been normalized for passive evolution. As long as the IRAC calibration was consistent over time, these are precise relative flux ratios, independent of the flux calibration. The absolute flux ratios are precise to about 2%. The 8.0 and 4.5 micron bandpasses will include PAH and mid-IR emission line features associated with activity seen in cool core BCGs (Donahue et al. 2011). The emission of dust-free, evolved stellar populations in these same bandpasses is similar to the Rayleigh-Jeans tail of a black body, decreasing steeply to longer wavelengths. We see two BCGs HCG 62 and Abell 1644 that show an excess in both normalized ratios however neither shows a NUV-K excess. Abell 1644 was not observed in MIPS and we expect to see a detection in the 70 micron waveband based on this correlation. HCG 62 has a 70 micron upper limit which may be related to the selection effect that it is a very low K_0 galaxy group.

We assess the presence of a luminous dust component, likely to be obscured star formation but also could be contributed by an AGN, by looking at the 24 micron to K-band (2.2 micron) flux ratio plotted against the central entropy in Figure 9. We note a similar pattern here as found in the UV excess plots (Figure 4), that the low K_0 galaxy clusters are far more likely to host BCGs with warm dust. The possible exception to this pattern is Abell 521, which is a high entropy cluster with an elevated 24 micron to K band flux ratio. However, as seen in Ferrari et al. (2006) there is a low entropy, compact, X-ray corona (Sun et al. 2007) (i.e. a “mini-cooling core”) around the BCG in Abell 521, embedded in a cluster with otherwise high entropy. Excess 24 micron emission is estimated by determining the mean of the 24-K ratio of BCGs in high K_0 systems (excluding Abell 521) and any BCG with at least 1σ above this mean (0.063 ± 0.050) is considered to have excess 24 micron emission. We see that 43% of the cool cores in our sample have an excess in their 24 micron to K band ratio. The BCGs with the most extreme 24 micron to K band ratios are in ZwCl 0857.9+2107 and Cygnus A with a ratio of about 20. BCGs in Abell 426 and Abell 1068 also have large ratios around 10. All four objects likely have some AGN contribution. We see the scatter (i.e. standard deviation) in the ratio $\log_{10}(F_{24\mu\text{m}}/F_K)$ is 0.81 for BCGs in low central entropy clusters.

We can compare IR ratios in BCGs to those of normal star-forming galaxies and starbursts, similar to Figure 1 in Johnson et al. (2007a). The ratios for the BCGs are plotted in Figure 10 as well as the SINGS galaxies (Kennicutt et al. 2003). Similar to their sample of a wide range of galaxies, the BCGs in our sample have the same colors as star-forming galaxies in SINGS. We note that some of the nearby BCGs have a higher ratio of 8 micron to 24 micron emission by a

factor of 2. This ratio may indicate a relatively larger contribution from PAH emission over very warm dust. Also, this bandpass may include contributions from the S(4) transition of molecular hydrogen. Rotationally excited molecular hydrogen lines are extremely luminous in some BCGs, and these same lines are not bright in star forming galaxies (Donahue et al. 2011). It is possible that some of the excess emission at the 8.0 micron may be contributed by molecular hydrogen.

4.3. Star Formation Rates (SFRs)

The UV color excess, Δ_c defined in § 4.1, can be used to estimate the excess UV luminosity due to unobscured star formation:

$$L_{\text{SFR}} = L_\nu(1 - 10^{-\Delta_c/2.5}), \quad (2)$$

where the specific luminosity L_ν is converted from the NUV AB magnitude, corrected for Galactic extinction. The NUV k-correction for a star forming spectrum is negligible out to moderate redshifts (Hicks et al. 2010). The unobscured star formation rate is then estimated from the relation in Kennicutt (1998) and listed in Table 7. The total UV luminosity is estimated to be $L_{\text{UV}} \sim \nu L_\nu$ using $\nu = c/2267\text{\AA}$. Upper limits are based on 3σ uncertainties in UV excesses.

The obscured star formation rate is estimated in two ways, (1) by fitting Groves et al. (2008) starburst models and a model of an old stellar population to the *2MASS* and *Spitzer* IRAC/MIPS infrared data points, and (2) from using calibrated conversions of IR luminosity (mostly 24 and 70 micron luminosities) to SFRs. In the first case, we present a sum of the two models, with independent normalizations. Star formation rates were determined for all BCGs with data from at least *2MASS* and the 24 μm band of MIPS. To estimate rest-frame IR luminosities based on the 24 and 70 micron fluxes, k-corrections were applied such that $L_{\text{rest}} = kL_{\text{obs}}$. The corrections were found using the best-fit Groves model for that individual galaxy and convolving it with the MIPS bandpass, both in the rest frame and the observed frame of the galaxy. The actual 70 micron corrections do not depend very much on the specific Groves starburst model. However, the 24 micron point usually falls around a minimum in the spectrum, which causes a larger scatter in the relation for a give redshift (up to 30%) The 24 micron k-corrections are in the range (0.125-1.056), the 70 micron k-corrections are in the range (0.738-1.879). The total IR luminosity, L_{dust} , is estimated by integrating the total scaled starburst model over $\lambda\lambda 8\text{-}1000\mu\text{m}$. We plot the UV star formation rate against the IR star formation rate in Figure 11.

Calibrated conversions for star formation rates from 24 and 70 micron luminosities were used from Calzetti et al. (2010). The 70 micron luminosity conversion to a SFR was from Equations (21) and (22) from this paper, depending on the luminosity of that galaxy. The 24 micron SFR relation was from Equation (6) which is from Wu et al. (2005). From Figure 12 we have a comparison between these conversions and the model calibrated star formation rate. The 24 micron luminosity

is not as good at predicting the bolometric IR luminosity (and the integrated star formation) because it does not sample as close to the cold dust mid-IR emission peak as the 70 micron luminosity. The 70 micron flux is much closer to the peak and is likely a better estimate of the IR luminosity and the obscured SFR.

We estimate the IR excess $IRX = \log_{10}(L_{\text{dust}}/L_{\text{UV}})$ and plot it against the $FUV - NUV$ color (Figure 13), similar to Figure 6 in the Johnson et al. (2007a) paper, which presents UV and IR data for a sample of star-forming disk galaxies and starburst galaxies. In an earlier comparison of BCGs with star-forming galaxies, Hicks et al. (2010) found that the cool core BCGs in their sample tended to be bluer in UV color and have a large scatter in IRX compared to those properties in the galaxies in Johnson et al. (2007a). We do see the larger scatter in IRX for those BCGs that have a bluer UV color. We note that most of the BCGs in our plot are found in low central entropy clusters because those are the only BCGs with FUV, NUV, and *Spitzer* mid-IR detections.

4.4. Star Formation and Cluster Entropy Profiles

We have shown here and in previous works (e.g., Cavagnolo et al. 2008, 2009; Rafferty et al. 2008), that BCGs in clusters with low central entropy (K_0) are the only BCGs to exhibit signs of vigorous star formation. The upper threshold for activity in BCGs appears to be around 30 keV cm^2 . Table 1 presents the subsamples with excess emission. We investigate here to see whether the strength of the signatures of activity, the UV and mid-IR excess, exhibited any trend with the central entropy floor or other cluster property.

Here we take the derived star formation rates as simply indicative of the level of star formation activity. By assuming the star formation is constant, we have taken a nominal assumption about the conversion factors and the starburst models, and translated luminosities into SFRs. We are not claiming that the star formation is continuous. Distinctions between continuous star formations, simple single-burst models of a single age, and convolutions of more complicated star formation histories are well beyond the scope of broad-band photometric data and global measurements. For example, extremely recent star formation is best tracked with $H\alpha$, but the $H\alpha$ fluxes available from the literature are typically from long-slit spectra, and therefore can underestimate emission line flux if some of it is located outside the central $2''$ or so. $H\alpha$ can also be affected by dust extinction in heavily obscured regions; $H\alpha$ can be produced by mechanisms other than by recombination in star formation regions. Mid-IR emission provides a pretty reliable assessment of the obscured star formation energy output, since it is like a bolometric measure of luminosity emitted by dust. At low star formation rates, the colder dust, heated by evolved stars can contribute to the longer wavelength emission, so the lowest IR SFRs in our sample (below about 0.1 solar masses per year) may be regarded as upper limits. The UV light from a galaxy is very sensitive to the presence of hot stars if some of their light escapes the galaxy. We do not attempt to correct the UV light for internal extinction, so the UV and the mid-IR are sampling complementary components of any star formation-related light.

A sum of the UV and IR SFRs is therefore a best estimate of something akin to the total star formation rate of the BCG, and even the most conservative interpretation is that they indicate the current luminosity of star formation in the BCG. We do not see any correlation between the entropy profile and the strength of star formation signatures (e.g. the UV or the mid-IR luminosities of the BCGs with various X-ray gas quantities, K_0 or the value of the entropy profile at 20 kpc ($K(r = 20 \text{ kpc})$)). In Figure 14 we plot the quantities of SFR and K_0 . Upon first glance, there may seem to be a trend for the detected lowest entropy systems to have the lowest star-formation luminosities. However, these are lowest redshift groups in the ACCEPT sample, with lower luminosities and masses overall. They are quite nearby, so the ones that are well-observed by Chandra have entropy profiles that probe the sub kpc-scales. Excluding the groups (or including the upper limits for BCGs in groups without evidence for star formation activity) erases any semblance of a trend. To test that we were not missing a trend because the best fit K_0 could be biased high for the more distant clusters (see Cavagnolo et al 2009), we plot K_0 and SFR for the BCGs with z between 0.05 and 0.15. In this subsample, no trend is visible. Furthermore, the expected trend would be that the lowest entropy systems would have the largest star formation luminosities because the gas has the shortest detected cooling times. Therefore we see no evidence for a simple relation between central gas entropy or cooling time and the estimated SFR.

4.5. ICM Gas Cooling and Star Formation in BCGs

While the presence of high density, high pressure intracluster gas seems to be a prerequisite for a BCG to host some star formation, role of the intracluster gas is not quite clear. The current paradigm suggests that some of the hot gas cools and forms stars, but a gas that has been at X-ray temperatures for some time has likely sputtered away any grains it may have had. The lifetime of a typical Galactic dust grain in 10^7 K gas is of order 10 million years (Draine & Salpeter 1979). Dust-free gas forms molecular hydrogen only very slowly (e.g., Bromm et al. 2009). Voit & Donahue (2011) show that for BCGs with measured reservoirs of CO (and H_2), the gas residence time ($= M(\text{H}_2)/\text{SFR}$) for BCGs is very similar to that of star-forming disk galaxies at $\text{SFR} < 10 \text{ M}_\odot \text{ yr}^{-1}$, around a Gyr. For BCGs with rapid SFRs, the residence time is similar to that of starbursts with similar SFRs ($\sim 10^7 - 10^8 \text{ yrs}$). They calculate that if much of the stellar winds and ejecta of evolved stars in the BCG are retained by the BCG, perhaps as a consequence of the higher intracluster pressures, this gas could fuel much of the existing star formation occurring at a steady rate. Certainly for BCGs with $\text{SFR} \sim 10$ solar masses per year or less, the stellar ejecta is a source of material that has mass of similar order of magnitude to any source of cooled ICM gas.

However, for galaxies with gas reservoirs of 10^{10} solar masses or more, cooled ICM appears to be required to supply the molecular clouds. The stellar ejecta or contributions from the ISM of dusty galaxies (e.g. Sparks et al. 1989) may provide dusty seeds that may mix with the ICM and significantly accelerate its cooling. The larger SFRs cannot be sustained at a steady rate, given the gas supply, and just as in starburst galaxies, must be a short-term situation. The gas may

accumulate over a longer period. Given that $\sim 1/3$ of low redshift cool core galaxies exhibit $H\alpha$, a similar fraction of cool core BCGs (or possibly fewer, if some of the $H\alpha$ emission is not related to SF) are in the star-forming state. Therefore, such galaxies could accumulate the ejecta of their stellar inhabitants into molecular clouds for Gigayears, then experience a burst once a threshold surface density of molecular hydrogen was achieved.

The empirical correlation between the presence low-entropy ICM and the star formation in the central BCG is incontrovertible. However, the common interpretation of this correlation that cooled ICM fuels the star formation has not been backed up by a physically plausible theory for how the hot ICM cools and makes cold and dusty molecular clouds. The resident stellar population is an obvious source of dust (and cool gas) that should not be neglected.

5. Conclusions

We present photometry for brightest cluster galaxies in the ACCEPT cluster sample, derived from *GALEX*, *Spitzer*, and *2MASS* archival observations. This sample includes 239 clusters which were well-observed by Chandra up until late 2008, with hot gas entropy profiles uniformly extracted (Cavagnolo et al. 2009). We identified the BCGs in all of the clusters. In our BCG identification, it is twice as likely to be within 10 projected kpc of its X-ray centroid in low entropy clusters (74%) compared to high entropy clusters (37%).

Similar to what has been seen in other star formation indicators (e.g. $H\alpha$), galaxy clusters with low central gas entropies (also known as "cool core" clusters) are the only clusters to host BCGs with infrared and UV excesses above those from the old stellar population. The entropy threshold of 30 keV cm^2 is consistent with the entropy threshold identified by other work (Cavagnolo et al. 2008; Rafferty et al. 2008; Cavagnolo et al. 2009). We found 168 observations by the near UV imaging by *GALEX*, of which 112 BCGs were detected. We found a mean NUV-K (6.59 ± 0.34) color seen in quiescent BCGs and use that to quantify excess UV emission in individual BCGs. Of the 84 clusters with low central gas entropy, 32 (38%) hosted BCGs with a UV excess, while none of the clusters with high central gas entropy did. The scatter (i.e. standard deviation) in the NUV-K AB color of BCGs in low entropy clusters is considerably higher at 0.99. We did not detect a difference between the mean UV color (FUV-NUV) of BCGs (not including those with possible $Ly\alpha$ contamination), within the error, for low and high entropy clusters.

Similarly, we detected excess infrared emission in some BCGs in low gas entropy clusters over a large range of infrared bands (e.g. 4.5, 8.0, 24, and 70 microns) and no excess in BCGs in high central entropy clusters. The mid-IR emission ratios for BCGs (including quiescent BCGs with mid-IR detections) are consistent with, and span a similar range to, galaxies studied in the Sloan Digital Sky Survey (SDSS) galaxies with a range of star forming properties by Johnson et al. (2007b). For example, 24 of the observed 56 BCGs (43%) in low entropy clusters show excess 24 micron to K band emission. The standard deviation of the ratio $\log_{10}(F_{24\mu\text{m}}/F_K)$ is 0.81 in these

BCGs. We also see a strong correlation between excess 4.5 micron and 8.0 micron fluxes that may indicate correlated PAH emission in both of these bands, when the PAH emission is strong.

The excess emission seen in the UV can be used in conjunction with the IR emission to estimate a total star formation rate, accounting for both obscured and unobscured star formation. The UV and IR estimates give complementary information whereas $H\alpha$ may be affected by contaminating contributions from other sources (e.g. dust extinction, shocks) or limited by technique (e.g. incomplete spatial coverage in long slit spectroscopy, contamination by N II in narrow band imaging). Additionally, the multi-wavelength coverage (as opposed to single band measurements) can help to further constrain possible sources of the excess emission. We see that the near-IR to far-IR emission is consistent with a combination of a starburst model and an old stellar population. Clear signs of these empirical correlations and significant dust emission in some low entropy clusters can help constrain star formation estimates in these BCGs. Aside from the previously noted upper threshold for activity at $K_0 = 30 \text{ keV cm}^2$, we do not detect a correlation between the level of luminosities or excesses with K_0 (or equivalently, central cooling time.) However, whether the gas fueling this activity comes from cooling of the ICM or other processes, is not so clear. A significant, massive evolved stellar population in these galaxies may produce dusty gas which may be confined by the hot gas and it may provide the seeds of condensation for the gas from the hot, and presumably dust-free, intracluster medium (Voit & Donahue 2011).

Support for this research was provided by *Spitzer* contracts JPL RSA 1377112 (MSU RC065166) and JPL 1353923 (MSU RC065195). M. Donahue and A. Hicks were partially supported by a Long Term Space Astrophysics grant NASA NNG05GD82G (MSU RC062757). We would also like to thank Deborah Haarsma and Luke Leisman for their helpful discussion on BCG identification and Mark Voit for his comments on the text. This research has made use of the SIMBAD database, operated at CDS, Strasbourg, France. This research has made use of the NASA/IPAC Extragalactic Database (NED) which is operated by the Jet Propulsion Laboratory, California Institute of Technology, under contract with the National Aeronautics and Space Administration.

Facility: GALEX, Spitzer (IRAC,MIPS), CTIO:2MASS, FLWO:2MASS

REFERENCES

- Arnaud, M., Rothenflug, R., Boulade, O., Vigroux, L., & Vangioni-Flam, E. 1992, A&A, 254, 49
- Böhringer, H., et al. 2007, A&A, 469, 363
- Bromm, V., Yoshida, N., Hernquist, L., & McKee, C. F. 2009, Nature, 459, 49
- Burns, J. O. 1990, AJ, 99, 14
- Calzetti, D., et al. 2010, ApJ, 714, 1256

- Catinella, B., et al. 2010, MNRAS, 403, 683
- Cavagnolo, K. W., Donahue, M., Voit, G. M., & Sun, M. 2008, ApJ, 683, L107
- . 2009, ApJS, 182, 12
- Cohen, M., Wheaton, W. A., & Megeath, S. T. 2003, AJ, 126, 1090
- Cowie, L. L., & Binney, J. 1977, ApJ, 215, 723
- Crawford, C. S., Allen, S. W., Ebeling, H., Edge, A. C., & Fabian, A. C. 1999, MNRAS, 306, 857
- David, L. P., Arnaud, K. A., Forman, W., & Jones, C. 1990, ApJ, 356, 32
- Donahue, M., de Messières, G. E., O’Connell, R. W., Voit, G. M., Hoffer, A., McNamara, B. R., & Nulsen, P. E. J. 2011, ApJ, 732, 40
- Donahue, M., Horner, D. J., Cavagnolo, K. W., & Voit, G. M. 2006, ApJ, 643, 730
- Donahue, M., Mack, J., Voit, G. M., Sparks, W., Elston, R., & Maloney, P. R. 2000, ApJ, 545, 670
- Donahue, M., et al. 2010, ApJ, 715, 881
- Draine, B. T., & Salpeter, E. E. 1979, ApJ, 231, 77
- Edge, A. C. 2001, MNRAS, 328, 762
- Edge, A. C., et al. 2010a, A&A, 518
- . 2010b, A&A, 518, L47+
- Egami, E., Rieke, G. H., Fadda, D., & Hines, D. C. 2006, ApJ, 652, L21
- Elston, R., & Maloney, P. 1994, in *Astrophysics and Space Science Library*, Vol. 190, *Astronomy with Arrays, The Next Generation*, ed. I. S. McLean, 169–+
- Fabian, A. C. 1994, ARA&A, 32, 277
- Fabian, A. C., & Nulsen, P. E. J. 1977, MNRAS, 180, 479
- Fazio, G. G., et al. 2004, ApJS, 154, 10
- Ferrari, C., Arnaud, M., Ettori, S., Maurogordato, S., & Rho, J. 2006, A&A, 446, 417
- Gonzalez, A. H., Zaritsky, D., & Zabludoff, A. I. 2007, ApJ, 666, 147
- Groves, B., Dopita, M. A., Sutherland, R. S., Kewley, L. J., Fischera, J., Leitherer, C., Brandl, B., & van Breugel, W. 2008, ApJS, 176, 438
- Heckman, T. M., Baum, S. A., van Breugel, W. J. M., & McCarthy, P. 1989, ApJ, 338, 48

- Hicks, A. K., Mushotzky, R., & Donahue, M. 2010, *ApJ*, 719, 1844
- Hu, E. M., Cowie, L. L., & Wang, Z. 1985, *ApJS*, 59, 447
- Jaffe, W., & Bremer, M. N. 1997, *MNRAS*, 284, L1
- Jarrett, T. H., Chester, T., Cutri, R., Schneider, S. E., & Huchra, J. P. 2003, *AJ*, 125, 525
- Johnson, B. D., et al. 2007a, *ApJS*, 173, 377
- . 2007b, *ApJS*, 173, 392
- Kennicutt, Jr., R. C. 1998, *ARA&A*, 36, 189
- Kennicutt, Jr., R. C., et al. 2003, *PASP*, 115, 928
- Leisman, L., Haarsma, D. B., Sebald, D. A., & ACCEPT team. 2011, in *Bulletin of the American Astronomical Society*, Vol. 43, American Astronomical Society Meeting Abstracts #217, #149.08—+
- Makovoz, D., & Marleau, F. R. 2005, *PASP*, 117, 1113
- Martin, D. C., et al. 2005, *ApJ*, 619, L1
- Morrissey, P., et al. 2007, *ApJS*, 173, 682
- O’Connell, R. W. 1999, *ARA&A*, 37, 603
- O’Dea, C. P., et al. 2008, *ApJ*, 681, 1035
- O’Dea, K. P., et al. 2010, *ApJ*, 719, 1619
- Peterson, J. R., Kahn, S. M., Paerels, F. B. S., Kaastra, J. S., Tamura, T., Bleeker, J. A. M., Ferrigno, C., & Jernigan, J. G. 2003, *ApJ*, 590, 207
- Quillen, A. C., et al. 2008, *ApJS*, 176, 39
- Rafferty, D. A., McNamara, B. R., & Nulsen, P. E. J. 2008, *ApJ*, 687, 899
- Reach, W. T., et al. 2005, *PASP*, 117, 978
- Reiprich, T. H., & Böhringer, H. 2002, *ApJ*, 567, 716
- Rieke, G. H., et al. 2004, *ApJS*, 154, 25
- Sanderson, A. J. R., Edge, A. C., & Smith, G. P. 2009, *MNRAS*, 398, 1698
- Schlegel, D. J., Finkbeiner, D. P., & Davis, M. 1998, *ApJ*, 500, 525
- Sparks, W. B., Paresce, F., & Macchetto, D. 1989, *ApJ*, 347, L65

- Sun, M. 2009, *ApJ*, 704, 1586
- Sun, M., Jones, C., Forman, W., Vikhlinin, A., Donahue, M., & Voit, M. 2007, *ApJ*, 657, 197
- Voit, G. M., Cavagnolo, K. W., Donahue, M., Rafferty, D. A., McNamara, B. R., & Nulsen, P. E. J. 2008, *ApJ*, 681, L5
- Voit, G. M., & Donahue, M. 2011, *ApJ*, 738, L24+
- Wang, J., Overzier, R., Kauffmann, G., von der Linden, A., & Kong, X. 2010, *MNRAS*, 401, 433
- Wu, H., Cao, C., Hao, C.-N., Liu, F.-S., Wang, J.-L., Xia, X.-Y., Deng, Z.-G., & Young, C. K.-S. 2005, *ApJ*, 632, L79

Table 1. Summary of Observations and Detections

Waveband	Observations	Observations ($K_0 \leq 30\text{keV cm}^2$)	Detections	Excess
NUV	168	84	112	32 ^a
4.5 micron	76	52	76	13
8.0 micron	76	52	76	43
24 micron	98	56	94	24 ^b
70 micron	65	46	32	32
160 micron	33	21	16	16

^aDefined to be NUV-K color less than 6.25, which is at least one sigma bluer than the mean of the quiescent BCGs.

^bDefined to be a 24 micron to K band ratio greater than 0.113, which is at least one sigma greater than the mean of the quiescent BCGs.

Note. — Refer to appropriate section of text for definitions of Detections and Excess.

Table 2. Brightest Cluster Galaxy Identifications.

Cluster Name	<i>GALEX</i> IAU Name	2MASS ID	IRAC AOR	MIPS AOR
1E0657 56a	...	06 ^h 58 ^m 16 ^s .04, −55°56′36 95″	12674048, 23089920	21981440 ^{a,b} , 23089664 ^a
1E0657 56b	...	06 ^h 58 ^m 35 ^s .16, −55°56′55 8″	12674048, 23089920	21981440 ^{a,b} , 23089664 ^a
2A 0335+096	033840.6+095812 ^c	03384056+0958119	18646528	18636544 ^{a,b}
2PIGG J0011.5-2850 001121.5-285114 ^d , 001121.5-285115 ^c		00112166-2851158
2PIGG J2227.0-3041	222754.3-303433 ^e	22275446-3034321
3C 28.0	005550.4+262438 ^e	00555058+2624366	18648320	18648064 ^{a,b}
3C 295	141120.4+521210 ^c	14112046+5212095
3C 388	184402.5+453329 ^e	18440241+4533298	10925056	4710144 ^{a,b,f} , 21693696 ^a
4C 55.16	...	08345512+5534289
Abell 13	...	00133853-1930007
Abell 68	...	00370686+0909236	...	23434240 ^a
Abell 85	004150.4-091810 ^e	00415052-0918109	18666752	18666496 ^{a,b}
Abell 119	005616.3-011520 ^e	00561610-0115197
Abell 133	010241.5-215252 ^e	01024177-2152557
Abell 141	...	01053543-2437476
Abell 160	011259.8+152929 ^d	01125953+1529283
Abell 193	012507.5+084158 ^c	01250764+0841576
Abell 209	013152.4-133637 ^e	01315250-1336409	12657664, 4755200	4764672 ^a , 4764928 ^a
Abell 222	...	01373406-1259288
Abell 223	...	01375602-1249106
Abell 262	015246.3+360906 ^e	01524648+3609065	18646272	18636288 ^{a,b}
Abell 267	015241.9+010031 ^d	01524199+0100257	12657152, 4755456	4768768 ^a , 4769024 ^a
Abell 368	...	02 ^h 37 ^m 28 ^s .90, −26°30′30 0″	...	23411968 ^a
Abell 370	...	02395273-0134188	12116224, 12116480 4403712, 4403968	11362304 ^{a,f} , 19038464 ^{a,b} 19038720 ^{a,f} , 19038976 ^{a,c} 4745472 ^{a,b,f} , 4766208 ^a , 4766464 ^a
Abell 383	024803.4-033145 ^e	02480342-0331447	12656640, 4755712	23304960 ^a , 4772352 ^a , 4772608 ^a
Abell 399	...	02575308+1301508
Abell 400	025741.5+060136 ^d	02574155+0601371
Abell 401 ^g	025857.6+133457 ^d	02585781+1334583	...	28313856 ^{a,b}
Abell 426	031948.1+413044 ^e	03194823+4130420	10483456 ^h	11153920 ^{a,b} , 21666048 ^a

Table 2—Continued

Cluster Name	<i>GALEX</i> IAU Name	2MASS ID	IRAC AOR	MIPS AOR
Abell 478	...	04132526+1027551	11579904	12417024 ^f 14944256 ^{a,f} , 14944512 ^{b,f}
Abell 496	...	04333784-1315430	11580160	...
Abell 520	...	04541993+0257453
Abell 521	...	04540687-1013247	...	23414016 ^a
Abell 539	051637.1+062651 ^e	05163713+0626526
Abell 562	...	06532152+6919514
Abell 576	072130.2+554539 ^c	07213023+5545416
Abell 586	...	07322028+3138009	...	23302400 ^a
Abell 611	080056.7+360322 ^c	08005684+3603234	...	23302912 ^a
Abell 644	GI3_103005_Abell644 ⁱ	08172559-0730455
Abell 665	083057.5+655029 ^e	08305736+6550299	...	23303424 ^a
Abell 697	084257.6+362201 ^e	08425763+3622000	4752384, 12654080	4769280 ^a , 4769536 ^a
Abell 744	090720.5+163904 ^e	09072049+1639064
Abell 754	090919.3-094159 ^e	09091923-0941591
Abell 773	...	09175344+5143379	12656384, 4753408	4766720 ^a , 4766976 ^a
Abell 907	...	09582201-1103500
Abell 963	101703.6+390250 ^e	10170363+3902500	23908608	...
Abell 1060	103642.6-273137 ^e	10364282-2731420
Abell 1063S	...	22484405-4431507	12655872	12655360 ^a , 12655616 ^a
Abell 1068	104044.5+395710 ^d	10404446+3957117	18650368	18638336 ^{a,b}
Abell 1201	111254.4+132609 ^e	11125450+1326093
Abell 1204	111320.5+173541 ^e	11132052+1735409	18650880	18650624 ^{a,b}
Abell 1240
Abell 1361	114339.3+462121 ^d	11433959+4621202	18651136	18638592 ^{a,b}
Abell 1413	115518.0+232417 ^e	11551798+2324177
Abell 1423	...	11571737+3336399
Abell 1446	120203.4+580205 ^d	12020385+5802081
Abell 1569	123625.8+163220 ^d	12362580+1632181
Abell 1576	...	12365866+6311145
Abell 1644	125711.5-172431 ^d , 125711.3-172431 ^e	12571157-1724344	18662656	...

Table 2—Continued

Cluster Name	<i>GALEX</i> IAU Name	2MASS ID	IRAC AOR	MIPS AOR
Abell 1650	125841.6-014541 ^d	12584149-0145410
Abell 1651	...	12592251-0411460
Abell 1664	130342.5-241442 ^e	13034252-2414428	...	18662400 ^{a,b}
Abell 1689	...	13112952-0120280	14696192, 14696448, 14696704 14697472, 25411840, 4754176 14696960, 14697216	19042048 ^b , 19042304 ^f 4769792 ^a , 4770048 ^a
Abell 1736	132648.6-270837 ^e	13264872-2708378
Abell 1758	...	13323845+5033351	4752640, 12654848	23304192 ^a , 4763136 ^a , 4763392 ^a
Abell 1763	133520.1+410004 ^e	13352009+4100041	14790144	14790912 ^{a,b,f} , 14791168 ^{a,b,f} , 14791424 ^{a,b,f}
Abell 1795	134852.5+263532 ^e	13485251+2635348	...	8788480 ^{a,b} , 8789504 ^a
Abell 1835	140102.0+025243 ^e	14010204+0252423	4404480, 4404224	19042560 ^{a,b} , 19042816 ^{a,f} 19043072 ^{a,f} , 23307520 ^a 4764160 ^a , 4764416 ^a , 4744448 ^{a,b,f}
Abell 1914	142602.5+374951 ^e	14260257+3749510	12653312, 4752896	4771584 ^a
Abell 1942	143821.9+034014 ^c	14382188+0340138
Abell 1991	145431.5+183831 ^d	14543146+1838325	18653696	...
Abell 1995	145257.4+580252 ^e	14525739+5802543
Abell 2029	151056.1+054439 ^e	15105610+0544416	...	17479680 ^a , 17480192 ^a 17480448 ^{a,b,f} , 17480704 ^{a,b,f} , 8790016 ^{a,b,f}
Abell 2034	151011.5+332908 ^d	15101172+3329112
Abell 2052	151644.5+070119 ^e	15164448+0701180	18654464	18641664 ^{a,b}
Abell 2063 ^g	152305.2+083634 ^d , 152305.4+083633 ^c	15230530+0836330	...	28314368 ^{a,b}
Abell 2065	152223.9+274252 ^d	15222403+2742521
Abell 2069	152408.3+295257 ^e	15240841+2952553
Abell 2104	...	15400795-0318162	25411328	...
Abell 2107 ^g	153939.1+214657 ^e	15393904+2146579	...	28314880 ^{a,b}
Abell 2111	153940.6+342527 ^e	15394049+3425276
Abell 2124	154459.0+360634 ^e	15445899+3606344
Abell 2125	...	15411437+6615567	...	11012096 ^a , 11012352 ^a 11012608 ^a , 11012864 ^a , 11013888 ^a
Abell 2142 ^g	155819.9+271401 ^e	15582002+2714000	...	28314112 ^{a,b}

Table 2—Continued

Cluster Name	<i>GALEX</i> IAU Name	2MASS ID	IRAC AOR	MIPS AOR
Abell 2147	160217.1+155831 ^e	16021700+1558282
Abell 2151	160435.7+174318 ^e	16043575+1743172	...	3860480 ^{a,b,f}
Abell 2163	...	16 ^h 15 ^m 33 ^s .60, −06° 09′ 16″
Abell 2187	162413.7+411433 ^e	16241402+4114377
Abell 2199	162838.3+393304 ^d , 162838.2+393304 ^c	16283827+3933049	3860992 ^h , 3861248 ^h	14957056 ^{a,f}
Abell 2204	...	16324698+0534410	18655232	18642432 ^{a,b}
Abell 2218	163549.3+661244	16 ^h 35 ^m 49 ^s .39, 66° 12′ 45 1″	14697728, 14698240 14698496, 4751616	19044096 ^f , 19044352 ^b , 19044608 ^f 4763648 ^a , 4763904 ^a
Abell 2219	164019.8+464242 ^e	16401981+4642409	4756224	23308544 ^a , 4773376 ^a , 4773632 ^a
Abell 2244	...	17024247+3403363
Abell 2255	171229.1+640338 ^e	17122875+6403385	...	21778944 ^{a,b}
Abell 2256	170427.0+783826 ^e	17042724+7838260
Abell 2259	...	17200968+2740077
Abell 2261	...	17222717+3207571	12655104, 4752128	4744960 ^{b,f} , 4765184 ^a , 4765440 ^a
Abell 2294	...	17241223+8553116
Abell 2319	192109.9+435647 ^c	19211004+4356443
Abell 2384	...	21522195-1932484
Abell 2390	215336.8+174144 ^e	21533687+1741439	12658688, 23473664 ^j , 4754432 23475712 ^k , 23475968 ^k	19044864 ^b , 19045120 ^f 4743680 ^b , 4762624 ^a , 4762880 ^a
Abell 2409	...	22005255+2058087
Abell 2420	...	22101878-1210141
Abell 2462	223911.4-172029 ^e	22391136-1720284
Abell 2537	...	23082221-0211315	...	23435008 ^a
Abell 2554	231219.9-213007 ^d	23121995-2130098
Abell 2556	231301.3-213804 ^e	23130142-2138039
Abell 2589	232357.2+164637 ^d , 232357.4+1646382	23235741+1646379
Abell 2597	232519.7-120726 ^e	23251973-1207275	13372160	13371904 ^{a,b,f} , 17791744 ^{a,b} , 17792000 ^{a,b}
Abell 2626	233630.6+210848 ^e	23363057+2108498	18657280	18644480 ^{a,b}
Abell 2631	233739.7+001616 ^d	23373975+0016165
Abell 2657	234457.4+091134 ^d	23445742+0911349
Abell 2667	235139.4-260501 ^e	23513947-2605032	23476224, 12656896, 23474688, 4756992	4775424 ^a , 4775680 ^a

Table 2—Continued

Cluster Name	<i>GALEX</i> IAU Name	2MASS ID	IRAC AOR	MIPS AOR
Abell 2717	000313.0-355613 ^e	00031298-3556132
Abell 2744a	...	00 ^h 14 ^m 20 ^s .677, −30°24′00 15″	12653568, 4753920	11359232 ^{b,f} , 4765696 ^a , 4765952 ^a
Abell 2744b	...	00 ^h 14 ^m 22 ^s .0, −30°24′20″	12653568, 4753920	11359232 ^{b,f} , 4765696 ^a , 4765952 ^a
Abell 2813	...	00432504-2037054
Abell 3084	030403.7-365629 ^e	03040396-3656274	...	23412224 ^a
Abell 3088	...	03070207-2839574	...	23412480 ^a
Abell 3112	031757.6-441417 ^e	03175766-4414175	18667264	18667008 ^{a,b}
Abell 3120	032156.0-511935 ^e	03215645-5119357
Abell 3158	034252.9-533752 ^e	03425295-5337526	...	8788736 ^{a,b,f}
Abell 3266	043113.3-612713 ^e	04311330-6127114	...	8788992 ^{a,b} , 8789760 ^a
Abell 3364	...	05473773-3152237	...	23416832 ^a
Abell 3376	060209.3-395702 ^e	06020973-3956597
Abell 3391	...	06262045-5341358	...	14426880 ^{a,b,f}
Abell 3395	...	06264958-5432340
Abell 3528S	125441.1-291340 ^e	12544100-2913397
Abell 3558	132756.8-312946 ^e	13275688-3129437
Abell 3562	133334.8-314019 ^d	13333473-3140201
Abell 3571	...	13472838-3251540
Abell 3581	140729.7-270104 ^e	14072978-2701043
Abell 3667	...	20122726-5649363
Abell 3822	215404.1-575203 ^e	21540421-5752033
Abell 3827	220153.0-595645 ^e	22015330-5956437
Abell 3921	224957.9-642547 ^e	22495818-6425468
Abell 4038	...	23474504-2808265
Abell 4059	235700.7-344531 ^d	23570068-3445331	18666240	18665984 ^{a,b}
Abell S0405	035133.9-821312 ^e	03513399-8213103
Abell S0592	...	06384867-5358246	...	23417600 ^a
AC 114	...	22584841-3448087	4756480, 25412864, 12653824	4773888 ^a , 4774144 ^a
AWM7	025427.5+413448 ^d	02542739+4134467
CENTAURUS	124849.4-411838 ^e	12484927-4118399	11042816	11043328 ^{a,b,f}
CID 0072	173301.8+434535 ^e	17330202+4345345	18656000	18643200 ^{a,b}

Table 2—Continued

Cluster Name	<i>GALEX</i> IAU Name	2MASS ID	IRAC AOR	MIPS AOR
CL J1226.9+3332	122658.7+333249 ^d	12 ^h 26 ^m 58 ^s .24, 33°32′48 6″	15062784 ^k , 15063040 ^j 22555904 ^k , 22556160 ^k , 3815680	4761088 ^a , 4761344 4748032 ^{b,f}
CYGNUS A	...	19592833+4044022	14265344 ^k	21694208 ^a , 4710656 ^{a,b,f}
ESO 3060170	054006.4-405009 ^d	05400667-4050114
ESO 5520200	045452.5-180657 ^e	04545226-1806561
EXO 0422-086	042551.8-083330 ^e	04255133-0833389
HCG 0062	125305.7-091213 ^c	12530567-0912141	11251712	11248640 ^{a,b}
HCG 42	100014.1-193809 ^e	10001412-1938113	11250688 ^j , 11253248 ^k	11247616 ^{a,b}
HERCULES A	165108.1+045933 ^e	16510802+0459349	26922496 ^k	21692928 ^a
HYDRA A	091805.5-120544 ^d , 091805.6-120543 ^c	09180565-1205439	26923008 ^k	21691136 ^a , 4707584 ^{a,b,f}
M49	122946.6+080000 ^d , 122946.7+080006 ^c	12294679+0800014	4469760 ^h	4470272 ^{a,b,f}
M87	123049.4+122328 ^e	12304942+1223279	12673792 ^h	11375872 ^a , 21683200 ^a , 4693248 ^{a,b,f}
MACS J0011.7-1523
MACS J0035.4-2015	...	00352611-2015440
MACS J0159.8-0849
MACS J0242.5-2132
MACS J0257.1-2325
MACS J0257.6-2209	...	02574108-2209179
MACS J0308.9+2645	...	03085592+2645373
MACS J0329.6-0211	...	03 ^h 29 ^m 41 ^s .68, −02°11′48 9″
MACS J0417.5-1154
MACS J0429.6-0253	...	04293604-0253073
MACS J0520.7-1328	...	05204205-1328477
MACS J0547.0-3904
MACS J0717.5+3745	23163648	23164160, 23163904, 23164928
MACS J0744.8+3927	...	07 ^h 44 ^m 51 ^s .98, 39°27′35 1″
MACS J1115.2+5320
MACS J1115.8+0129
MACS J1131.8-1955	...	11315413-1955391
MACS J1149.5+2223	...	11 ^h 49 ^m 36 ^s , 22°23′53″
MACS J1206.2-0847

Table 2—Continued

Cluster Name	<i>GALEX</i> IAU Name	2MASS ID	IRAC AOR	MIPS AOR
MACS J1311.0-0310
MACS J1621.3+3810
MACS J1931.8-2634
MACS J2049.9-3217
MACS J2211.7-0349	...	22114596-0349438	...	23433984 ^a
MACS J2214.9-1359	...	22 ^h 14 ^m 56 ^s .51, 14°00′17″
MACS J2228+2036
MACS J2229.7-2755	222945.2-275536 ^e	22294524-2755353
MACS J2245.0+2637	...	22450463+2638039
MKW3S	152151.8+074229 ^e	15215187+0742319
MKW 04	120427.0+015344 ^e	12042705+0153456	18034432 ^h	18042624 ^{a,b,f}
MKW 08	144042.8+032755 ^e	14404287+0327555
MS 0016.9+1609	...	00 ^h 18 ^m 33 ^s .6, 16°26′15″	4756736, 12656128	...
MS 0116.3-0115	011853.6-010006 ^e	01185363-0100074
MS 0440.5+0204	044310.1+021016 ^d	04430994+0210190
MS 0451.6-0305	...	04 ^h 54 ^m 10 ^s .85, −03°00′51″	12652800, 4753664	19039232 ^b , 19039488 ^f 19039744 ^b , 19040000 ^f 4747520 ^{b,f} , 4770304 ^a , 4770560 ^a
MS 0735.6+7421	074144.1+741440 ^e	07414444+7414395	7858688	...
MS 0839.8+2938	084256.0+292728 ^e	08425596+2927272	...	23303936 ^a , 23418880 ^a
MS 0906.5+1110	...	09091273+1058286	...	23419136 ^a
MS 1006.0+1202	...	10084771+1147379
MS 1008.1-1224	...	10103233-1239524	25410304	...
MS 1455.0+2232	145715.1+222033 ^e	14571507+2220341	12657408, 4753152	4767744 ^a , 4768000 ^a
MS 2137.3-2353	214015.1-233939 ^e	21401517-2339398	12658944, 4755968	4772864 ^a , 4773120 ^a
MS J1157.3+5531	115952.3+553205 ^e	11595215+5532053
NGC 0507	012340.1+331522 ^e	01233995+3315222	18030080 ^h	14253824 ^{a,f} , 14254080 ^{a,b}
NGC 4636	124249.8+024117 ^e	12424986+0241160	4475136	4475648 ^{a,b,f}
NGC 5044	131523.7-162305 ^e	13152396-1623079	15573504	14258432 ^{a,f} , 14258688 ^{a,b}
NGC 5813	150111.4+014208 ^e	15011126+0142070	4490496 ^h	4491008 ^{a,b,f}
NGC 5846	150629.4+013621 ^e	15062925+0136202	16310272 ^h , 4491264	4491776 ^{a,b,f}

Table 2—Continued

Cluster Name	<i>GALEX</i> IAU Name	2MASS ID	IRAC AOR	MIPS AOR
OPHIUCHUS	171227.6-232209 ^d	17122774-2322108
PKS 0745-191	...	07473129-1917403	18667776	18667520 ^{a,b}
RBS 0461	...	03411752+1523477
RBS 0533	041937.8+022435 ^e	04193792+0224355
RBS 0797	094712.4+762313 ^e	09 ^h 47 ^m 12 ^s .6, 76°23′14″
RCS J2327-0204	232729.2-020323 ^e	23 ^h 27 ^m 29 ^s .0, −02°03′23″
RXCJ0331.1-2100	...	03310587-2100326	...	23412736 ^a
RXC J1023.8-2715	102350.0-271523 ^e	10235019-2715232
RX J0220.9-3829	...	02205660-3828475
RX J0232.2-4420
RX J0439+0520	043902.2+052047 ^d	04390223+0520443	18649344	18649088 ^{a,b}
RX J0439.0+0715	...	04390053+0716038
RX J0528.9-3927	33327104	23415552 ^a
RX J0647.7+7015	...	06 ^h 47 ^m 51 ^s .45, 70°15′04 4″
RX J0819.6+6336	081925.9+633726 ^d	08192591+6337256
RX J1000.4+4409	100031.2+440844 ^d	10 ^h 00 ^m 31 ^s .0, 44°08′43″
RX J1022.1+3830	102210.3+383104 ^d	10221031+3831045
RX J1130.0+3637	113003.3+363812 ^d	11300319+3638135
RX J1320.2+3308	132014.6+330835 ^c	13201472+3308359
RX J1347.5-1145	134730.7-114509 ^e	13 ^h 47 ^m 31 ^s .0, −11°45′09″	12654336	...
RX J1423.8+2404
RX J1504.1-0248	150407.6-024815 ^e	15040752-0248161	...	23426048 ^a
RX J1532.9+3021	...	15 ^h 32 ^m 53 ^s .8, 30°21′00″	18658560	18658304 ^{a,b}
RX J1539.5-8335	...	15393387-8335215
RX J1720.1+2638	172010.0+263730 ^e	17201001+2637317	...	18659072 ^{a,b}
RX J1720.2+3536
RX J1852.1+5711	185208.5+571144 ^d	18520859+5711430
RX J2129.6+0005	212939.9+000522 ^e	21293995+0005207	18659584	18659328 ^{a,b}
SC 1327-312	132947.5-313625 ^e	13294775-3136250
SERSIC 159-03	231358.8-424336 ^e	23135863-4243393	18665728	18665472 ^{a,b}
SS2B153	105026.1-125041 ^e	10502610-1250422

Table 2—Continued

Cluster Name	<i>GALEX</i> IAU Name	2MASS ID	IRAC AOR	MIPS AOR
UGC 03957	074058.2+552538 ^e	07405822+5525379
UGC 12491	...	23183823+4257289
ZWCL 1215	121741.2+033922 ^d	12174112+0339208
ZWCL 1358+6245	135950.5+623104 ^e	13 ^h 59 ^m 50 ^s .0, 62°31′03″	12657920, 23473920 ^j , 23474432 ^j 23478272 ^k , 23478528 ^k , 4754944	4770816 ^a , 4771072 ^a
ZWCL 1742	...	17441450+3259292	18656256	18643456 ^{a,b}
ZWCL 1953	...	08500730+3604203
ZWCL 3146	102339.6+041110 ^e	10233960+0411116	12654592, 4751872	4768256 ^a , 4768512 ^a , 4746496 ^{a,b,f}
ZWICKY 2701	...	09524915+5153053	18649856	18649600 ^{a,b}
ZwCl 0857.9+2107	090036.9+205342 ^e	09003684+2053402	18660096	18659840 ^{a,b}

^aMIPS observation includes a 24 μ m observation.

^bMIPS observation includes a 70 μ m observation.

^c*GALEX* observation only includes FUV measurement.

^d*GALEX* observation only includes NUV measurement.

^e*GALEX* observation includes both NUV and FUV measurement.

^fMIPS observation includes a 160 μ m observation.

^g*Spitzer* observations were made by Donahue as part of the DDT program 488.

^hDue to an anomalous point source in the pbcd reduction, the images needed to be reduced from the bcd frames.

ⁱ*GALEX* observation was taken as a Guest Investigator for Hicks et al. (2010).

^jIRAC observation only has bands 1 and 3 on target.

^kIRAC observation only has bands 2 and 4 on target.

Table 3. Physical Properties.

Cluster Name	Redshift	Central Entropy ^a (keV cm ²)	K_{100} ^a (keV cm ²)	alpha ^a (kpc/'')	Scale (kpc/'')	IR Radius ('')	UV Radius ('')	Centroid Offset ^a (kpc)
1E0657 56a	0.2960	307.45	18.55	1.88	4.41	3.24	...	503.92
1E0657 56b	0.2960	307.45	18.55	1.88	4.41	3.24	...	216.72
2A 0335+096	0.0347	7.14	138.64	1.52	0.69	20.7	12.8	1.00
2PIGG J0011.5-2850	0.0753	101.98	214.68	0.84	1.43	10.01	17.3	2.10
2PIGG J2227.0-3041	0.0729	17.13	113.95	1.37	1.39	10.31	17.3	0.59
3C 28.0	0.1952	23.85	107.82	1.79	3.24	4.42	12.8	3.55
3C 295	0.4641	14.54	81.95	1.47	5.86	2.44	9	16.98
3C 388	0.0917	17.03	214.3	0.76	1.71	8.38	17.3	1.44
4C 55.16	0.2420	23.27	161.6	1.29	3.82	3.75	9	31.64
Abell 13	0.0940	182.64	181.95	1.37	1.75	8.19	12.8	0.89
Abell 68	0.2546	217.34	142.31	0.89	3.96	3.61	9	3.77
Abell 85	0.0558	12.5	158.83	1.12	1.08	13.2	17.3	1.86
Abell 119	0.0442	233.85	191.29	0.75	0.87	16.44	17.3	2.20
Abell 133	0.0558	17.26	170.12	1.59	1.08	13.2	17.3	3.29
Abell 141	0.2300	205.03	42.56	1.78	3.67	3.89	9	4.38
Abell 160	0.0447	155.78	116.26	0.98	0.88	16.26	17.3	1.65
Abell 193	0.0485	185.46	35.96	2.23	0.95	15.05	17.3	0.57
Abell 209	0.2060	105.5	149.31	0.8	3.38	4.23	12.8	7.85
Abell 222	0.2130	126.02	82.25	1	3.47	4.13	9	7.83
Abell 223	0.2070	183.87	160.65	1.24	3.39	4.22	9	1.13
Abell 262	0.0164	10.57	205.09	0.98	0.33	42.84	17.3	0.25
Abell 267	0.2300	168.56	51.81	1.82	3.67	3.89	17.3	1.52
Abell 368	0.2200	50.87	144.12	1.21	3.55	4.03	...	60.21
Abell 370	0.3747	321.92	78.72	1.24	5.16	2.77	9	99.67
Abell 383	0.1871	13.02	110.9	1.4	3.13	4.57	17.3	2.63
Abell 399	0.0716	153.2	204.34	0.74	1.36	10.48	9	1.52
Abell 400	0.0240	162.81	35.26	1.76	0.48	29.55	17.3	4.61
Abell 401	0.0745	166.86	81.79	1.4	1.42	10.11	17.3	1.12
Abell 426	0.0179	19.38	119.89	1.74	0.36	39.32	17.3	0.33
Abell 478	0.0883	7.81	122	0.97	1.65	8.66	...	0.44
Abell 496	0.0328	8.91	216.33	1.27	0.65	21.85	...	1.48
Abell 520	0.2020	325.54	10.22	2.09	3.33	4.3	...	643.52
Abell 521	0.2533	259.87	245.43	1.91	3.95	3.62	...	4.23
Abell 539	0.0288	22.59	493.32	1.05	0.58	24.76	9	15.36
Abell 562	0.1100	202.06	34.61	1.09	2.01	7.13	...	0.43
Abell 576	0.0385	95.29	221.21	1.41	0.76	18.74	17.3	0.59
Abell 586	0.1710	94.75	92.06	1.25	2.91	4.91	...	2.51
Abell 611	0.2880	124.93	164.35	1.25	4.33	3.3	9	1.44
Abell 644 ^b	0.0698	132.36	85.91	1.55	1.33	10.73	7	0.97
Abell 665	0.1810	134.57	106.34	1.06	3.05	4.69	17.3	3.57

Table 3—Continued

Cluster Name	Redshift	Central Entropy ^a (keV cm ²)	K_{100} ^a (keV cm ²)	alpha ^a	Scale (kpc/'')	IR Radius ('')	UV Radius ('')	Centroid Offset ^a (kpc)
Abell 697	0.2820	166.67	108.16	1.1	4.27	3.35	17.3	7.72
Abell 744	0.0729	63.42	229.33	0.79	1.39	10.31	17.3	0.79
Abell 754	0.0543	270.39	69.67	1.48	1.06	13.54	17.3	0.65
Abell 773	0.2170	244.32	41.1	1.6	3.52	4.07	9	7.22
Abell 907	0.1527	23.38	187.01	1.05	2.65	5.39	12.8	3.21
Abell 963	0.2056	55.77	169.12	0.9	3.37	4.24	17.3	6.41
Abell 1060	0.0125	72	178.34	1.25	0.26	55.94	17.3	0.35
Abell 1063S	0.3540	169.59	42.21	1.72	4.98	2.87	9	4.31
Abell 1068	0.1375	9.11	108.8	1.31	2.43	5.88	17.3	1.74
Abell 1201	0.1688	64.81	198.94	1.03	2.88	4.96	17.3	1.62
Abell 1204	0.1706	15.31	81.83	1.4	2.91	4.92	9	4.68
Abell 1240	0.1590	462.4	8.27	2.37	2.74	5.21
Abell 1361	0.1171	18.64	117.86	1.06	2.12	6.75	17.3	8.10
Abell 1413	0.1426	64.03	123.19	1.19	2.51	5.71	17.3	2.90
Abell 1423	0.2130	68.32	124.17	1.2	3.47	4.13	9	2.14
Abell 1446	0.1035	152.38	119.5	0.67	1.9	7.52	12.8	3.11
Abell 1569	0.0735	110.1	149.14	0.51	1.4	10.23	9	0.43
Abell 1576	0.2790	186.24	98.35	1.38	4.23	3.38	...	13.26
Abell 1644	0.0471	19.03	585.67	1.76	0.92	15.48	17.3	0.54
Abell 1650	0.0843	37.96	159.89	0.84	1.58	9.03	17.3	1.09
Abell 1651	0.0840	89.46	115.53	0.97	1.58	9.06	...	1.95
Abell 1664	0.1276	14.4	141.84	1.7	2.28	6.27	12.8	1.12
Abell 1689	0.1843	78.44	111.77	1.35	3.09	4.62	9	21.14
Abell 1736	0.0338	150.35	127.25	0.99	0.67	21.23	12.8	0.20
Abell 1758	0.2792	230.84	144.04	1.21	4.24	3.38	...	272.85
Abell 1763	0.1866	214.69	70.8	1.37	3.12	4.58	17.3	0.91
Abell 1795	0.0625	18.99	130.38	1.18	1.2	11.88	17.3	1.21
Abell 1835	0.2532	11.44	111.71	1.26	3.95	3.62	12.8	7.93
Abell 1914	0.1712	107.16	131.15	1.05	2.91	4.91	9	58.40
Abell 1942	0.2240	107.73	194.08	0.66	3.6	3.97	9	3.00
Abell 1991	0.0587	1.53	152.21	1.09	1.14	12.59	17.3	1.90
Abell 1995	0.3186	374.35	26.81	2.08	4.64	3.08	9	2.89
Abell 2029	0.0765	10.5	163.58	0.95	1.45	9.86	17.3	1.75
Abell 2034	0.1130	232.64	85.07	1.14	2.05	6.96	17.3	3.94
Abell 2052	0.0353	9.45	164.72	1.25	0.7	20.36	17.3	0.80
Abell 2063	0.0351	53.51	129.01	1.07	0.7	20.47	17.3	1.11
Abell 2065	0.0730	43.95	195.29	1.02	1.39	10.29	9	112.52
Abell 2069	0.1160	453.25	54.57	1.47	2.1	6.81	9	2.26
Abell 2104	0.1554	160.61	210.1	1.2	2.69	5.31	9	0.96
Abell 2107	0.0411	21.24	396.13	0.91	0.81	17.61	17.3	0.91

Table 3—Continued

Cluster Name	Redshift	Central Entropy ^a (keV cm ²)	K_{100} ^a (keV cm ²)	alpha ^a	Scale (kpc/'')	IR Radius ('')	UV Radius ('')	Centroid Offset ^a (kpc)
Abell 2111	0.2300	107.36	193.98	0.65	3.67	3.89	17.3	4.20
Abell 2124	0.0658	98.31	260.81	0.9	1.26	11.33	17.3	1.19
Abell 2125	0.2465	225.17	32.9	1.35	3.87	3.7	9	18.90
Abell 2142	0.0898	68.06	120.57	1.22	1.68	8.53	17.3	0.93
Abell 2147	0.0356	151.86	136.19	0.55	0.71	20.2	17.3	0.28
Abell 2151	0.0366	0.37	135.18	0.56	0.73	19.67	17.3	0.12
Abell 2163	0.1695	437.98	72.21	1.87	2.89	4.95	...	524.17
Abell 2187	0.1833	78.63	170.71	0.96	3.08	4.64	12.8	0.53
Abell 2199	0.0300	13.27	331.46	1.35	0.6	23.81	17.3	0.42
Abell 2204	0.1524	9.74	166.19	1.41	2.65	5.4	...	21.70
Abell 2218	0.1713	288.56	10.72	2.35	2.92	4.9	9	26.65
Abell 2219	0.2256	411.57	17.01	1.97	3.62	3.95	17.3	0.54
Abell 2244	0.0967	57.58	109.07	1	1.79	7.99	...	3.45
Abell 2255	0.0805	529.1	5.78	2.63	1.52	9.42	12.8	149.58
Abell 2256	0.0579	349.58	7.05	2.54	1.12	12.75	12.8	877.60
Abell 2259	0.1640	113.98	60.96	1.36	2.81	5.08	9	3.42
Abell 2261	0.2240	61.08	105.96	1.27	3.6	3.97	...	1.82
Abell 2294	0.1780	156.31	235.74	1.03	3.01	4.75	...	9.62
Abell 2319	0.0562	270.23	39.42	1.76	1.09	13.11	12.8	6.12
Abell 2384	0.0945	38.48	139.21	1.49	1.75	8.15	...	3.69
Abell 2390	0.2301	14.73	202.92	1.07	3.68	3.89	17.3	3.02
Abell 2409	0.1479	73.81	120.76	0.97	2.58	5.53	9	5.60
Abell 2420	0.0846	332.56	64.33	1.12	1.59	9	...	1.22
Abell 2462	0.0737	129.68	83.2	0.77	1.4	10.21	12.8	0.17
Abell 2537	0.2950	110.41	124.72	1.26	4.4	3.25	...	3.60
Abell 2554	0.1103	105.09	318.36	0.66	2.01	7.11	12.8	1.59
Abell 2556	0.0862	12.38	115.76	1.13	1.62	8.85	17.3	0.93
Abell 2589	0.0415	51.99	109.56	0.61	0.82	17.45	17.3	0.66
Abell 2597	0.0854	10.6	98.88	1.26	1.6	8.93	17.3	2.16
Abell 2626	0.0573	23.19	144.08	1.05	1.11	12.88	17.3	3.36
Abell 2631	0.2779	308.81	29.18	1.44	4.22	3.39	17.3	4236.20
Abell 2657	0.0402	65.39	153.55	0.91	0.8	17.98	9	0.79
Abell 2667	0.2300	19.31	93.44	1.31	3.67	3.89	12.8	15.44
Abell 2717	0.0475	27.05	151.19	0.75	0.93	15.35	17.3	0.18
Abell 2744a	0.3080	438.44	46.39	1.41	4.54	3.15	...	151.49
Abell 2744b	0.3080	438.44	46.39	1.41	4.54	3.15	...	268.24
Abell 2813	0.2924	267.63	90.43	1.76	4.38	3.27	9	34.07
Abell 3084	0.0977	96.74	193.67	1.08	1.81	7.92	17.3	1.16
Abell 3088	0.2534	82.78	216.83	1.71	3.95	3.62	...	7.37
Abell 3112	0.0720	11.4	169.12	1.17	1.37	10.43	17.3	0.64

Table 3—Continued

Cluster Name	Redshift	Central Entropy ^a (keV cm ²)	K_{100} ^a (keV cm ²)	alpha ^a	Scale (kpc/'')	IR Radius ('')	UV Radius ('')	Centroid Offset ^a (kpc)
Abell 3120	0.0690	17.29	206.17	0.99	1.32	10.84	17.3	0.48
Abell 3158	0.0580	166.01	80.92	0.9	1.12	12.73	17.3	1.51
Abell 3266	0.0590	72.45	376.73	0.64	1.14	12.53	17.3	7.23
Abell 3364	0.1483	268.55	34.53	1.97	2.59	5.52	...	1.26
Abell 3376	0.0456	282.95	58.97	1.71	0.9	15.96	17.3	0.99
Abell 3391	0.0560	367.52	23.56	1.64	1.09	13.15	...	1.31
Abell 3395	0.0510	247.2	105.85	1.65	1	14.36	...	2.20
Abell 3528S	0.0530	31.56	270.04	1.17	1.03	13.85	17.3	2.05
Abell 3558	0.0480	126.15	132.52	2.11	0.94	15.2	17.3	0.38
Abell 3562	0.0490	77.42	159.76	0.81	0.96	14.91	12.8	0.93
Abell 3571	0.0391	79.31	191.27	0.82	0.77	18.47	...	0.53
Abell 3581	0.0218	9.51	138.07	1.22	0.44	32.44	17.3	0.70
Abell 3667	0.0556	160.43	110.56	0.78	1.08	13.24	...	1.32
Abell 3822	0.0759	108.66	200.32	0.66	1.44	9.93	17.3	0.87
Abell 3827	0.0984	164.58	94.8	1.34	1.82	7.87	17.3	2.96
Abell 3921	0.0927	101.19	151.49	0.86	1.72	8.29	17.3	1.33
Abell 4038	0.0300	37.93	117.86	1.11	0.6	23.81	...	0.58
Abell 4059	0.0475	7.06	203.16	0.88	0.93	15.35	17.3	1.40
Abell S0405	0.0613	16.94	274.22	0.45	1.18	12.09	17.3	5.47
Abell S0592	0.2216	58.7	195.48	0.99	3.57	4	...	6.93
AC 114	0.3120	199.79	69.99	1.5	4.58	3.13	9	2.48
AWM7	0.0172	8.37	227.59	0.8	0.35	40.89	17.3	0.26
CENTAURUS	0.0109	2.25	474.86	1.33	0.22	64.03	17.3	0.08
CID 0072	0.0344	9.45	133.25	0.99	0.69	20.87	17.3	0.60
CL J1226.9+3332	0.8900	166.03	99	1.41	7.77	1.84	7	15.14
CYGNUS A	0.0561	23.64	210.12	1.57	1.09	13.13	...	0.85
ESO 3060170	0.0358	7.98	1400.88	1.8	0.71	20.09	17.3	1.03
ESO 5520200	0.0314	5.89	121.77	0.67	0.63	22.78	17.3	0.61
EXO 0422-086	0.0397	13.77	193.82	1.25	0.79	18.2	9	2.07
HCG 0062	0.0146	3.44	219.02	1.28	0.3	48.02	17.3	7.71
HCG 42	0.0133	1.85	126.46	0.87	0.27	52.63	17.3	0.49
HERCULES A	0.1541	9.17	143.89	1.07	2.67	5.35	17.3	8.65
HYDRA A	0.0549	13.31	114.92	1.03	1.07	13.4	17.3	0.40
M49	0.0033	0.91	495.33	1.14	0.07	209.55	17.3	0.07
M87	0.0044	3.53	146.6	0.8	0.09	157.37	17.3	0.09
MACS J0011.7-1523	0.3600	18.83	109.14	1.04	5.03	2.84
MACS J0035.4-2015	0.3644	93.42	76.4	1.26	5.07	2.82	...	248.81
MACS J0159.8-0849	0.4050	18.79	123.87	1.31	5.41	2.64
MACS J0242.5-2132	0.3140	10.92	74.59	1.29	4.6	3.11
MACS J0257.1-2325	0.5053	234.47	195.81	1.39	6.14	2.33

Table 3—Continued

Cluster Name	Redshift	Central Entropy ^a (keV cm ²)	K_{100} ^a (keV cm ²)	alpha ^a (kpc/'')	Scale (kpc/'')	IR Radius (")	UV Radius (")	Centroid Offset ^a (kpc)
MACS J0257.6-2209	0.3224	155.91	82.11	1.55	4.68	3.06	9	1.52
MACS J0308.9+2645	0.3240	212.76	70.07	1.43	4.69	3.05	9	4.91
MACS J0329.6-0211	0.4500	11.13	96.68	1.26	5.76	2.48	...	7.08
MACS J0417.5-1154	0.4400	27.08	99.69	1.42	5.69	2.52
MACS J0429.6-0253	0.3990	17.17	88.87	1.23	5.36	2.67	...	1.91
MACS J0520.7-1328	0.3398	88.59	84.92	1.2	4.85	2.95	...	8.14
MACS J0547.0-3904	0.2100	23.14	121.59	1.2	3.43	4.17
MACS J0717.5+3745	0.5480	220.15	160.08	0.76	6.4	2.23
MACS J0744.8+3927	0.6860	42.38	112.02	1.11	7.09	2.02	...	101.36
MACS J1115.2+5320	0.4390	292.28	27.56	1.73	5.68	2.52
MACS J1115.8+0129	0.3521	14.76	107.65	1.31	4.96	2.88
MACS J1131.8-1955	0.3070	97.26	156.32	1.15	4.53	3.16	...	2.56
MACS J1149.5+2223	0.5440	280.69	33.13	1.47	6.38	2.24	...	18.05
MACS J1206.2-0847	0.4400	69.04	94.69	1.28	5.69	2.52
MACS J1311.0-0310	0.4940	47.36	63.47	1.62	6.06	2.36
MACS J1621.3+3810	0.4610	20.08	129.83	1.18	5.84	2.45
MACS J1931.8-2634	0.3520	14.56	87.52	1.27	4.96	2.88
MACS J2049.9-3217	0.3254	195.85	92.71	1.06	4.71	3.04
MACS J2211.7-0349	0.2700	165.49	78.26	1.59	4.14	3.46	...	2.55
MACS J2214.9-1359	0.5026	297.7	171.96	1.46	6.12	2.34	...	98.06
MACS J2228+2036	0.4120	118.79	107.22	1	5.47	2.61
MACS J2229.7-2755	0.3240	12.39	74.97	1.36	4.69	3.05	17.3	6.04
MACS J2245.0+2637	0.3040	42.03	105.93	1.33	4.5	3.18	9	2.65
MKW3S	0.0450	23.94	131.08	0.96	0.88	16.16	17.3	0.78
MKW 04	0.0198	6.86	392.7	1.26	0.4	35.63	17.3	0.21
MKW 08	0.0270	130.68	228.51	0.87	0.54	26.36	17.3	32.83
MS 0016.9+1609	0.5410	162.07	64.17	1.29	6.36	2.25
MS 0116.3-0115	0.0452	12.77	220.8	0.63	0.89	16.09	17.3	0.64
MS 0440.5+0204	0.1900	25.46	164.03	1.11	3.17	4.51	9	1.11
MS 0451.6-0305	0.5386	568.13	15.61	2.81	6.34	2.25	...	14.34
MS 0735.6+7421	0.2160	15.96	106.79	1.14	3.5	4.08	9	2.85
MS 0839.8+2938	0.1940	19.19	105.79	1.33	3.22	4.44	9	0.83
MS 0906.5+1110	0.1630	104.23	97.32	1.15	2.8	5.11	...	1.49
MS 1006.0+1202	0.2210	160.28	82.81	1.32	3.56	4.01	...	8.20
MS 1008.1-1224	0.3010	97.62	262.05	0.76	4.46	3.2	...	2.19
MS 1455.0+2232	0.2590	16.88	81.47	1.39	4.01	3.56	9	5.70
MS 2137.3-2353	0.3130	14.68	89.85	1.39	4.59	3.12	17.3	4.20
MS J1157.3+5531	0.0810	5.93	277.01	1.45	1.53	9.36	9	3.38
NGC 0507	0.0164	0	99.89	0.65	0.33	42.84	17.3	0.27
NGC 4636	0.0031	1.42	11962.07	1.96	0.06	223.01	17.3	0.01

Table 3—Continued

Cluster Name	Redshift	Central Entropy ^a (keV cm ²)	K_{100} ^a (keV cm ²)	alpha ^a	Scale (kpc/'')	IR Radius ('')	UV Radius ('')	Centroid Offset ^a (kpc)
NGC 5044	0.0090	2.28	82.15	0.96	0.18	77.37	17.3	0.06
NGC 5813	0.0066	1.38	102.51	0.91	0.14	105.2	17.3	0.03
NGC 5846	0.0057	1.83	685.78	1.44	0.12	121.67	17.3	0.07
OPHIUCHUS	0.0280	8.95	247.48	0.73	0.56	25.45	12.8	2.28
PKS 0745-191	0.1028	12.41	110.7	1.39	1.89	7.57	...	8.00
RBS 0461	0.0290	95.67	68.8	1.39	0.58	24.6	9	0.34
RBS 0533	0.0123	2.22	164.34	1	0.25	56.84	17.3	0.33
RBS 0797	0.3540	19.49	97.67	1.67	4.98	2.87	9	3.38
RCS J2327-0204	0.2000	68.55	217.2	1.28	3.3	4.33	17.3	261.00
RXCJ0331.1-2100	0.1880	11.4	134.1	1.3	3.14	4.55	...	1.09
RXC J1023.8-2715	0.0963	20.86	255.29	1.45	1.78	8.02	12.8	1.03
RX J0220.9-3829	0.2287	43	159.95	1.23	3.66	3.91	...	1.44
RX J0232.2-4420	0.2836	44.62	166.53	1.16	4.28	3.34
RX J0439+0520	0.2080	14.92	95.47	1.19	3.4	4.2	9	4.10
RX J0439.0+0715	0.2300	66.75	129.57	1.06	3.67	3.89	...	4.00
RX J0528.9-3927	0.2632	72.85	99.8	1.47	4.06	3.52
RX J0647.7+7015	0.5840	225.06	48.82	1.7	6.6	2.17	...	108.26
RX J0819.6+6336	0.1190	20.69	170.57	0.68	2.15	6.66	9	3.69
RX J1000.4+4409	0.1540	27.71	151.1	1.09	2.67	5.35	9	30.73
RX J1022.1+3830	0.0491	51.6	194.76	1.04	0.96	14.88	17.3	18.72
RX J1130.0+3637	0.0600	29.93	149.6	1.14	1.16	12.34	17.3	0.92
RX J1320.2+3308	0.0366	8.8	140.28	1.28	0.73	19.67	17.3	0.85
RX J1347.5-1145	0.4510	12.45	179.86	1.06	5.77	2.48	9	34.95
RX J1423.8+2404	0.5450	10.23	119.91	1.27	6.38	2.24
RX J1504.1-0248	0.2150	13.08	95.58	1.5	3.49	4.1	12.8	2.93
RX J1532.9+3021	0.3450	16.93	76.31	1.51	4.89	2.92
RX J1539.5-8335	0.0728	25.88	109.99	1.41	1.39	10.32	...	4.41
RX J1720.1+2638	0.1640	21.03	109.14	1.39	2.81	5.08	17.3	1.17
RX J1720.2+3536	0.3913	24	94.44	1.42	5.3	2.7
RX J1852.1+5711	0.1094	18.72	170.36	0.83	2	7.16	9	0.99
RX J2129.6+0005	0.2350	21.14	97.91	1.26	3.73	3.83	17.3	0.61
SC 1327-312	0.0531	64.57	160.82	0.81	1.03	13.83	17.3	0.48
SERSIC 159-03	0.0580	10.45	77.78	1.17	1.12	12.73	17.3	0.85
SS2B153	0.0186	1.12	71.35	0.8	0.38	37.88	17.3	0.66
UGC 03957	0.0341	12.88	175.07	0.98	0.68	21.05	17.3	0.27
UGC 12491	0.0174	2.99	148.48	1.12	0.35	40.43	...	0.43
ZWCL 1215	0.0750	163.23	131.29	1	1.42	10.04	9	3.09
ZWCL 1358+6245	0.3280	20.67	97.97	1.43	4.73	3.02	9	18.84
ZWCL 1742	0.0757	23.84	126.53	1.3	1.44	9.96	...	0.76
ZWCL 1953	0.3800	194.53	62.12	1.39	5.21	2.75	...	4.25

Table 3—Continued

Cluster Name	Redshift	Central Entropy ^a (keV cm ²)	K_{100} ^a (keV cm ²)	alpha ^a	Scale (kpc/″)	IR Radius (″)	UV Radius (″)	Centroid Offset ^a (kpc)
ZWCL 3146	0.2900	11.42	105.48	1.29	4.35	3.29	12.8	2.39
ZWICKY 2701	0.2100	39.66	126	1.45	3.43	4.17	9	1.71
ZwCl 0857.9+2107	0.2350	24.25	89.27	1.4	3.73	3.83	17.3	3.81

^aQuantities defined in Cavagnolo et al. (2009) are from radially fit entropy profiles with a functional form $K(r) = K_0 + K_x(r/r_x)^\alpha$, where K_0 is the central entropy in excess above the power law fit, K_{100} is the entropy profile normalization at $100h_{70}^{-1}$ kpc from the X-ray centroid, and alpha is the best-fit power law index.

^bUV data is taken from Hicks et al. (2010)

Note. — Redshift information and central entropies are reproduced from the ACCEPT database. The size scale is calculated as the angular distance size assuming the standard cosmology in the paper. The IR radii are set at $14.3h_{70}^{-1}$ kpc in size and are used for *2MASS* and IRAC aperture measurements except in the case where the aperture is below 5″. In this case the aperture is set to be 5″ to minimize large aperture corrections. The UV radius is set by the aperture photometry in the *GALEX* database which most closely matches the GALEXView total flux measurement. We compare the BCG positions that we derive from the *2MASS* locations in Table 2 and compare that to the X-ray centroid in the ACCEPT database. These distances are presented in a histogram in Figure 1

Table 4. Fluxes Matched to UV Aperture.

Name Cluster Name	Flux NUV (mag)	Error NUV (mag)	Flux FUV (mag)	Error FUV (mag)	Flux J (mag)	Error J (mag)	Flux H (mag)	Error H (mag)	Flux K (mag)	Error K (mag)
1E0657 56a
1E0657 56b
2A 0335+096	18.05	0	18.50	0	13.48	0.0130	13.13	0.0160	13.09	0.0160
2PIGG J0011.5-2850	20.07	0.1093	20.65	0.2108	13.15	0.0080	12.90	0.0100	13.05	0.0131
2PIGG J2227.0-3041	18.40	0.0176	19.85	0.0568	12.98	0.0070	12.75	0.0090	12.90	0.0106
3C 28.0	20.51	0.3453	20.56	0.2914	15.54	0.0660	15.35	0.0720	15.11	0.0697
3C 295	23.17	0	23.80	0.3245	16.38	0.1570	16.18	0.2230	15.76	0.1470
3C 388	19.95	0.0507	20.97	0.1878	13.29	0.0100	13.10	0.0120	13.28	0.0139
4C 55.16	21.49	0	21.09	0	16.28	0.1640	15.93	0.2000	15.86	0.1770
Abell 13	21.82	0	21.37	0	14.73	0.0370	14.41	0.0460	14.48	0.0510
Abell 68	20.60	0	20.31	0	15.86	0.1240	15.91	0.2080	15.31	0.1310
Abell 85 ^a	18.85	0.0165	19.79	0.0323	12.50	0.0050	12.23	0.0060	12.41	0.0083
Abell 119	19.40	0.0289	20.05	0.0482	12.44	0.0041	12.21	0.0050	12.37	0.0070
Abell 133	19.28	0.1079	20.16	0.2425	12.81	0.0070	12.61	0.0110	12.69	0.0105
Abell 141	21.38	0	20.92	0	16.46	0.1770	15.84	0.1500	15.95	0.1950
Abell 160	19.24	0.0591	20.37	0	12.75	0.0070	12.60	0.0080	12.79	0.0131
Abell 193	21.05	0	20.39	0.2598	12.95	0.0070	12.68	0.0080	12.80	0.0110
Abell 209	21.64	0	21.89	0.0703	15.37	0.0690	15.26	0.1000	15.00	0.0840
Abell 222	21.59	0	21.13	0	15.79	0.0910	15.72	0.1410	15.49	0.1330
Abell 223	21.54	0	21.09	0	16.13	0.1260	15.79	0.1550	15.44	0.1290
Abell 262	18.21	0.0275	19.48	0.0714	11.43	0.0020	11.20	0.0030	11.53	0.0027
Abell 267	21.21	0.2633	21.60	0	14.90	0.0380	14.52	0.0510	14.47	0.0404
Abell 368
Abell 370	21.71	0	21.29	0	16.27	0.1480	16.12	0.1720	15.64	0.1550
Abell 383	20.25	0.2779	18.86	0.1555	14.61	0.0310	14.42	0.0400	14.16	0.0386
Abell 399	20.38	0	20.27	0	14.18	0.0240	13.92	0.0310	13.84	0.0310
Abell 400	18.60	0.1675	20.00	0	11.39	0.0030	11.25	0.0030	11.64	0.0034
Abell 401	19.53	0.3106	20.33	0	12.79	0.0090	12.60	0.0100	12.85	0.0113
Abell 426	14.23	0.0013	15.33	0.0029	10.78	0.0300	10.68	0.0300	11.03	0.0300
Abell 478
Abell 496
Abell 520
Abell 521
Abell 539	18.82	0.2203	20.07	0	12.85	0.0050	12.74	0.0060	13.04	0.0064
Abell 562
Abell 576	21.25	0	20.92	0	13.56	0.0130	13.28	0.0160	13.38	0.0180
Abell 586
Abell 611	22.57	0	22.65	0.3308	16.11	0.1510	15.46	0.1270	15.47	0.1200
Abell 644 ^a ^b	20.94	0.08	20.39	0	13.92	0.0260	13.77	0.0300	14.02	0.0430
Abell 665	22.71	0	21.64	0.3204	15.44	0.0730	15.10	0.0930	15.26	0.1020
Abell 697	22.02	0.1797	22.98	0.2221	14.71	0.0470	14.73	0.0590	14.57	0.0476
Abell 744	20.17	0.2177	21.01	0	13.44	0.0110	13.18	0.0140	13.36	0.0130
Abell 754	21.02	0	20.68	0	13.85	0.0170	13.58	0.0180	13.66	0.0300
Abell 773	21.38	0	20.91	0	15.46	0.0850	15.32	0.0970	15.13	0.0890

Table 4—Continued

Name Cluster Name	Flux NUV (mag)	Error NUV (mag)	Flux FUV (mag)	Error FUV (mag)	Flux J (mag)	Error J (mag)	Flux H (mag)	Error H (mag)	Flux K (mag)	Error K (mag)
Abell 907	21.19	0	20.83	0	15.19	0.0560	14.87	0.0600	14.67	0.0720
Abell 963	21.62	0.0411	21.97	0.0409	14.59	0.0320	14.35	0.0360	14.25	0.0309
Abell 1060	17.74	0.0507	18.49	0.1080	11.33	0.0200	11.32	0.0200	11.52	0.0300
Abell 1063S	21.67	0	21.20	0	15.89	0.1430	15.33	0.1240	15.52	0.1680
Abell 1068	19.39	0.0322	14.04	0.0170	13.86	0.0220	13.73	0.0210
Abell 1201	21.51	0	21.05	0	15.17	0.0480	14.99	0.0690	14.75	0.0590
Abell 1204 ^a	21.33	0.0605	21.24	0.0694	15.35	0.0340	15.31	0.0520	15.19	0.0505
Abell 1240
Abell 1361	21.32	0	20.87	0	14.84	0.0380	14.64	0.0540	14.56	0.0550
Abell 1413	20.67	0.0858	21.10	0.1193	13.77	0.0130	13.52	0.0160	13.54	0.0183
Abell 1423	21.43	0	20.97	0	15.64	0.0760	15.27	0.0770	15.09	0.0790
Abell 1446	21.33	0.3012	20.89	0	14.10	0.0150	13.99	0.0220	14.00	0.0213
Abell 1569	20.94	0.2780	20.89	0	14.10	0.0110	13.86	0.0150	14.03	0.0157
Abell 1576
Abell 1644	18.90	0.0421	19.67	0.2327	12.38	0.0060	12.19	0.0060	12.41	0.0087
Abell 1650	21.45	0	20.99	0	14.34	0.0290	14.07	0.0350	14.23	0.0540
Abell 1651
Abell 1664	17.77	0.0194	18.16	0.0336	14.28	0.0290	14.11	0.0350	14.42	0.0378
Abell 1689	21.28	0	20.84	0	15.30	0.0660	15.16	0.0860	14.88	0.0920
Abell 1736	19.51	0.1769	20.59	0	12.77	0.0050	12.57	0.0060	12.77	0.0089
Abell 1758
Abell 1763	22.27	0.07	22.56	0.13	16.07	0.0870	16.08	0.1100	15.06	0.0709
Abell 1795	18.00	0.0287	18.48	0.1079	13.25	0.0070	12.96	0.0080	13.12	0.0105
Abell 1835	18.92	0.0179	19.15	0.0297	14.93	0.0380	14.62	0.0430	14.58	0.0468
Abell 1914	22.46	0.1264	22.98	0.1598	15.56	0.0400	15.35	0.0460	15.49	0.0682
Abell 1942	23.27	0	23.19	0.3217	15.47	0.0900	15.44	0.1180	14.94	0.0960
Abell 1991	19.71	0.0619	21.14	0	13.05	0.0080	12.82	0.0080	13.04	0.0138
Abell 1995	23.07	0.2903	23.30	0.3020	16.15	0.0660	15.77	0.0710	15.50	0.0569
Abell 2029 ^a	19.14	0.0473	19.99	0.0797	12.56	0.0060	12.32	0.0060	12.42	0.0096
Abell 2034	21.65	0	21.18	0	15.04	0.0460	14.81	0.0570	14.78	0.0630
Abell 2052 ^a	19.12	0.1005	19.47	0.1726	12.22	0.0050	12.02	0.0050	12.23	0.0074
Abell 2063	19.06	0.0298	20.77	0	12.48	0.0050	12.29	0.0060	12.53	0.0094
Abell 2065	21.19	0.3182	20.96	0	14.21	0.0333	13.99	0.0474	14.04	0.0406
Abell 2069	21.54	0	21.09	0	14.79	0.0390	14.46	0.0480	14.55	0.0510
Abell 2104	19.02	0	19.08	0	15.53	0.0880	15.12	0.0830	15.06	0.1090
Abell 2107	19.26	0.1134	20.05	0.2199	12.21	0.0040	11.99	0.0040	12.21	0.0065
Abell 2111	22.61	0.0996	23.69	0.2615	15.38	0.0560	15.26	0.0790	14.78	0.0601
Abell 2124	20.08	0.1435	20.17	0.1617	13.05	0.0070	12.88	0.0090	12.96	0.0091
Abell 2125	21.38	0	20.94	0	15.50	0.0860	15.20	0.0930	15.10	0.1070
Abell 2142 ^a	20.48	0.0320	21.44	0.0714	13.73	0.0150	13.56	0.0170	13.65	0.0250
Abell 2147	19.20	0.0797	20.36	0.2335	12.44	0.0040	12.25	0.0050	12.43	0.0068
Abell 2151	19.43	0.1109	21.00	0	12.37	0.0040	12.20	0.0050	12.39	0.0058
Abell 2163
Abell 2187	21.06	0.1970	21.26	0.4139	14.69	0.0250	14.49	0.0280	14.38	0.0326

Table 4—Continued

Name Cluster Name	Flux NUV (mag)	Error NUV (mag)	Flux FUV (mag)	Error FUV (mag)	Flux J (mag)	Error J (mag)	Flux H (mag)	Error H (mag)	Flux K (mag)	Error K (mag)
Abell 2199	18.42	0.0685	19.15	0.0516	11.68	0.0030	11.45	0.0040	11.67	0.0045
Abell 2204
Abell 2218	22.27	0.0709	23.58	0.3181
Abell 2219	23.03	0	23.02	0	15.83	0.1060	15.24	0.0970	15.38	0.1270
Abell 2244
Abell 2255	20.61	0.0353	21.54	0.0876	14.76	0.0270	14.49	0.0360	14.53	0.0396
Abell 2256	20.05	0.1159	20.60	0.2400	13.06	0.0210	12.82	0.0240	13.01	0.0290
Abell 2259	21.37	0	20.95	0	15.04	0.0490	14.78	0.0530	14.72	0.0610
Abell 2261
Abell 2294
Abell 2319	22.47	0	20.58	0.1400	13.85	0.0180	13.56	0.0200	13.68	0.0240
Abell 2384
Abell 2390	19.63	0.0462	19.70	0.0443	15.17	0.0540	15.23	0.0690	14.59	0.0508
Abell 2409	20.71	0	20.46	0	15.23	0.0730	15.10	0.0950	14.83	0.0910
Abell 2420
Abell 2462	20.30	0.1821	21.30	0.3477	13.47	0.0100	13.28	0.0140	13.41	0.0147
Abell 2537
Abell 2554	21.12	0.2837	21.17	0	14.14	0.0170	13.90	0.0270	14.07	0.0273
Abell 2556	20.68	0.2537	21.14	0.3075	13.71	0.0150	13.60	0.0230	13.67	0.0224
Abell 2589	19.39	0.0912	20.00	0.0780	12.46	0.0050	12.23	0.0050	12.45	0.0084
Abell 2597 ^a	18.68	0.0210	18.95	0.0303	13.91	0.0200	13.92	0.0320	13.90	0.0301
Abell 2626	19.17	0.1195	20.04	0.2993	12.77	0.0070	12.56	0.0090	12.78	0.0113
Abell 2631	22.48	0	23.03	0	16.21	0.1430	15.81	0.1490	15.68	0.1470
Abell 2657	20.76	0	20.55	0	14.07	0.0250	13.83	0.0310	13.96	0.0380
Abell 2667	20.64	0.1827	19.83	0.1478	15.11	0.0490	15.24	0.0920	14.85	0.0666
Abell 2717	20.01	0.2005	20.94	0	13.03	0.0070	12.79	0.0080	12.89	0.0121
Abell 2744a
Abell 2744b
Abell 2813	21.35	0	20.90	0	16.82	0.2460	16.70	0.3290	15.84	0.1620
Abell 3084	20.94	0.09	22	0.3	14.61	0.0310	14.09	0.0320	14.05	0.0324
Abell 3088
Abell 3112 ^a	19.81	0.0371	20.18	0.0596	13.17	0.0080	13.00	0.0090	12.99	0.0109
Abell 3120	20.10	0.0925	20.93	0.1769	13.52	0.0120	13.30	0.0130	13.41	0.0166
Abell 3158	20.02	0.1791	19.78	0.1559	13.00	0.0080	12.69	0.0100	12.92	0.0117
Abell 3266	19.40	0.0336	20.37	0.0786	12.54	0.0050	12.29	0.0060	12.43	0.0084
Abell 3364
Abell 3376	19.55	0.0510	20.27	0.0882	13.20	0.0110	12.98	0.0120	13.17	0.0162
Abell 3391
Abell 3395
Abell 3528S	18.58	0.0317	19.84	0.0860	11.91	0.0040	11.70	0.0040	11.96	0.0059
Abell 3558	18.99	0.0625	19.70	0.1114	12.16	0.0040	11.94	0.0040	12.16	0.0069
Abell 3562	19.63	0.1968	20.60	0	12.90	0.0070	12.70	0.0070	12.90	0.0102
Abell 3571
Abell 3581	18.06	0.0824	19.21	0.1843	11.82	0.0030	11.61	0.0030	11.87	0.0046

Table 4—Continued

Name	Flux	Error	Flux	Error	Flux	Error	Flux	Error	Flux	Error
Cluster Name	NUV	NUV	FUV	FUV	J	J	H	H	K	K
	(mag)	(mag)	(mag)	(mag)	(mag)	(mag)	(mag)	(mag)	(mag)	(mag)
MACS J1931.8-2634
MACS J2049.9-3217
MACS J2211.7-0349
MACS J2214.9-1359
MACS J2228+2036
MACS J2229.7-2755	20.48	0.0733	20.24	0.0631	15.88	0.0720	15.42	0.0800	14.94	0.0616
MACS J2245.0+2637	21.19	0	20.83	0	15.99	0.1200	16.00	0.1860	15.52	0.1410
MKW3S ^a	19.59	0.0366	20.50	0.0754	12.88	0.0060	12.66	0.0070	12.90	0.0112
MKW 04 ^a	18.03	0.0132	18.59	0.0281	11.19	0.0020	10.97	0.0020	11.20	0.0029
MKW 08	18.61	0.0285	19.50	0.0785	12.53	0.0070	12.35	0.0080	12.50	0.0107
MS 0016.9+1609
MS 0116.3-0115	19.39	0.0267	20.18	0.0363	12.59	0.0050	12.39	0.0060	12.62	0.0078
MS 0440.5+0204	20.22	0	20.32	0	14.38	0.0440	14.13	0.0470	13.99	0.0470
MS 0451.6-0305
MS 0735.6+7421	21.84	0.2980	21.14	0.2261	15.42	0.0500	15.15	0.0680	15.02	0.0625
MS 0839.8+2938 ^a	20.89	0.2499	20.67	0.2304	15.13	0.0280	14.93	0.0320	15.00	0.0386
MS 0906.5+1110
MS 1006.0+1202
MS 1008.1-1224
MS 1455.0+2232 ^a	20.22	0.0337	20.09	0.0460	15.44	0.1020	15.33	0.1398	14.92	0.1033
MS 2137.3-2353	21.54	0.0482	21.45	0.0294	15.89	0.0640	15.65	0.0790	15.16	0.0643
MS J1157.3+5531	20.96	0.1020	21.30	0	13.67	0.0178	13.40	0.0218	13.54	0.0248
NGC 507	17.91	0.0178	19.08	0.0486	-0.02	0.0010	10.79	0.0020	11.05	0.0018
NGC 4636	16.65	0.0285	17.46	0.0685	9.93	0.0200	9.88	0.0200	10.05	0.0300
NGC 5044	17.13	0.0121	17.94	0.0284	10.44	0.0010	10.26	0.0010	10.54	0.0019
NGC 5813	17.23	0.0099	18.42	0.0249	10.26	0.0300	10.29	0.0300	10.50	0.0300
NGC 5846	16.80	0.0101	17.51	0.0270	9.98	0.0010	9.78	0.0010	10.06	0.0011
OPHIUCHUS	16.24	0.2065	17.80	0	11.04	0.0080	11.22	0.0070	12.06	0.0072
PKS 0745-191
RBS 0461	18.19	0	18.46	0	13.32	0.0110	12.97	0.0110	13.01	0.0170
RBS 0533	17.28	0.0612	18.10	0.1333	10.85	0.0020	10.71	0.0020	11.07	0.0024
RBS 0797	21.30	0	20.40	0.2609
RCS J2327-0204	19.52	0.0512	20.08	0.0805
RXCJ0331.1-2100
RXC J1023.8-2715	20.74	0.3265	20.32	0.2099	15.23	0.0590	15.15	0.0680	15.11	0.0758
RX J0220.9-3829
RX J0232.2-4420
RX J0439+0520	19.93	0	19.88	0	15.48	0.0910	15.22	0.1110	14.89	0.1000
RX J0439.0+0715
RX J0528.9-3927
RX J0647.7+7015
RX J0819.6+6336	21.13	0	20.73	0	14.32	0.0240	14.06	0.0280	14.06	0.0310
RX J1000.4+4409	22.27	0.1729	20.97	0	0.03
RX J1022.1+3830	20.11	0.2209	20.92	0	13.16	0.0080	12.94	0.0100	13.16	0.0110

Table 4—Continued

Name Cluster Name	Flux NUV (mag)	Error NUV (mag)	Flux FUV (mag)	Error FUV (mag)	Flux J (mag)	Error J (mag)	Flux H (mag)	Error H (mag)	Flux K (mag)	Error K (mag)
RX J1130.0+3637	20.75	0.1684	20.84	0	14.35	0.0210	14.16	0.0280	14.19	0.0297
RX J1320.2+3308	21.40	0	20.88	0.2884	13.52	0.0110	13.27	0.0120	13.41	0.0170
RX J1347.5-1145 ^a	21.03	0.0534	21.39	0.0661
RX J1423.8+2404
RX J1504.1-0248	17.69	0.0118	17.53	0.0203	15.07	0.0510	14.78	0.0450	15.12	0.0692
RX J1532.9+3021
RX J1539.5-8335
RX J1720.1+2638	19.73	0.1018	20.72	0.2954	14.02	0.0210	13.85	0.0230	14.02	0.0288
RX J1720.2+3536
RX J1852.1+5711	21.34	0	20.95	0	15.21	0.0560	14.97	0.0630	14.95	0.0880
RX J2129.6+0005	21.37	0.0988	21.21	0.0766	14.86	0.0440	14.52	0.0490	14.87	0.0529
SC 1327-312	19.72	0.0616	20.72	0.1747	13.31	0.0090	13.14	0.0100	13.27	0.0162
SERSIC 159-03	19.06	0.0141	19.41	0.0229	13.12	0.0080	12.88	0.0090	13.09	0.0133
SS2B153	17.86	0.0451	18.51	0.0992	11.16	0.0020	10.96	0.0020	11.23	0.0026
UGC 03957	18.83	0.0630	19.89	0.1925	11.92	0.0030	11.72	0.0040	11.96	0.0041
UGC 12491
ZWCL 1215	21.28	0	20.82	0	14.27	0.0290	14.01	0.0320	14.02	0.0440
ZWCL 1358+6245 ^a	23.56	0.2803	23.16	0.1521
ZWCL 1742
ZWCL 1953
ZWCL 3146 ^a	19.38	0.0236	19.18	0.0249	15.87	0.0940	14.83	0.0620	14.97	0.0878
ZWICKY 2701	21.43	0	20.95	0	15.73	0.1110	15.62	0.1700	15.33	0.1210
ZwCl 0857.9+2107	20.10	0.0320	19.77	0.0246	15.71	0.0760	15.85	0.0910	15.13	0.0681

^aBCGs are also in the Hicks et al. (2010) sample.

^bBCG *GALEX* fluxes are taken from Hicks et al. (2010).

Note. — Fluxes reported with errors equal to 0 are 3σ upper limits. For NUV upper limits, the *2MASS* flux is matched with a $7''$ aperture such that it is similar in size to the *GALEX* PSF.

Table 5. *Spitzer* Aperture Flux.

Name	Flux	Error	Flux	Error	Flux	Error	Flux	Error	Flux	Error	Flux	Error	Flux	Error
Cluster Name	$3.6\mu m$	$3.6\mu m$	$4.5\mu m$	$4.5\mu m$	$5.8\mu m$	$5.8\mu m$	$8.0\mu m$	$8.0\mu m$	$24\mu m$	$24\mu m$	$70\mu m$	$70\mu m$	$160\mu m$	$160\mu m$
	(mJy)	(mJy)	(mJy)	(mJy)	(mJy)	(mJy)	(mJy)	(mJy)	(mJy)	(mJy)	(mJy)	(mJy)	(mJy)	(mJy)
1E0657 56a	0.47	0.02	0.38	0.02	0.22	0.01	0.14	0.01	0.15	0.02	5.29	0
1E0657 56b	0.57	0.03	0.46	0.02	0.26	0.01	0.17	0.01	0.11	0.02	1.43 ^a	0
2A 0335+096	26.12	1.31	15.93	0.80	14.79	0.74	9.94	0.50	2.40 ^b	0.24	77.10	20.36
2PIGG J0011.5-2850
2PIGG J2227.0-3041
3C 28.0	0.88	0.04	0.67	0.03	0.35	0.02	0.43	0.02	0.55 ^c	0.08	6.78	0
3C 295
3C 388	6.20	0.31	4.11	0.21	2.70	0.13	1.88	0.09	2.15	0.22	18.79 ^d	4.16	7.13	0
4C 55.16
Abell 13
Abell 68	1.28	0.15
Abell 85	15.08	0.75	9.43	0.47	6.79	0.34	4.36	0.22	1.51 ^b	0.16	17.17 ^d	3.88
Abell 119
Abell 133
Abell 141
Abell 160
Abell 193
Abell 209	1.35	0.07	1.04	0.05	0.58	0.03	0.44	0.02	0.24	0.03
Abell 222
Abell 223
Abell 262	73.01	3.65	43.31	2.17	34.50	1.72	22.20	1.11	4.08	0.41	90.28	24.05
Abell 267	1.37	0.07	1.07	0.05	0.65	0.03	0.44	0.02	0.14	0.06
Abell 368	0.59	0.06
Abell 370	0.79	0.04	0.66	0.03	0.41	0.02	0.26	0.01	0.08 ^b	0.03	2.44	0	6.13 ^a	0
Abell 383	1.60	0.08	1.20	0.06	0.73	0.04	0.61	0.03	0.51 ^b	0.05
Abell 399
Abell 400
Abell 401	0.49	0	5.33	0
Abell 426 ^e	143.49	7.17	124.20	6.21	208.70	10.44	356.70	17.84	2864.10	286.41	6312.40	1264.04	4115.45	824.60

Table 5—Continued

Name	Flux	Error	Flux	Error	Flux	Error	Flux	Error	Flux	Error	Flux	Error	Flux	Error
Cluster Name	$3.6\mu m$	$3.6\mu m$	$4.5\mu m$	$4.5\mu m$	$5.8\mu m$	$5.8\mu m$	$8.0\mu m$	$8.0\mu m$	$24\mu m$	$24\mu m$	$70\mu m$	$70\mu m$	$160\mu m$	$160\mu m$
	(mJy)	(mJy)	(mJy)	(mJy)	(mJy)	(mJy)	(mJy)	(mJy)	(mJy)	(mJy)	(mJy)	(mJy)	(mJy)	(mJy)
Abell 478	5.03	0.25	3.34	0.17	2.46	0.12	2.35	0.12	1.59 ^b	0.16	35.86 ^d	7.28	48.36 ^d	9.67
Abell 496	33.00	1.65	19.72	0.99	15.18	0.76	9.34	0.47
Abell 520 ^e
Abell 521	4.90	0.49
Abell 539
Abell 562
Abell 576
Abell 586	0.70	0.09 ^b
Abell 611	0.28	0.23
Abell 644
Abell 665	0.08	0.20
Abell 697	1.27	0.06	1.03	0.05	0.61	0.03	0.40	0.02	0.38	0.04
Abell 744
Abell 754
Abell 773	1.28	0.06	0.99	0.05	0.59	0.03	0.38	0.02	0.30	0.04
Abell 907
Abell 963	1.71	0.09	1.32	0.07	0.76	0.04	0.54	0.03
Abell 1060
Abell 1063S	1.09	0.05	0.87	0.04	0.54	0.03	0.34	0.02	0.06	0.01
Abell 1068	3.15	0.16	2.77	0.14	3.40	0.17	8.50	0.43	74.78 ^c	7.48	894.50	179.71
Abell 1201
Abell 1204	1.03	0.05	0.79	0.04	0.50	0.02	0.42	0.02	1.47	0.16	26.06 ^d	5.40
Abell 1240
Abell 1361	2.61	0.13	1.81	0.09	1.14	0.06	0.80	0.04	0.66 ^b	0.08	20.78 ^d	4.48
Abell 1413
Abell 1423
Abell 1446
Abell 1569
Abell 1576

Table 5—Continued

Name	Flux	Error	Flux	Error	Flux	Error	Flux	Error	Flux	Error	Flux	Error	Flux	Error
Cluster Name	$3.6\mu\text{m}$	$3.6\mu\text{m}$	$4.5\mu\text{m}$	$4.5\mu\text{m}$	$5.8\mu\text{m}$	$5.8\mu\text{m}$	$8.0\mu\text{m}$	$8.0\mu\text{m}$	$24\mu\text{m}$	$24\mu\text{m}$	$70\mu\text{m}$	$70\mu\text{m}$	$160\mu\text{m}$	$160\mu\text{m}$
	(mJy)	(mJy)	(mJy)	(mJy)	(mJy)	(mJy)	(mJy)	(mJy)	(mJy)	(mJy)	(mJy)	(mJy)	(mJy)	(mJy)
Abell 1644	2.24	0.11	1.58	0.08	1.27	0.06	2.49	0.12
Abell 1650
Abell 1651
Abell 1664	4.08	0.41	85.52	23.12
Abell 1689	1.35	0.07	1.01	0.05	0.59	0.03	0.39	0.02	0.92 ^b	0.09	1.74	0	4.43	0
Abell 1736
Abell 1758	0.80	0.04	0.65	0.03	0.38	0.02	0.23	0.01	0.23	0.03
Abell 1763	1.45	0.07	1.12	0.06	0.61	0.03	0.36	0.02	0.33	0.10	8.07	0	28.28	0
Abell 1795	2.17	0.25	37.21	0
Abell 1835	1.93	0.10	1.83	0.09	1.29	0.06	4.53	0.23	17.80 ^c	1.78	175.07	36.14	317.29	64.16
Abell 1914	0.98	0.05	0.70	0.04	0.39	0.02	0.26	0.01	0.12 ^b	0.01
Abell 1942
Abell 1991	8.99	0.45	5.64	0.28	3.88	0.19	2.54	0.13
Abell 1995
Abell 2029	1.07	0.19	14.88	0	46.57	0
Abell 2034
Abell 2052	25.15	1.26	15.23	0.76	11.58	0.58	7.85	0.39	4.91	0.49	28.97 ^d	6.08
Abell 2063	1.11	0.13	14.61 ^a	0
Abell 2065
Abell 2069
Abell 2104	1.42	0.07	1.07	0.05	0.66	0.03	0.42	0.02
Abell 2107	1.56 ^b	0.16	6.23 ^a	0
Abell 2111
Abell 2124
Abell 2125	0.28 ^b	0.03
Abell 2142	0.54 ^b	0.08	8.38 ^a	0
Abell 2147
Abell 2151	0.93 ^b	0.13	22.08	0	65.70	0
Abell 2163

Table 5—Continued

Name	Flux	Error	Flux	Error	Flux	Error	Flux	Error	Flux	Error	Flux	Error	Flux	Error
Cluster Name	$3.6\mu m$	$3.6\mu m$	$4.5\mu m$	$4.5\mu m$	$5.8\mu m$	$5.8\mu m$	$8.0\mu m$	$8.0\mu m$	$24\mu m$	$24\mu m$	$70\mu m$	$70\mu m$	$160\mu m$	$160\mu m$
	(mJy)	(mJy)	(mJy)	(mJy)	(mJy)	(mJy)	(mJy)	(mJy)	(mJy)	(mJy)	(mJy)	(mJy)	(mJy)	(mJy)
Abell 2187
Abell 2199 ^e	46.60	2.33	28.35	1.42	21.31	1.07	14.38	0.72	5.06 ^f	0.51	173.77	37.61
Abell 2204	1.71	0.09	1.19	0.06	0.76	0.04	0.68	0.03	2.46	0.25	47.57 ^d	9.92
Abell 2218	1.12	0.06	0.82	0.04	0.48	0.02	0.32	0.02	0.05	0	46.12	0	46.57	0
Abell 2219	1.00	0.05	0.77	0.04	0.43	0.02	0.29	0.01	0.29	0.03
Abell 2244
Abell 2255	0.31	0.05	9.03 ^a	0
Abell 2256
Abell 2259
Abell 2261	2.03	0.10	1.57	0.08	0.87	0.04	0.60	0.03	0.44	0.05	3.29	0	38.02 ^a	0
Abell 2294
Abell 2319
Abell 2384
Abell 2390	1.01	0.05	0.80	0.04	0.50	0.03	0.62	0.03	1.23 ^c	0.12	48.80	12.59	120.01	24.00
Abell 2409
Abell 2420
Abell 2462
Abell 2537	0.04	0.02
Abell 2554
Abell 2556
Abell 2589
Abell 2597	3.69	0.18	2.48	0.12	2.05	0.10	2.05	0.10	2.36 ^c	0.25	62.87 ^d	19.09	42.05	10.28
Abell 2626	10.76	0.54	6.80	0.34	4.85	0.24	3.00	0.15	1.34 ^b	0.14	5.96	0
Abell 2631
Abell 2657
Abell 2667	0.76	0.04	0.61	0.03	0.46	0.02	0.62	0.03	8.19 ^f	0.82
Abell 2717
Abell 2744a	0.65	0.03225	0.52	0.03	0.32	0.02	0.21	0.01	0.48 ^b	0.05	4.29 ^a	0	23.63 ^a	0
Abell 2744b	0.64	0.03	0.52	0.03	0.32	0.02	0.20	0.01	0.09	0	2.34	0	6.99	0

Table 5—Continued

Name	Flux	Error	Flux	Error	Flux	Error	Flux	Error	Flux	Error	Flux	Error	Flux	Error
Cluster Name	$3.6\mu m$	$3.6\mu m$	$4.5\mu m$	$4.5\mu m$	$5.8\mu m$	$5.8\mu m$	$8.0\mu m$	$8.0\mu m$	$24\mu m$	$24\mu m$	$70\mu m$	$70\mu m$	$160\mu m$	$160\mu m$
	(mJy)	(mJy)	(mJy)	(mJy)	(mJy)	(mJy)	(mJy)	(mJy)	(mJy)	(mJy)	(mJy)	(mJy)	(mJy)	(mJy)
Abell 2813
Abell 3084	0.41	0.07
Abell 3088	0.40 ^b	0.05
Abell 3112	7.80	0.39	5.12	0.26	3.53	0.18	2.92	0.15	3.07	0.31	5.96 ^a	0
Abell 3120
Abell 3158	0.70 ^b	0.10	21.59	0	40.12	0
Abell 3266	2.64 ^b	0.30	14.88	0	42.60	0
Abell 3364	0.18	0.06
Abell 3376
Abell 3391	1.75	0.18	1.31	0	25.24 ^a	0
Abell 3395
Abell 3528S
Abell 3558
Abell 3562
Abell 3571
Abell 3581
Abell 3667
Abell 3822
Abell 3827
Abell 3921
Abell 4038
Abell 4059	18.05	0.90	11.23	0.56	7.91	0.40	5.78	0.29	1.83	0.19	13.41 ^d	2.98
Abell S0405
Abell S0592	0.16	0.02
AC 114	0.93	0.05	0.75	0.04	0.46	0.02	0.31	0.02	0.10	0.01
AWM7
CENTAURUS	328.00	16.40	191.00	9.55	162.00	8.10	100.00	5.00	25.60 ^f	3.00	165.00	41.28	256.00	60.15
CID 0072	19.16	0.96	11.47	0.57	8.50	0.42	5.64	0.28	1.13 ^b	0.12	5.78 ^a	0
CL J1226.9+3332	0.48	0.02	0.33	0.02	0.25	0.01	0.14	0.01	0.20 ^b	0.03	3.66	0	30.13 ^a	0

Table 5—Continued

Name	Flux	Error	Flux	Error	Flux	Error	Flux	Error	Flux	Error	Flux	Error	Flux	Error
Cluster Name	$3.6\mu m$	$3.6\mu m$	$4.5\mu m$	$4.5\mu m$	$5.8\mu m$	$5.8\mu m$	$8.0\mu m$	$8.0\mu m$	$24\mu m$	$24\mu m$	$70\mu m$	$70\mu m$	$160\mu m$	$160\mu m$
	(mJy)	(mJy)	(mJy)	(mJy)	(mJy)	(mJy)	(mJy)	(mJy)	(mJy)	(mJy)	(mJy)	(mJy)	(mJy)	(mJy)
CYGNUS A	16.32	0.82	59.12	2.96	677.50	67.75	1394.46	280.16	454.29	94.03
ESO 3060170
ESO 5520200
EXO 0422-086
HCG 0062	115.00	5.75	68.24	3.41	52.61	2.63	74.77	3.74	13.28 ^f	1.36	24.05	0
HCG 42 ^e	158.20	7.91	92.28	4.61	77.33	3.87	45.45	2.27	12.40 ^f	1.31	8.58	0
HERCULES A	0.91	0.05	0.43	0.02	0.17	0.02
HYDRA A	7.74	0.39	6.86	0.34	9.15 ^c	0.92	155.18	36.56	181.77	38.98
M49 ^e	2042.00	102.10	1195.00	59.75	564.00	28.20	754.00	37.70	924.50 ^f	92.48	205.24	43.76	26.98	5.90
M87 ^e	1502.00	75.10	890.50	44.53	905.80	45.29	493.30	24.67	256.17 ^f	25.62	395.40	83.69	588.32	119.94
MACS J0011.7-1523
MACS J0035.4-2015
MACS J0159.8-0849
MACS J0242.5-2132
MACS J0257.1-2325
MACS J0257.6-2209
MACS J0308.9+2645
MACS J0329.6-0211
MACS J0417.5-1154
MACS J0429.6-0253
MACS J0520.7-1328
MACS J0547.0-3904
MACS J0717.5+3745
MACS J0744.8+3927
MACS J1115.2+5320
MACS J1115.8+0129
MACS J1131.8-1955
MACS J1149.5+2223
MACS J1206.2-0847

Table 5—Continued

Name	Flux	Error	Flux	Error	Flux	Error	Flux	Error	Flux	Error	Flux	Error	Flux	Error
Cluster Name	$3.6\mu m$	$3.6\mu m$	$4.5\mu m$	$4.5\mu m$	$5.8\mu m$	$5.8\mu m$	$8.0\mu m$	$8.0\mu m$	$24\mu m$	$24\mu m$	$70\mu m$	$70\mu m$	$160\mu m$	$160\mu m$
	(mJy)	(mJy)	(mJy)	(mJy)	(mJy)	(mJy)	(mJy)	(mJy)	(mJy)	(mJy)	(mJy)	(mJy)	(mJy)	(mJy)
MACS J1311.0-0310
MACS J1621.3+3810
MACS J1931.8-2634
MACS J2049.9-3217
MACS J2211.7-0349	0.22	0.14
MACS J2214.9-1359
MACS J2228+2036
MACS J2229.7-2755
MACS J2245.0+2637
MKW3S
MKW 04 ^e	87.04	4.35	51.15	2.56	39.97	2.00	24.80	1.24	3.57	0.37	7.29	0	23.43	0
MKW 08
MS 0016.9+1609
MS 0116.3-0115
MS 0440.5+0204
MS 0451.6-0305	0.36	0.02	0.25	0.01	0.18	0.01	0.11	0.01	0.15 ^b	0.02	2.23 ^a	0	2.68 ^a	0
MS 0735.6+7421	0.92	0.05	0.71	0.04	0.44	0.02	0.33	0.02
MS 0839.8+2938	0.35	0.05
MS 0906.5+1110	0.48	0
MS 1006.0+1202
MS 1008.1-1224	0.78	0.04	0.62	0.03	0.38	0.02	0.26	0.01
MS 1455.0+2232	1.13	0.06	0.91	0.05	0.55	0.03	0.45	0.02	0.62	0.09
MS 2137.3-2353	0.81	0.04	0.64	0.03	0.44	0.02	0.27	0.01	0.58	0.13
MS J1157.3+5531
NGC 0507 ^e	98.66	4.93	59.01	2.95	49.18	2.46	28.78	1.44	8.27 ^f	0.83	4.15	0	2.19	0
NGC 4636	992.05	49.60	634.90	31.74	371.46	18.57	277.01	13.85 ^f	22.56	2.26	168.85	43.86	181.33	48.45
NGC 5044	244.53	12.23	143.78	7.19	121.75	6.09	76.38	3.82	32.24 ^f	3.23	140.06	29.34	251.76	50.82
NGC 5813 ^e	323.11	16.16	189.30	9.47	167.55	8.38	98.08	4.90	29.22 ^f	2.93	76.25	29.14	137.18	59.69
NGC 5846 ^e	534.30	26.72	310.56	15.53	282.50	14.13	162.40	8.12	57.03 ^f	5.71	219.11	50.86	287.15	71.78

Table 5—Continued

Name	Flux	Error	Flux	Error	Flux	Error	Flux	Error	Flux	Error	Flux	Error	Flux	Error
Cluster Name	$3.6\mu m$	$3.6\mu m$	$4.5\mu m$	$4.5\mu m$	$5.8\mu m$	$5.8\mu m$	$8.0\mu m$	$8.0\mu m$	$24\mu m$	$24\mu m$	$70\mu m$	$70\mu m$	$160\mu m$	$160\mu m$
	(mJy)	(mJy)	(mJy)	(mJy)	(mJy)	(mJy)	(mJy)	(mJy)	(mJy)	(mJy)	(mJy)	(mJy)	(mJy)	(mJy)
OPHIUCHUS
PKS 0745-191	4.51	0.23	3.16	0.16	2.31	0.12	2.93	0.15	10.22 ^b	1.02	154.33	34.50
RBS 0461
RBS 0533
RBS 0797
RCS J2327-0204
RXCJ0331.1-2100	2.28	0.23
RXC J1023.8-2715
RX J0220.9-3829
RX J0232.2-4420
RX J0439+0520	1.35	0.07	1.08	0.05	0.67	0.03	0.73	0.04	2.05	0.23	14.14 ^d	2.97
RX J0439.0+0715
RX J0528.9-3927
RX J0647.7+7015
RX J0819.6+6336
RX J1000.4+4409
RX J1022.1+3830
RX J1130.0+3637
RX J1320.2+3308
RX J1347.5-1145	0.23	0.01	0.17	0.01	0.13	0.01	0.09	0
RX J1423.8+2404
RX J1504.1-0248	1.50	0.15
RX J1532.9+3021	0.69	0.03	0.61	0.03	0.39	0.02	0.80	0.04	3.76 ^c	0.38	90.71	18.14
RX J1539.5-8335
RX J1720.1+2638	0.55	0.08	6.92	0
RX J1720.2+3536
RX J1852.1+5711
RX J2129.6+0005	1.10	0.05	0.87	0.04	0.50	0.02	0.39	0.02	1.13	0.11	6.18	0
SC 1327-312

Table 5—Continued

Name	Flux	Error	Flux	Error	Flux	Error	Flux	Error	Flux	Error	Flux	Error	Flux	Error
Cluster Name	$3.6\mu m$	$3.6\mu m$	$4.5\mu m$	$4.5\mu m$	$5.8\mu m$	$5.8\mu m$	$8.0\mu m$	$8.0\mu m$	$24\mu m$	$24\mu m$	$70\mu m$	$70\mu m$	$160\mu m$	$160\mu m$
	(mJy)	(mJy)	(mJy)	(mJy)	(mJy)	(mJy)	(mJy)	(mJy)	(mJy)	(mJy)	(mJy)	(mJy)	(mJy)	(mJy)
SERSIC 159-03	8.69	0.43	5.45	0.27	3.85	0.19	2.75	0.14	1.22	0.13	15.51 ^d	3.43
SS2B153
UGC 03957
UGC 12491
ZWCL 1215
ZWCL 1358+6245	0.38	0.02	0.30	0.02	0.19	0.01	0.12	0.01	0.19	0.03
ZWCL 1742	4.66	0.23	3.09	0.15	2.25	0.11	2.14	0.11	3.23 ^b	0.32	27.36 ^d	5.80
ZWCL 1953
ZWCL 3146	0.84	0.04	0.76	0.04	0.51	0.03	1.20	0.06	4.35 ^c	0.44	46.42	14.05	156.84	38.26
ZWICKY 2701	1.02	0.05	0.76	0.04	0.46	0.02	0.31	0.02	0.20 ^b	0.05	6.67	0
ZwCl 0857.9+2107	0.82	0.04	1.01	0.05	1.58	0.08	3.56	0.18	33.03	3.30	214.18	42.84

^aOriginally, aperture flux measurement indicated a detection. However, 24 micron flux measurement and visual inspection indicated contamination in the aperture where flux is likely from an unrelated source. The reported measurement is now an upper limit computed using the point source estimate at $16''$.

^bSource not extended but has significant contamination. Point source measurement at $35''$ radius is greater than 10 percent error margin.

^cSource not extended but has mild source contamination. Point source measurement at $35''$ radius is within 10 percent error.

^dFlux measurement is a filtered detection.

^eIRAC flux measurements derived from a BCD image that was remosaicked.

^fSource is extended in the MIPS 24 micron image. 24 micron flux measured within the aperture (see Table 3). Note an aperture radius of $35''$ was used for NGC4636 because of significant point source contamination outside of

35''.

Note. — Fluxes reported with errors equal to 0 are 5σ upper limits.

Table 6. *2MASS* Aperture Flux.

Name Cluster Name	Flux J (mJy)	Error J (mJy)	Flux H (mJy)	Error H (mJy)	Flux K (mJy)	Error K (mJy)	Flux K24 (mJy)	Error K24 (mJy)
1E0657 56a
1E0657 56b
2A 0335+096	65.69	0.54	72.49	0.94	57.94	0.83	40.23	0.50
2PIGG J0011.5-2850	12.83	0.22	15.56	0.34	14.53	0.41
2PIGG J2227.0-3041	15.75	0.26	19.44	0.37	17.22	0.41
3C 28.0	1.26	0.12	1.64	0.17	1.68	0.19	3.35	0.51
3C 295	0.76	0.11	1.03	0.18	1.31	0.17
3C 388	10.31	0.18	12.48	0.28	11.57	0.32	15.38	0.49
4C 55.16	0.63	0.12	0.97	0.20	1.07	0.19
Abell 13	5.56	0.19	7.24	0.31	6.79	0.32
Abell 68	1.52	0.13	1.55	0.21	2.04	0.23	4.47	0.60
Abell 85	27.30	0.28	34.94	0.43	30.85	0.57	30.31	0.56
Abell 119	35.72	0.36	44.95	0.62	39.83	0.70
Abell 133	22.75	0.38	27.42	0.71	25.98	0.63
Abell 141	0.88	0.11	1.32	0.17	1.22	0.19
Abell 160	25.68	0.43	30.24	0.58	27.38	0.85
Abell 193	37.18	0.35	47.36	0.50	39.79	0.60
Abell 209	2.01	0.12	2.27	0.19	2.67	0.20	5.94	0.53
Abell 222	1.43	0.11	1.75	0.17	2.05	0.20
Abell 223	0.95	0.11	1.42	0.18	1.78	0.20
Abell 262	175.12	1.44	234.38	2.23	176.68	1.78	73.44	0.44
Abell 267	1.85	0.12	2.11	0.20	2.78	0.19	4.99	0.49
Abell 368
Abell 370	0.79	0.11	0.99	0.15	1.56	0.20	2.44	0.54
Abell 383	2.60	0.13	2.92	0.20	3.37	0.22	6.26	0.59
Abell 399	15.64	0.25	18.06	0.42	16.71	0.43
Abell 400	126.33	0.86	148.84	1.47	122.78	1.30
Abell 401	16.14	0.24	20.03	0.38	17.75	0.40	22.10	0.53
Abell 426	297.55	7.75	338.24	10.76	279.04	10.73	110.50	3.74
Abell 478	13.93	0.17	15.61	0.28	13.36	0.24	17.60	0.37
Abell 496	74.64	0.52	87.26	0.88	70.20	0.99
Abell 520	1.66	0.17	1.75	0.24	1.82	0.27
Abell 521	1.40	0.11	1.90	0.16	1.86	0.22	3.77	0.57
Abell 539	68.99	0.68	80.66	1.13	65.27	1.08
Abell 562	4.93	0.18	6.17	0.29	5.88	0.29
Abell 576	34.31	0.45	39.45	0.71	33.51	0.74
Abell 586	2.72	0.12	3.08	0.19	3.75	0.21	8.14	0.54
Abell 611	1.09	0.13	1.83	0.20	1.85	0.18	3.82	0.48
Abell 644	12.69	0.27	14.88	0.41	12.44	0.52
Abell 665	2.03	0.12	2.69	0.20	2.46	0.19	3.71	0.50
Abell 697	1.54	0.13	2.03	0.20	2.64	0.20	4.63	0.54
Abell 744	11.34	0.26	14.31	0.44	13.17	0.36
Abell 754	17.31	0.33	21.07	0.42	17.09	0.65
Abell 773	1.83	0.13	2.12	0.17	2.57	0.19	4.65	0.49

Table 6—Continued

Name Cluster Name	Flux J (mJy)	Error J (mJy)	Flux H (mJy)	Error H (mJy)	Flux K (mJy)	Error K (mJy)	Flux K24 (mJy)	Error K24 (mJy)
Abell 907	2.60	0.12	3.41	0.17	3.93	0.25
Abell 963	2.20	0.12	2.97	0.18	3.52	0.18
Abell 1060	284.71	12.60	277.40	13.40	246.57	17.61
Abell 1063S	1.15	0.15	1.99	0.22	1.84	0.25	4.09	0.66
Abell 1068	3.94	0.13	5.43	0.21	5.61	0.22	9.72	0.48
Abell 1201	2.30	0.10	2.75	0.17	3.38	0.18
Abell 1204	1.70	0.10	1.88	0.16	2.08	0.17	3.50	0.46
Abell 1240
Abell 1361	4.17	0.14	4.97	0.24	5.27	0.26	9.36	0.52
Abell 1413	4.80	0.12	6.13	0.19	5.75	0.21
Abell 1423	1.60	0.10	2.21	0.14	2.60	0.17
Abell 1446	6.18	0.17	6.99	0.28	7.15	0.27
Abell 1569	8.63	0.21	10.76	0.36	9.55	0.34
Abell 1576	1.34	0.11	1.49	0.18	2.37	0.18
Abell 1644	34.13	0.45	42.28	0.62	36.09	0.76
Abell 1650	8.54	0.23	10.86	0.36	9.06	0.47
Abell 1651	9.68	0.23	13.02	0.32	11.96	0.42
Abell 1664	3.64	0.15	4.50	0.26	4.32	0.26	6.52	0.54
Abell 1689	2.19	0.12	2.45	0.18	3.04	0.24	6.21	0.64
Abell 1736	35.70	0.53	42.11	0.72	37.68	1.02
Abell 1758	0.94	0.11	1.42	0.18	1.46	0.18	2.70	0.55
Abell 1763	0.64	0.08	0.75	0.13	1.23	0.15	2.63	0.39
Abell 1795	13.86	0.24	17.85	0.33	15.35	0.39	16.48	0.42
Abell 1835	2.41	0.14	2.81	0.20	3.59	0.26	5.37	0.69
Abell 1914	1.48	0.09	1.97	0.13	1.78	0.18	2.61	0.55
Abell 1942	1.89	0.14	2.04	0.19	2.87	0.24
Abell 1991	16.35	0.30	20.46	0.40	17.32	0.55
Abell 1995	0.74	0.10	0.89	0.14	1.50	0.15
Abell 2029	20.59	0.25	26.01	0.32	25.02	0.52	31.75	0.70
Abell 2034	5.30	0.15	6.67	0.23	6.57	0.26
Abell 2052	51.77	0.59	64.49	0.86	54.11	1.03	35.87	0.60
Abell 2063	40.82	0.54	48.63	0.83	40.55	0.99	27.79	0.61
Abell 2065	8.38	0.25	9.89	0.45	9.47	0.37
Abell 2069	4.50	0.15	6.00	0.26	5.47	0.25
Abell 2104	2.57	0.14	3.12	0.19	2.83	0.24
Abell 2107	45.92	0.41	56.67	0.56	48.82	0.80	39.08	0.57
Abell 2111	1.04	0.10	1.45	0.18	1.43	0.17
Abell 2124	15.29	0.25	18.53	0.37	17.63	0.36
Abell 2125	1.69	0.13	2.33	0.19	2.44	0.23	5.07	0.61
Abell 2142	7.03	0.21	8.82	0.29	7.40	0.38	10.61	0.58
Abell 2147	41.21	0.47	49.30	0.66	42.60	0.77
Abell 2151	45.08	0.43	53.44	0.70	46.29	0.70	31.18	0.46
Abell 2163
Abell 2187	2.38	0.11	3.14	0.15	3.39	0.19

Table 6—Continued

Name Cluster Name	Flux J (mJy)	Error J (mJy)	Flux H (mJy)	Error H (mJy)	Flux K (mJy)	Error K (mJy)	Flux K24 (mJy)	Error K24 (mJy)
Abell 2199	93.82	0.67	115.01	1.13	96.73	1.20	61.03	0.60
Abell 2204	3.27	0.11	3.40	0.17	3.37	0.21	11.15	0.52
Abell 2218
Abell 2219	1.26	0.12	1.95	0.19	1.92	0.21	4.73	0.56
Abell 2244	8.13	0.16	10.44	0.25	9.74	0.27
Abell 2255	4.17	0.23	5.27	0.39	4.72	0.41	5.71	0.57
Abell 2256	21.01	0.38	26.30	0.55	22.92	0.59
Abell 2259	2.75	0.12	3.51	0.16	3.86	0.19
Abell 2261	2.85	0.11	3.68	0.18	4.17	0.19	7.34	0.49
Abell 2294	3.62	0.13	4.31	0.19	4.95	0.23
Abell 2319	24.58	0.32	29.88	0.49	24.34	0.51
Abell 2384	4.82	0.18	5.40	0.31	5.61	0.34
Abell 2390	1.43	0.11	1.81	0.17	2.38	0.21	4.74	0.55
Abell 2409	2.68	0.16	3.04	0.23	3.80	0.27
Abell 2420	11.49	0.26	13.90	0.40	12.64	0.43
Abell 2462	12.91	0.27	15.73	0.47	14.29	0.46
Abell 2537	1.26	0.12	1.49	0.21	1.45	0.21	3.44	0.55
Abell 2554	5.39	0.17	6.07	0.32	6.03	0.31
Abell 2556	7.71	0.22	9.29	0.42	8.83	0.39
Abell 2589	36.96	0.45	46.09	0.61	38.49	0.88
Abell 2597	6.54	0.25	7.35	0.45	7.02	0.42	8.87	0.61
Abell 2626	21.15	0.32	25.97	0.52	22.67	0.58	22.86	0.59
Abell 2631	0.96	0.11	1.49	0.17	1.63	0.18
Abell 2657	24.29	0.51	27.73	0.78	22.12	0.83
Abell 2667	1.09	0.13	1.08	0.22	1.25	0.23	4.26	0.61
Abell 2717	20.25	0.35	25.45	0.49	23.37	0.73
Abell 2744a
Abell 2744b
Abell 2813	0.55	0.11	0.59	0.17	1.14	0.18
Abell 3084	3.56	0.21	4.89	0.31	5.58	0.35	7.66	0.58
Abell 3088	0.94	0.12	1.09	0.20	1.37	0.24	3.82	0.65
Abell 3112	13.58	0.25	16.17	0.31	15.59	0.39	18.76	0.49
Abell 3120	10.59	0.27	12.67	0.36	11.72	0.44
Abell 3158	18.32	0.35	24.32	0.56	20.55	0.58	20.78	0.60
Abell 3266	27.98	0.28	35.52	0.44	31.49	0.59	32.32	0.61
Abell 3364	2.57	0.16	3.09	0.22	3.01	0.29	5.86	0.70
Abell 3376	17.49	0.50	21.86	0.73	19.39	0.84
Abell 3391	37.75	0.36	46.94	0.54	39.17	0.61	38.88	0.60
Abell 3395	23.90	0.40	29.92	0.59	24.56	0.62
Abell 3528S	51.40	0.40	63.21	0.57	54.18	0.73
Abell 3558	42.86	0.37	53.17	0.47	44.86	0.76
Abell 3562	26.50	0.42	32.02	0.55	27.91	0.72
Abell 3571	56.48	0.57	67.55	0.94	56.35	0.84
Abell 3581	91.59	0.97	111.17	1.12	93.04	1.65

Table 6—Continued

Name	Flux	Error	Flux	Error	Flux	Error	Flux	Error
Cluster Name	J (mJy)	J (mJy)	H (mJy)	H (mJy)	K (mJy)	K (mJy)	K24 (mJy)	K24 (mJy)
Abell 3667	26.10	0.38	32.59	0.51	27.58	0.62
Abell 3822	10.67	0.31	13.65	0.43	12.44	0.44
Abell 3827	11.98	0.24	15.22	0.35	13.46	0.38
Abell 3921	10.29	0.27	12.53	0.36	12.48	0.41
Abell 4038	52.87	0.74	66.47	1.25	53.26	1.20
Abell 4059	33.92	0.37	42.73	0.55	36.95	0.64	32.37	0.55
Abell S0405	20.37	0.38	25.16	0.54	22.12	0.65
Abell S0592	1.38	0.14	1.48	0.20	1.76	0.22	2.98	0.59
AC 114	1.04	0.12	1.62	0.17	1.56	0.23	3.61	0.61
AWM7	246.13	1.14	293.96	1.71	236.70	1.64
CENTAURUS	846.43	9.05	784.14	11.56	671.20	10.08	147.71	2.69
CID 0072	35.35	0.51	44.73	0.78	36.12	0.90	27.69	0.54
CL J1226.9+3332
CYGNUS A	36.44	0.43	41.18	0.55	34.72	0.60	34.47	0.60
ESO 3060170	48.06	0.63	58.38	0.83	49.06	1.02
ESO 5520200	73.87	0.67	88.69	0.95	74.30	1.21
EXO 0422-086	45.35	0.39	53.84	0.54	43.04	0.80
HCG 0062	232.69	1.68	280.96	2.58	217.50	3.30	91.57	0.70
HCG 42	350.28	1.90	423.08	3.13	343.69	3.63	163.65	0.67
HERCULES A	2.03	0.13	2.43	0.19	3.10	0.21	5.92	0.51
HYDRA A	21.02	0.46	25.11	0.70	22.79	0.70	22.41	0.68
M49	4144.27	180.56	4195.07	236.24	3698.43	275.45	561.11	11.22
M87	3303.44	104.40	3559.22	146.49	2882.03	130.89	523.58	10.45
MACS J0011.7-1523
MACS J0035.4-2015	0.69	0.09	0.95	0.15	1.21	0.19
MACS J0159.8-0849
MACS J0242.5-2132
MACS J0257.1-2325
MACS J0257.6-2209	1.17	0.13	1.54	0.22	2.10	0.22
MACS J0308.9+2645	1.69	0.10	2.06	0.16	2.36	0.17
MACS J0329.6-0211
MACS J0417.5-1154
MACS J0429.6-0253	0.71	0.11	1.20	0.19	1.63	0.21
MACS J0520.7-1328	0.90	0.14	1.48	0.18	1.90	0.25
MACS J0547.0-3904
MACS J0717.5+3745
MACS J0744.8+3927
MACS J1115.2+5320
MACS J1115.8+0129
MACS J1131.8-1955	1.27	0.11	1.77	0.19	2.26	0.22
MACS J1149.5+2223
MACS J1206.2-0847
MACS J1311.0-0310
MACS J1621.3+3810

Table 6—Continued

Name Cluster Name	Flux J (mJy)	Error J (mJy)	Flux H (mJy)	Error H (mJy)	Flux K (mJy)	Error K (mJy)	Flux K24 (mJy)	Error K24 (mJy)
MACS J1931.8-2634
MACS J2049.9-3217
MACS J2211.7-0349	0.87	0.14	1.80	0.21	1.72	0.23	4.13	0.61
MACS J2214.9-1359
MACS J2228+2036
MACS J2229.7-2755	0.81	0.10	1.20	0.16	1.51	0.17
MACS J2245.0+2637	1.26	0.12	1.19	0.18	1.93	0.20
MKW3S	23.64	0.40	29.06	0.56	24.13	0.73
MKW 04	196.90	1.23	242.96	1.64	198.43	2.16	97.48	0.67
MKW 08	47.78	0.90	56.21	1.29	52.13	1.46
MS 0016.9+1609
MS 0116.3-0115	31.25	0.39	37.88	0.63	31.35	0.64
MS 0440.5+0204	5.85	0.19	6.85	0.25	6.86	0.27
MS 0451.6-0305
MS 0735.6+7421	1.37	0.11	1.61	0.19	1.83	0.20
MS 0839.8+2938	1.74	0.08	2.11	0.12	2.60	0.16	4.61	0.42
MS 0906.5+1110	2.86	0.15	3.19	0.21	3.73	0.26	7.08	0.68
MS 1006.0+1202	1.36	0.15	1.86	0.24	2.22	0.27
MS 1008.1-1224	1.33	0.14	1.55	0.21	1.69	0.26
MS 1455.0+2232	1.68	0.11	1.90	0.18	2.66	0.20	4.86	0.54
MS 2137.3-2353	1.09	0.09	1.22	0.13	1.68	0.16	2.58	0.42
MS J1157.3+5531	12.93	0.21	16.55	0.33	14.50	0.33
NGC 0507	256.60	1.42	285.59	2.38	247.06	2.11	117.08	0.52
NGC 4636	1948.19	87.98	2080.16	122.03	1687.71	135.74	263.45	7.02
NGC 5044	628.83	2.80	731.33	4.56	599.60	7.20	174.24	0.77
NGC 5813	891.14	35.99	867.64	38.30	733.94	64.40	183.53	8.86
NGC 5846	2430.17	52.65	2780.30	65.20	2181.73	16.18	267.15	0.71
OPHIUCHUS	192.74	1.47	186.81	1.90	135.70	1.71
PKS 0745-191	13.46	0.21	13.88	0.26	10.93	0.38	15.13	0.67
RBS 0461	52.87	0.63	58.47	0.84	43.29	1.24
RBS 0533	242.51	2.55	285.11	3.23	225.51	4.08
RBS 0797
RCS J2327-0204
RXCJ0331.1-2100	5.82	0.12	6.60	0.18	5.43	0.22	7.98	0.59
RXC J1023.8-2715	2.07	0.20	1.94	0.24	2.39	0.36
RX J0220.9-3829	1.25	0.11	1.36	0.16	1.51	0.19
RX J0232.2-4420
RX J0439+0520	2.26	0.14	2.54	0.22	3.37	0.25	5.36	0.66
RX J0439.0+0715	0.95	0.12	1.61	0.20	1.77	0.18
RX J0528.9-3927
RX J0647.7+7015
RX J0819.6+6336	6.99	0.14	8.65	0.21	8.44	0.23
RX J1000.4+4409
RX J1022.1+3830	16.97	0.33	20.76	0.54	17.50	0.54

Table 6—Continued

Name Cluster Name	Flux J (mJy)	Error J (mJy)	Flux H (mJy)	Error H (mJy)	Flux K (mJy)	Error K (mJy)	Flux K24 (mJy)	Error K24 (mJy)
RX J1130.0+3637	5.59	0.26	6.51	0.42	6.19	0.42
RX J1320.2+3308	25.95	0.41	32.15	0.55	27.38	0.71
RX J1347.5-1145
RX J1423.8+2404
RX J1504.1-0248	2.21	0.14	3.24	0.19	3.15	0.28	3.35	0.73
RX J1532.9+3021
RX J1539.5-8335	15.68	0.34	18.99	0.48	14.88	0.57
RX J1720.1+2638	2.77	0.12	3.47	0.16	3.54	0.19	7.01	0.49
RX J1720.2+3536
RX J1852.1+5711	3.26	0.16	3.99	0.22	3.92	0.31
RX J2129.6+0005	1.69	0.12	2.50	0.21	2.56	0.22	3.97	0.57
SC 1327-312	14.98	0.33	17.95	0.43	16.60	0.67
SERSIC 159-03	16.16	0.29	20.03	0.42	17.17	0.53	17.41	0.54
SS2B153	177.24	1.12	216.72	1.60	171.39	2.00
UGC 03957	65.94	0.53	80.20	0.86	67.14	0.80
UGC 12491	98.34	1.12	110.16	1.91	90.98	2.07
ZWCL 1215	9.87	0.27	12.11	0.38	11.57	0.52
ZWCL 1358+6245
ZWCL 1742	8.36	0.20	9.68	0.34	9.41	0.32	11.54	0.42
ZWCL 1953	0.71	0.10	1.35	0.18	1.13	0.17
ZWCL 3146	1.05	0.14	1.78	0.21	1.51	0.25	3.84	0.66
ZWICKY 2701	1.47	0.13	1.64	0.23	2.22	0.21	3.90	0.56
ZwCl 0857.9+2107	0.76	0.10	0.92	0.13	1.40	0.17	2.81	0.44

Table 7. Star Formation Rates:

Name	SFR	Error	SFR	SFR	Error	SFR	Error	Mass
Cluster Name	UV	UV	IR	$70\mu m$	$70\mu m$	$24\mu m$	$24\mu m$	Stellar Mass
	$(M_{\odot} \text{ yr}^{-1})$	$(M_{\odot} \text{ yr}^{-1})$	$(M_{\odot} \text{ yr}^{-1})$	$(M_{\odot} \text{ yr}^{-1})$	$(M_{\odot} \text{ yr}^{-1})$	$(M_{\odot} \text{ yr}^{-1})$	$(M_{\odot} \text{ yr}^{-1})$	$(10^{10} M_{\odot})$
1E0657 56a	2.12	5.22	0	0.91	0.11	5.52
1E0657 56b	1.64	1.65	0	0.76	0.12	6.68
2A 0335+096	0.72	0.94	0.25	0.21	0.02	5.58
2PIGG J0011.5-2850	0.92	0
2PIGG J2227.0-3041	1.82	0.33
3C 28.0	2.30	0.37	13.51	2.15	0	2.05	0.29	4.40
3C 295
3C 388	1.14	0	1.78	1.61	0.36	1.47	0.15	7.06
4C 55.16
Abell 13
Abell 68
Abell 85	0.90	0	0.61	0.70	0.16	0.36	0.04	6.72
Abell 119	0.57	0
Abell 133	0.69	0
Abell 141
Abell 160	0.40	0
Abell 193
Abell 209	2.04	0.91	0.12	7.91
Abell 222
Abell 223
Abell 262	0.16	0	0.12	0.39	0.10	0.08	0.01	3.50
Abell 267	2.86	0	5.01	0.69	0.27	9.84
Abell 368
Abell 370	5.96	2.86	0	1.19	0.47	14.39
Abell 383	2.40	0	5.58	1.65	0.18	8.03
Abell 399
Abell 400	0.32	0
Abell 401	1.10	0	0
Abell 426	7.11	0.10	34.46	12.16	2.43	69.99	7.00	6.66

Table 7—Continued

Name	SFR	Error	SFR	SFR	Error	SFR	Error	Mass
Cluster Name	UV	UV	IR	70 μm	70 μm	24 μm	24 μm	Stellar Mass
	($M_{\odot} \text{ yr}^{-1}$)	($M_{\odot} \text{ yr}^{-1}$)	($M_{\odot} \text{ yr}^{-1}$)	($M_{\odot} \text{ yr}^{-1}$)	($M_{\odot} \text{ yr}^{-1}$)	($M_{\odot} \text{ yr}^{-1}$)	($M_{\odot} \text{ yr}^{-1}$)	($10^{10} M_{\odot}$)
Abell 478	2.39	2.15	0.44	0.98	0.10	7.84
Abell 496
Abell 520
Abell 521
Abell 539	0.15	0.04
Abell 562
Abell 576
Abell 586
Abell 611
Abell 644	0.33	0
Abell 665
Abell 697	4.17	0	13.33	1.58	0.16	13.70
Abell 744	0.65	0
Abell 754
Abell 773	3.64	1.25	0.16	8.17
Abell 907
Abell 963	2.70	0
Abell 1060	0.10	0
Abell 1063S	0.40	0.82	0.13	17.78
Abell 1068	2.60	0.60	93.15	159.87	32.12	119.39	11.94	6.08
Abell 1201
Abell 1204	0.76	0	4.44	8.10	1.68	3.72	0.40	4.27
Abell 1240
Abell 1361	3.21	2.06	0.44	0.73	0.08	4.94
Abell 1413	2.32	0
Abell 1423
Abell 1446	0.76	0
Abell 1569	0.36	0
Abell 1576

Table 7—Continued

Name	SFR	Error	SFR	SFR	Error	SFR	Error	Mass
Cluster Name	UV	UV	IR	70 μm	70 μm	24 μm	24 μm	Stellar Mass
	($M_{\odot} \text{ yr}^{-1}$)	($M_{\odot} \text{ yr}^{-1}$)	($M_{\odot} \text{ yr}^{-1}$)	($M_{\odot} \text{ yr}^{-1}$)	($M_{\odot} \text{ yr}^{-1}$)	($M_{\odot} \text{ yr}^{-1}$)	($M_{\odot} \text{ yr}^{-1}$)	($10^{10} M_{\odot}$)
Abell 1644	0.63	0
Abell 1650
Abell 1651
Abell 1664	16.13	0.27	10.00	11.53	3.12	5.80	0.58	4.90
Abell 1689	10.88	0.82	0	2.17	0.22	6.27
Abell 1736	0.23	0
Abell 1758	3.28	0.93	0.13	8.51
Abell 1763	1.06	0	7.68	2.26	0	1.14	0.34	4.18
Abell 1795	2.39	0.20
Abell 1835	23.56	1.07	235.37	134.96	27.86	97.17	9.72	15.03
Abell 1914	0.58	0	0.35	0.31	0.04	3.89
Abell 1942
Abell 1991	0.56	0
Abell 1995	2.36	0
Abell 2029	1.72	0
Abell 2034
Abell 2052	0.41	0	0.34	0.54	0.11	0.47	0.05	4.89
Abell 2063	0.31	0
Abell 2065	0.35	0
Abell 2069
Abell 2104
Abell 2107	0.57	0
Abell 2111	2.17	0
Abell 2124	0.76	0
Abell 2125
Abell 2142	0.77	0
Abell 2147	0.35	0
Abell 2151	0.38	0
Abell 2163

Table 7—Continued

Name	SFR	Error	SFR	SFR	Error	SFR	Error	Mass
Cluster Name	UV	UV	IR	70 μm	70 μm	24 μm	24 μm	Stellar Mass
	($M_{\odot} \text{ yr}^{-1}$)	($M_{\odot} \text{ yr}^{-1}$)	($M_{\odot} \text{ yr}^{-1}$)	($M_{\odot} \text{ yr}^{-1}$)	($M_{\odot} \text{ yr}^{-1}$)	($M_{\odot} \text{ yr}^{-1}$)	($M_{\odot} \text{ yr}^{-1}$)	($10^{10} M_{\odot}$)
Abell 2187	1.87	0
Abell 2199	0.49	0	0.58	0.35	0.03	6.35
Abell 2204	6.06	10.27	2.14	4.55	0.46	5.68
Abell 2218
Abell 2219	1.17	1.23	0.14	6.85
Abell 2244
Abell 2255	0.28	0
Abell 2256	0.56	0
Abell 2259
Abell 2261	9.99	1.54	0	1.58	0.17	13.54
Abell 2294
Abell 2319
Abell 2384
Abell 2390	8.53	0.86	40.60	20.76	5.35	6.14	0.62	7.20
Abell 2409
Abell 2420
Abell 2462	0.64	0
Abell 2537
Abell 2554	0.82	0
Abell 2556	0.70	0
Abell 2589	0.47	0
Abell 2597	2.52	0.19	3.23	3.31	1.00	1.37	0.15	3.90
Abell 2626	0.67	0	0.92	0.34	0	0.32	0.03	5.34
Abell 2631
Abell 2657
Abell 2667	2.32	0.68	75.94	31.97	3.20	4.84
Abell 2717	0.41	0
Abell 2744a	36.16	4.88	0	2.31	0.25	7.94
Abell 2744b

Table 7—Continued

Name	SFR	Error	SFR	SFR	Error	SFR	Error	Mass
Cluster Name	UV	UV	IR	70 μm	70 μm	24 μm	24 μm	Stellar Mass
	($M_{\odot} \text{ yr}^{-1}$)	($M_{\odot} \text{ yr}^{-1}$)	($M_{\odot} \text{ yr}^{-1}$)	($M_{\odot} \text{ yr}^{-1}$)	($M_{\odot} \text{ yr}^{-1}$)	($M_{\odot} \text{ yr}^{-1}$)	($M_{\odot} \text{ yr}^{-1}$)	($10^{10} M_{\odot}$)
Abell 2813
Abell 3084	0.64	0
Abell 3088
Abell 3112	0.90	0	2.27	0.51	0	1.26	0.13	5.53
Abell 3120	0.55	0
Abell 3158	0.60	0
Abell 3266	0.98	0
Abell 3364
Abell 3376	0.29	0
Abell 3391	0.54	0.13	0	0.42	0.04	9.12
Abell 3395
Abell 3528S	1.21	0
Abell 3558	0.82	0
Abell 3562	0.44	0
Abell 3571
Abell 3581	0.21	0
Abell 3667
Abell 3822	0.74	0
Abell 3827	1.70	0
Abell 3921	1.31	0
Abell 4038
Abell 4059	0.66	0	0.57	0.47	0.11	0.31	0.03	6.04
Abell S0405	0.73	0
Abell S0592
AC 114	4.62	0.95	0.10	12.25
AWM7	0.24	0
CENTAURUS	0.16	0	0.18	0.34	0.08	0.23	0.03	6.22
CID 0072	0.27	0	0.26	0.17	0	0.10	0.01	3.21
CL J1226.9+3332	132.54	26.75	0	3.41	0.51	28.97

Table 7—Continued

Name	SFR	Error	SFR	SFR	Error	SFR	Error	Mass
Cluster Name	UV	UV	IR	70 μm	70 μm	24 μm	24 μm	Stellar Mass
	($M_{\odot} \text{ yr}^{-1}$)	($M_{\odot} \text{ yr}^{-1}$)	($M_{\odot} \text{ yr}^{-1}$)	($M_{\odot} \text{ yr}^{-1}$)	($M_{\odot} \text{ yr}^{-1}$)	($M_{\odot} \text{ yr}^{-1}$)	($M_{\odot} \text{ yr}^{-1}$)	($10^{10} M_{\odot}$)
CYGNUS A	95.04	31.23	6.27	167.24	16.72	7.56
ESO 3060170	0.39	0
ESO 5520200	0.40	0
EXO 0422-086	0.40	0.09
HCG 0062	1.07	0.14	0	0.21	0.02	3.56
HCG 42	0.24	0	0.32	0.06	0	0.16	0.02	4.47
HERCULES A	1.34	0	1.17	0.40	0.06	4.32
HYDRA A	2.62	0.19	3.77	3.08	0.73	2.13	0.21	4.88
M49	0.06	0	0.58	0.08	0.02	0.76	0.08	2.98
M87	0.10	0	0.24	0.18	0.04	0.37	0.04	4.55
MACS J0011.7-1523
MACS J0035.4-2015
MACS J0159.8-0849
MACS J0242.5-2132
MACS J0257.1-2325
MACS J0257.6-2209
MACS J0308.9+2645
MACS J0329.6-0211
MACS J0417.5-1154
MACS J0429.6-0253
MACS J0520.7-1328
MACS J0547.0-3904
MACS J0717.5+3745
MACS J0744.8+3927
MACS J1115.2+5320
MACS J1115.8+0129
MACS J1131.8-1955
MACS J1149.5+2223
MACS J1206.2-0847

Table 7—Continued

Name	SFR	Error	SFR	SFR	Error	SFR	Error	Mass
Cluster Name	UV	UV	IR	$70\mu m$	$70\mu m$	$24\mu m$	$24\mu m$	Stellar Mass
	$(M_{\odot} \text{ yr}^{-1})$	$(M_{\odot} \text{ yr}^{-1})$	$(M_{\odot} \text{ yr}^{-1})$	$(M_{\odot} \text{ yr}^{-1})$	$(M_{\odot} \text{ yr}^{-1})$	$(M_{\odot} \text{ yr}^{-1})$	$(M_{\odot} \text{ yr}^{-1})$	$(10^{10} M_{\odot})$
MACS J1311.0-0310
MACS J1621.3+3810
MACS J1931.8-2634
MACS J2049.9-3217
MACS J2211.7-0349
MACS J2214.9-1359
MACS J2228+2036
MACS J2229.7-2755	6.95	1.36
MACS J2245.0+2637
MKW3S	0.37	0
MKW 04	0.33	0	0.03	0.10	0	0.10	0.01	5.66
MKW 08	0.19	0
MS 0016.9+1609
MS 0116.3-0115	0.48	0
MS 0440.5+0204
MS 0451.6-0305	8.09	7.63	0	2.79	0.42	11.00
MS 0735.6+7421	1.51	0
MS 0839.8+2938	1.20	0
MS 0906.5+1110
MS 1006.0+1202
MS 1008.1-1224
MS 1455.0+2232	5.90	0.86	9.46	3.16	0.47	10.86
MS 2137.3-2353	3.09	0	18.49	3.73	0.84	10.96
MS J1157.3+5531	0.69	0
NGC 0507	0.26	0	0.29	0.05	0	0.17	0.02	4.83
NGC 4636	0.02	0	-0.01	0.07	0.02	0.02	0	1.38
NGC 5044	0.12	0	0.27	0.23	0.05	0.19	0.02	3.61
NGC 5813	0.07	0	0.04	0.11	0.04	0.10	0.01	2.40
NGC 5846	0.08	0	0.14	0.17	0.04	0.14	0.01	4.78

Table 7—Continued

Name	SFR	Error	SFR	SFR	Error	SFR	Error	Mass
Cluster Name	UV	UV	IR	70 μm	70 μm	24 μm	24 μm	Stellar Mass
	($M_{\odot} \text{ yr}^{-1}$)	($M_{\odot} \text{ yr}^{-1}$)	($M_{\odot} \text{ yr}^{-1}$)	($M_{\odot} \text{ yr}^{-1}$)	($M_{\odot} \text{ yr}^{-1}$)	($M_{\odot} \text{ yr}^{-1}$)	($M_{\odot} \text{ yr}^{-1}$)	($10^{10} M_{\odot}$)
OPHIUCHUS	2.60	0.10
PKS 0745-191	17.81	11.52	2.57	8.50	0.85	9.51
RBS 0461
RBS 0533	0.14	0
RBS 0797
RCS J2327-0204
RXCJ0331.1-2100
RXC J1023.8-2715	0.35	0.08
RX J0220.9-3829
RX J0232.2-4420
RX J0439+0520	9.93	7.35	1.54	7.57	0.83	8.79
RX J0439.0+0715
RX J0528.9-3927
RX J0647.7+7015
RX J0819.6+6336
RX J1000.4+4409
RX J1022.1+3830	0.34	0
RX J1130.0+3637	0.20	0
RX J1320.2+3308
RX J1347.5-1145
RX J1423.8+2404
RX J1504.1-0248	56.50	0.46
RX J1532.9+3021	227.52	110.14	22.03	43.54	4.35	9.33
RX J1539.5-8335
RX J1720.1+2638	2.67	0.68
RX J1720.2+3536
RX J1852.1+5711
RX J2129.6+0005	2.09	0	5.58	4.71	0	5.15	0.51	8.61
SC 1327-312	0.37	0

Table 7—Continued

Name	SFR	Error	SFR	SFR	Error	SFR	Error	Mass
Cluster Name	UV	UV	IR	70 μm	70 μm	24 μm	24 μm	Stellar Mass
	($M_{\odot} \text{ yr}^{-1}$)	($M_{\odot} \text{ yr}^{-1}$)	($M_{\odot} \text{ yr}^{-1}$)	($M_{\odot} \text{ yr}^{-1}$)	($M_{\odot} \text{ yr}^{-1}$)	($M_{\odot} \text{ yr}^{-1}$)	($M_{\odot} \text{ yr}^{-1}$)	($10^{10} M_{\odot}$)
SERSIC 159-03	0.52	0	0.89	0.67	0.15	0.30	0.03	4.21
SS2B153	0.28	0
UGC 03957	0.49	0
UGC 12491
ZWCL 1215
ZWCL 1358+6245	2.86	1.73	0.26	5.36
ZWCL 1742	2.02	1.52	0.32	1.45	0.15	3.80
ZWCL 1953
ZWCL 3146	20.86	1.05	65.51	34.09	10.32	31.28	3.13	9.98
ZWICKY 2701	0.97	2.91	0	0.57	0.14	6.32
ZwCl 0857.9+2107	5.93	0.55	428.41	96.25	19.25	164.99	16.50	2.56

Note. — A star formation rate uncertainty of 0 identifies the quoted rate as a 3σ upper limit.

Note. — UV SFR are calculated for all objects, including those in high K_0 systems. Upper limits are then calculated using the uncertainties on the NUV, K, and inert BCG color. If a star formation rate is consistent with a SFR of zero within 3σ , a 3σ upper limit is reported.

Note. — The IR SFR is estimated by a fit to the Groves et al. (2008) models. The 24 and 70 micron SFRs are estimated from empirical relationships reported in Calzetti et al. (2010) and the uncertainties are calculated using the 24 and 70 micron flux uncertainties, respectively.

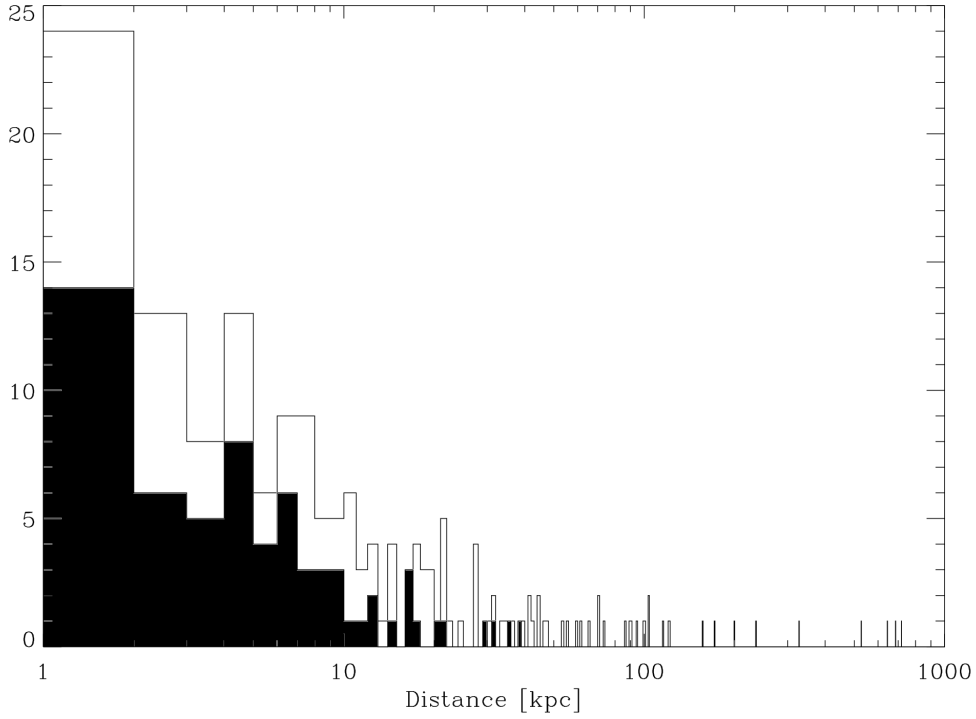


Fig. 1.— The projected physical distance, in $\text{kpc } h_{70}^{-1}$, between X-ray centroid and the BCG we identified. All BCGs with an RA and Dec, not just those with *GALEX* and *Spitzer* data are plotted here. The shaded region highlights BCGs in low K_0 clusters. In high central entropy systems, 37% of BCGs lie within 10 kpc of the X-ray centroid, while the percentage is increased to 74% for low central entropy systems. All BCGs which lie greater than 40 kpc away from their X-ray centroid are in high K_0 clusters.

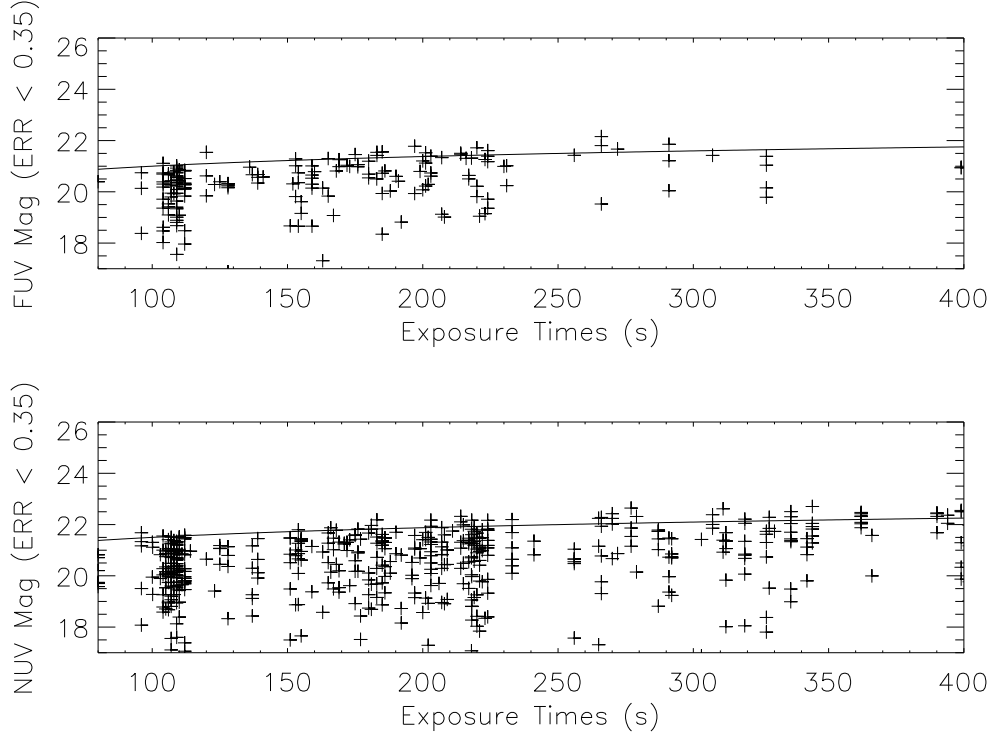


Fig. 2.— The UV magnitudes (AB scale) for all UV sources within $1'$ of the BCG locations (regardless of identity) with flux uncertainties less than 0.35 magnitudes. The upper envelope of this distribution serves as a basis for estimating the upper limit fluxes for undetected or poorly-detected BCGs for exposure times less than 400 seconds: $FUV_{UL} = 18.5 + 1.25 \log_{10} t$ and $NUV_{UL} = 19.0 + 1.25 \log_{10} t$. We considered all *GALEX* detections with magnitude errors > 0.35 to be poorly detected.

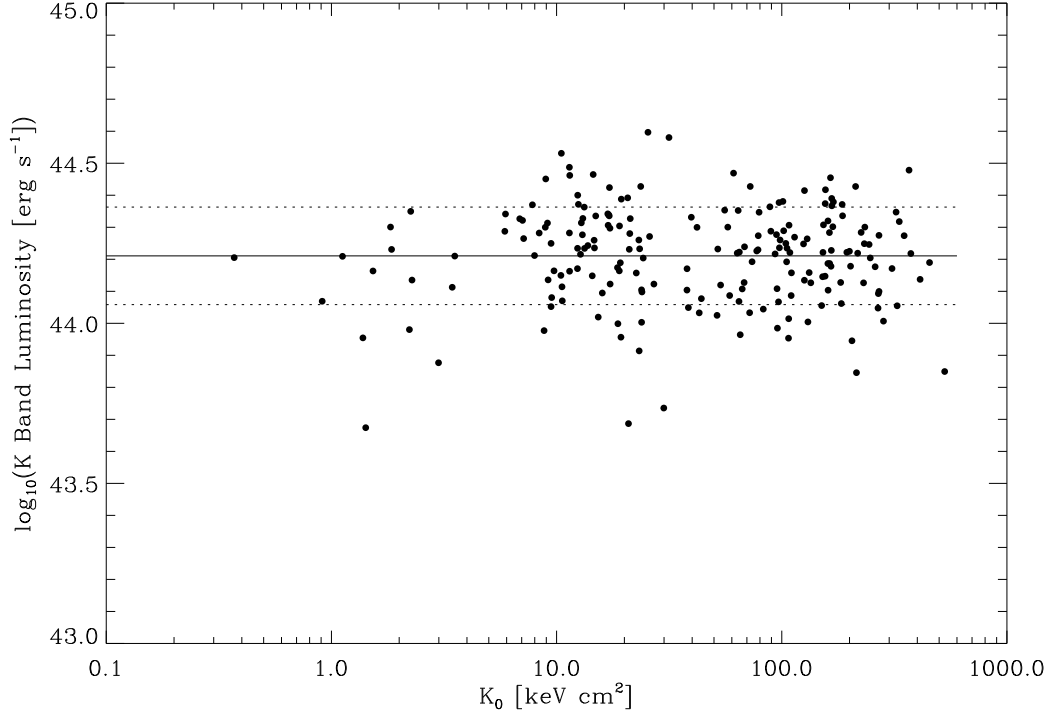


Fig. 3.— The logarithm of K band luminosity and central entropy of the cluster. The K band luminosity is calculated from the flux inside $14.3 \text{ kpc } h_{70}^{-1} \text{ kpc}$ radius. The luminosities are k-corrected assuming passive evolution. The solid horizontal line represents the mean ($1.6 \times 10^{44} \text{ erg s}^{-1} h_{70}^{-2}$) of the data points while the dotted lines are the 1σ error ($+0.7 \times 10^{44} \text{ erg s}^{-1} h_{70}^{-2}$, $-0.4 \times 10^{44} \text{ erg s}^{-1} h_{70}^{-2}$) on the mean.

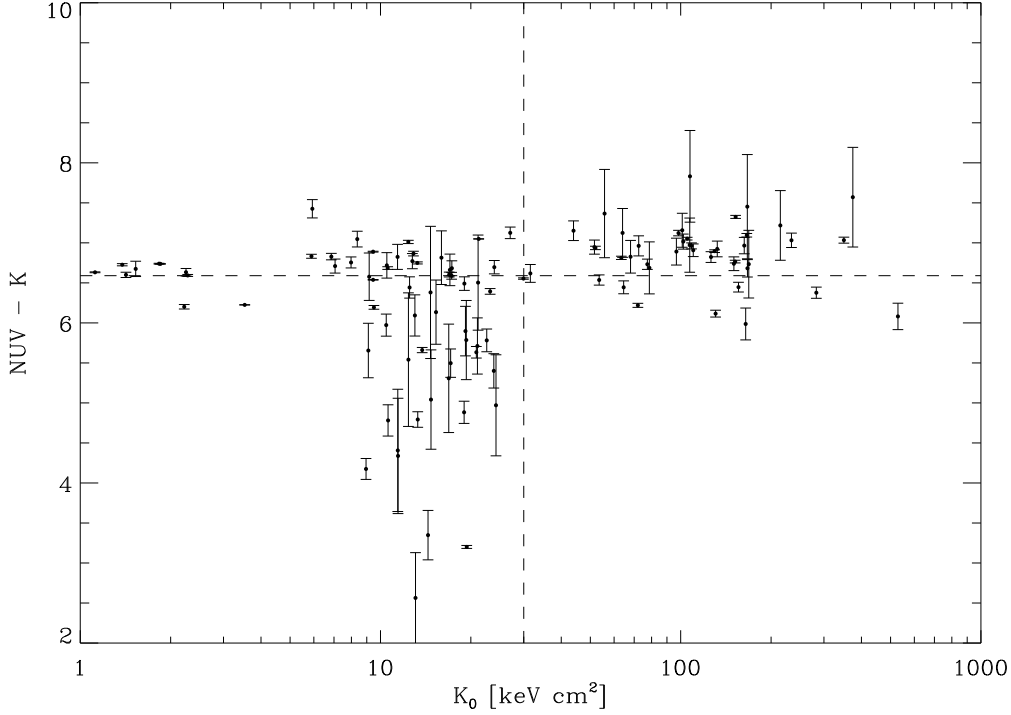


Fig. 4.— NUV-K as a function of cluster central entropy. The vertical dashed line is at 30 keV cm^2 , our cutoff for the definition of low entropy clusters. Note the large color distribution for low K_0 objects, while the high entropy objects have a more consistent redder color. The K band fluxes have been k-corrected assuming passive evolution. The horizontal dashed line represents a NUV-K color of 6.59 magnitudes, the mean of the BCGs in clusters with $K_0 \leq 30 \text{ keV cm}^2$. There may appear to be a trend with the low entropy objects, but this is a selection effect where the lowest entropy objects that are observed are also the nearest objects.

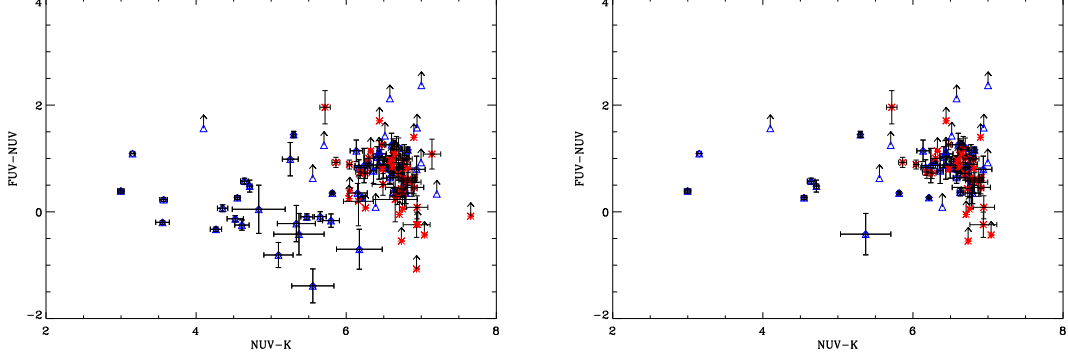


Fig. 5.— FUV-NUV and NUV-K colors. The blue triangles are BCGs in low K_0 clusters ($\leq 30 \text{ keV cm}^2$) while the red asterisks are BCGs in high entropy clusters. The left plot includes all of the BCGs while the right plot only includes nearby ($z < 0.15$) BCGs demonstrating that the bluest FUV-NUV colors, in the left hand plot, are likely arising because of contributions from $\text{Ly}\alpha$.

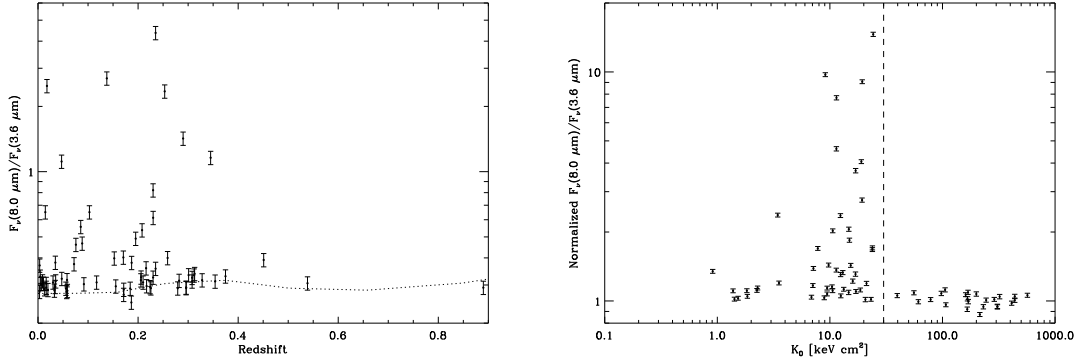


Fig. 6.— Redshift dependence of 8.0 μm to 3.6 μm ratio. The dotted line represents the expected flux ratio for passively evolving stellar population that is 10 Gyr at $z = 0$. While IRS spectra of $\text{H}\alpha$ -emitting BCGs show PAH features that would fall in the 8.0 micron bandpass (e.g. Donahue et al. 2011) the observed IRAC 8.0 micron color is sensitive to only strong PAH features. On the right, the flux ratio has been normalized by the passive evolution model and is plotted against the central entropy of the cluster. The dotted line identifies the threshold 30 keV cm^2 . There appears to be a deficit of excess-IR emitters in the low K_0 clusters, but this deficit is likely to be a selection effect since low K_0 can only be resolved in the most nearby groups.

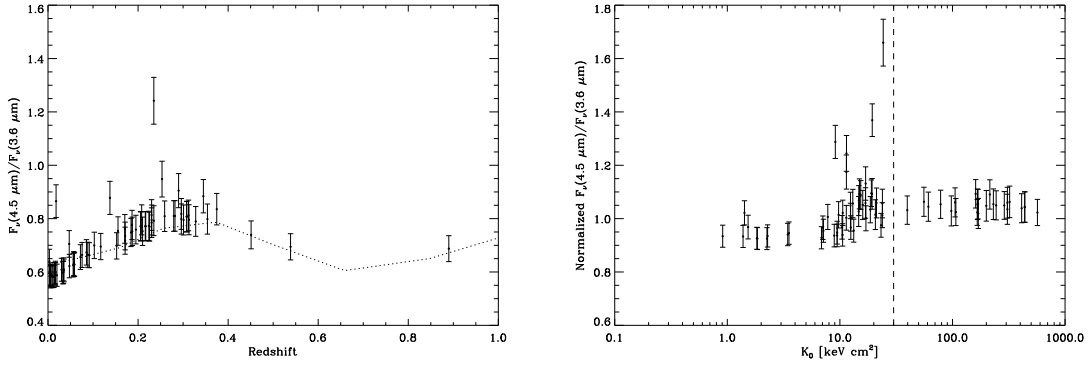


Fig. 7.— The left hand figure shows the flux ratio between the $4.5 \mu\text{m}$ and the $3.6 \mu\text{m}$ flux is plotted as a function of redshift. The dotted line indicates a Starburst99 model for a passively evolving elliptical galaxy with a primarily old stellar population dominated by red giants, with an age of about 10 Gyr at $z = 0$. For most of the BCGs the IRAC $4.5 \mu\text{m}$ to $3.6 \mu\text{m}$ colors are consistent with those of a passively evolving population. In the figure on the right, the flux ratio has been normalized by the passive evolution model and is plotted against the central entropy of the cluster. The dotted line again identifies $K_0 = 30 \text{ keV cm}^2$. It is interesting that the handful of BCGs (Abell 426, Abell 1068, Abell 1835, and ZwCl 0857.9+2107) with large excess 4.5 micron emission are located only in clusters with K_0 less than the threshold.

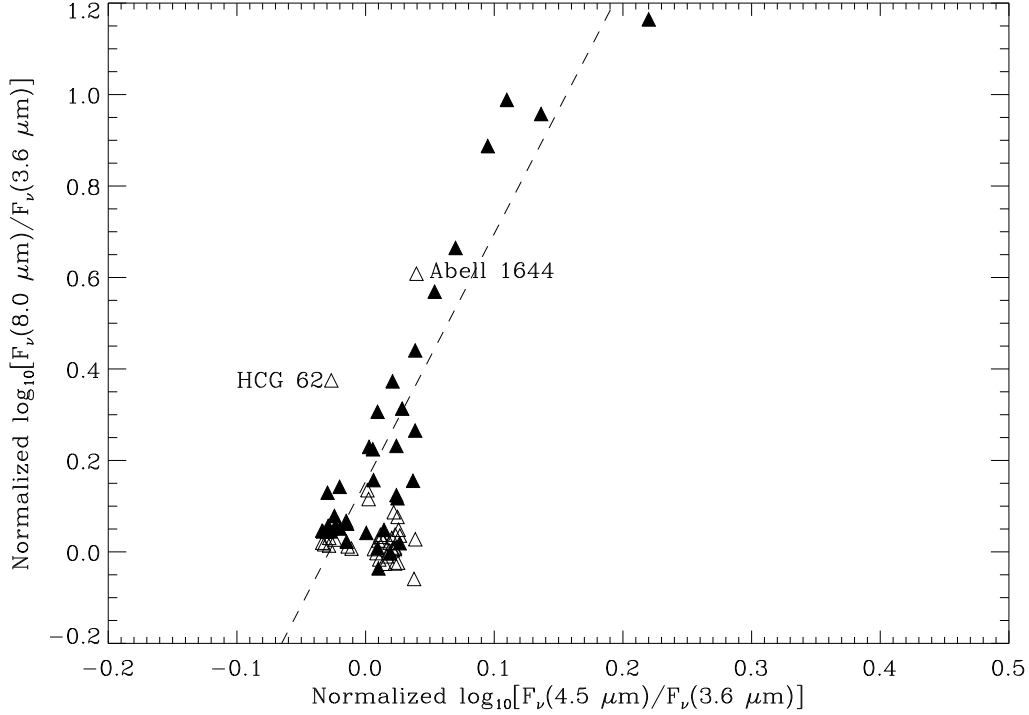


Fig. 8.— 8.0 micron to 3.6 micron ratio and 4.5 micron to 3.6 micron ratio. Both ratios have been normalized for passive evolution. The 8.0/3.6 and the 4.5/3.6 ratios are strongly correlated ($r = 0.92(15\sigma)$) for objects with mid-IR detections and/or NUV-K excesses (shown as filled in triangles), which is expected if the excess 4.5 micron emission is generated by processes related to that producing the 8.0 micron emission. Dashed line is a fit to the data; see text. Abell 1644 and HCG 62 do not have blue NUV-K colors, HCG 62 is a 70 micron upper limit, and Abell 1644 wasn't observed by MIPS. Since these ratios use only IRAC data, the uncertainties in the absolute flux calibration are not included. As long as the IRAC calibration was consistent over time, these are precise relative flux ratios. The absolute flux ratios are accurate to about 2%.

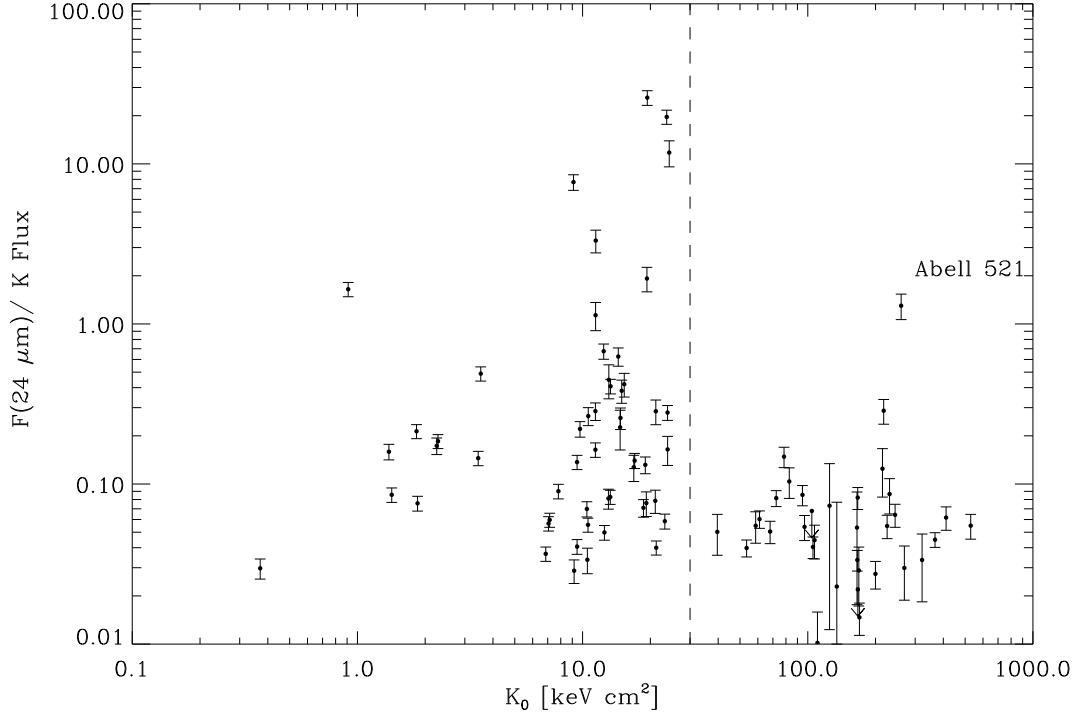


Fig. 9.— 24 micron flux to K band flux ratio with central entropy of the cluster. BCGs with excess 24 micron flux inhabit clusters with low K_0 , with the exception of Abell 521. Even though it is a high K_0 cluster, the BCG in Abell 521 is in a low entropy, compact, X-ray corona (i.e. a “mini-cooling core”) which can be associated with BCGs with radio sources and star-formation activity, like BCGs in low K_0 clusters of galaxies (Ferrari et al. 2006).

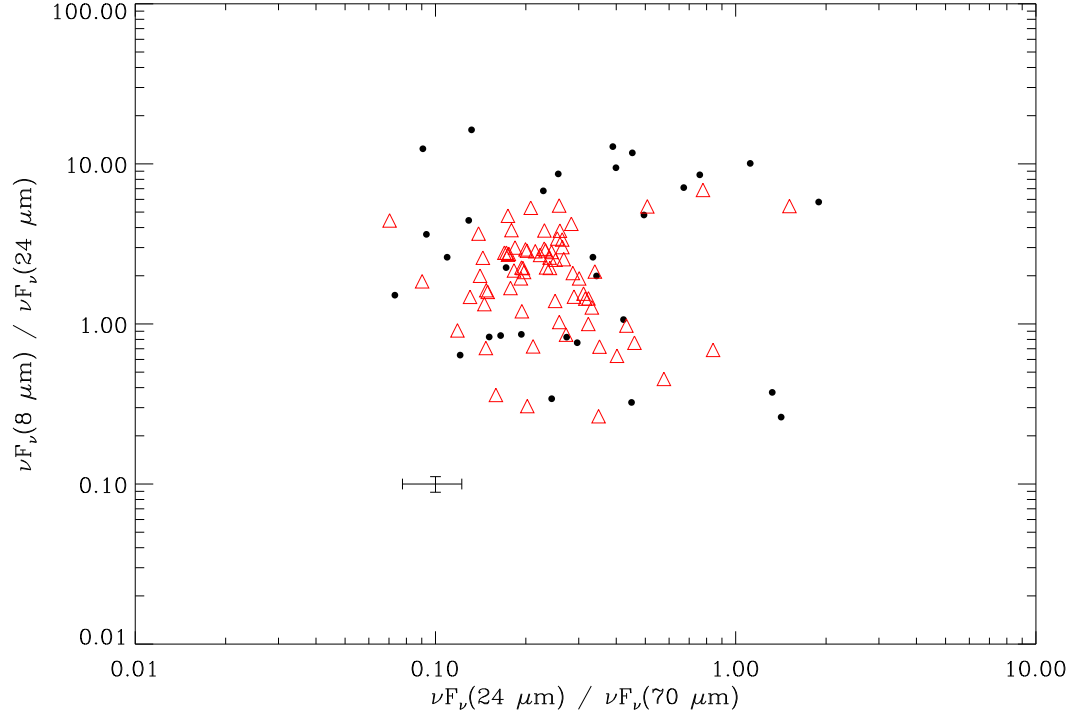


Fig. 10.— Mid IR flux ratio comparison with SINGS galaxies. This plot is similar to Figure 1 in Johnson et al. (2007a). The black dots are our BCGs and the SINGS galaxies (Kennicutt et al. 2003) are overplotted as red triangles. Ratios for objects with MIPS upper limits at 24 or 70 microns are not plotted but are consistent with the distribution of the detected galaxies. An error bar, representing the standard IRAC and MIPS systematic errors, is plotted to represent a typical error bar. Some nearby BCGs have slightly higher 8.0/24 micron flux ratios than SINGS galaxies, but similar 24/70 micron flux ratios.

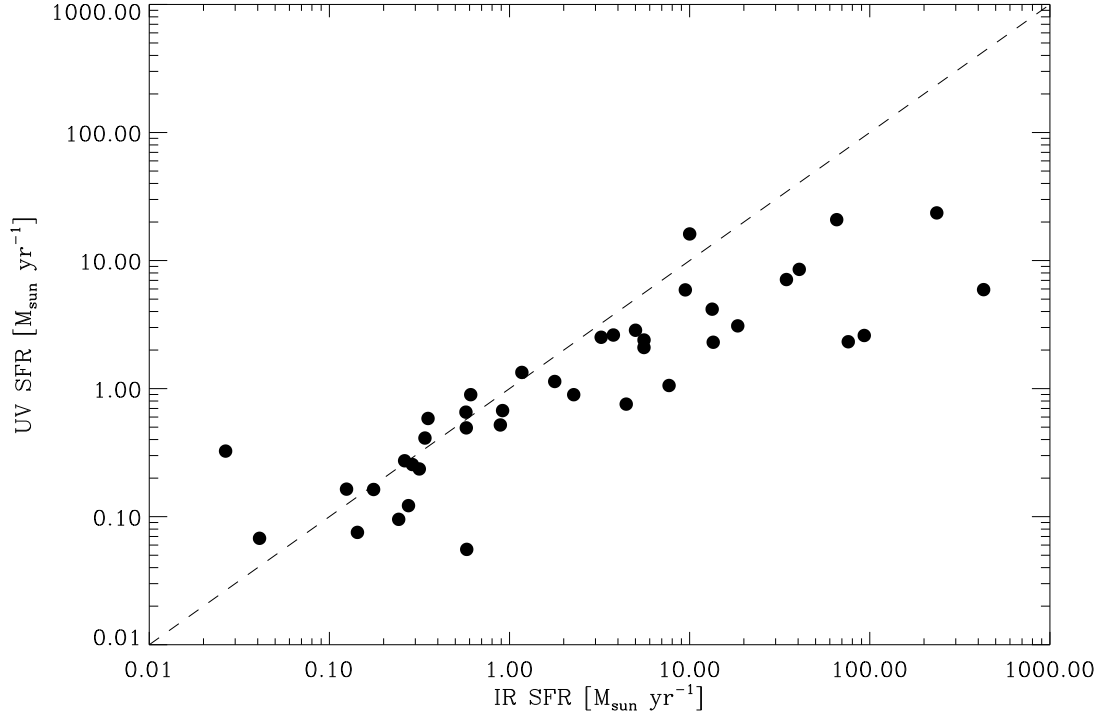


Fig. 11.— UV and IR SFR. The dotted line represents a line of unity. The UV SFR assumes a constant rate of star formation. The model-derived IR star formation rates are consistent with star formation rates measured with a MIPS $70 \mu\text{m}$ SFR estimate as shown in Figure 12. Those objects which fall below the line, BCGs with excess IR star formation, are similar to starburst galaxies, in the sense that for the most luminous star-forming galaxies, most of the star-formation is obscured.

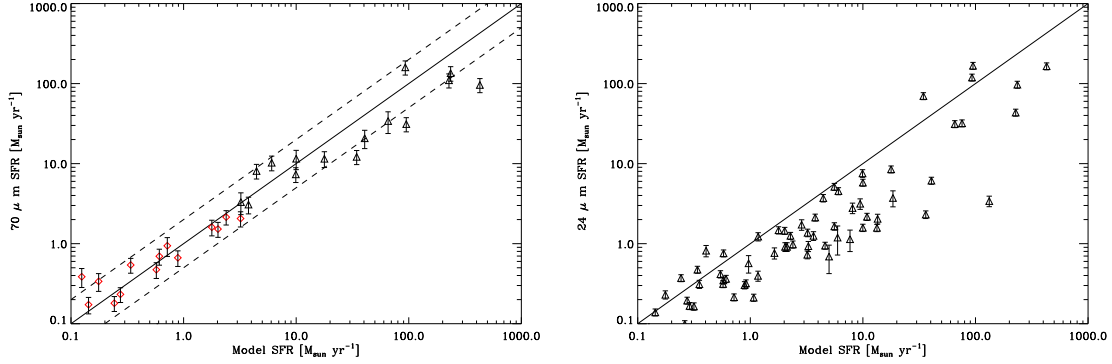


Fig. 12.— Comparison of model IR SFR to single band IR SFR. We compare the estimates from the Groves model star formation rates to the star formation rate estimates using the 70 micron luminosity in the left plot. The line represents a line of unity, not a fit. The dotted lines represent the boundary for a difference of a factor of two in star formation rate. The black triangles represent the high luminosity relation given in Calzetti et al. (2010) while the red diamonds use their relation for galaxies with low IR luminosities (and therefore a larger amount of the IR flux is produced by dust heated by evolved stars rather than hot stars). The right plot is a similar plot relating the 24 micron luminosity to the Groves model star formation rates. The 24 micron SFRs tend to have lower estimates as the 70 micron luminosities are found nearer to the peak of the dust blackbody and therefore more representative of the total IR luminosity and SFR. For the most luminous 70 microns galaxies, it appears that the model fit tends to overpredict the SFR and luminosity relative to the 70 micron flux estimate.

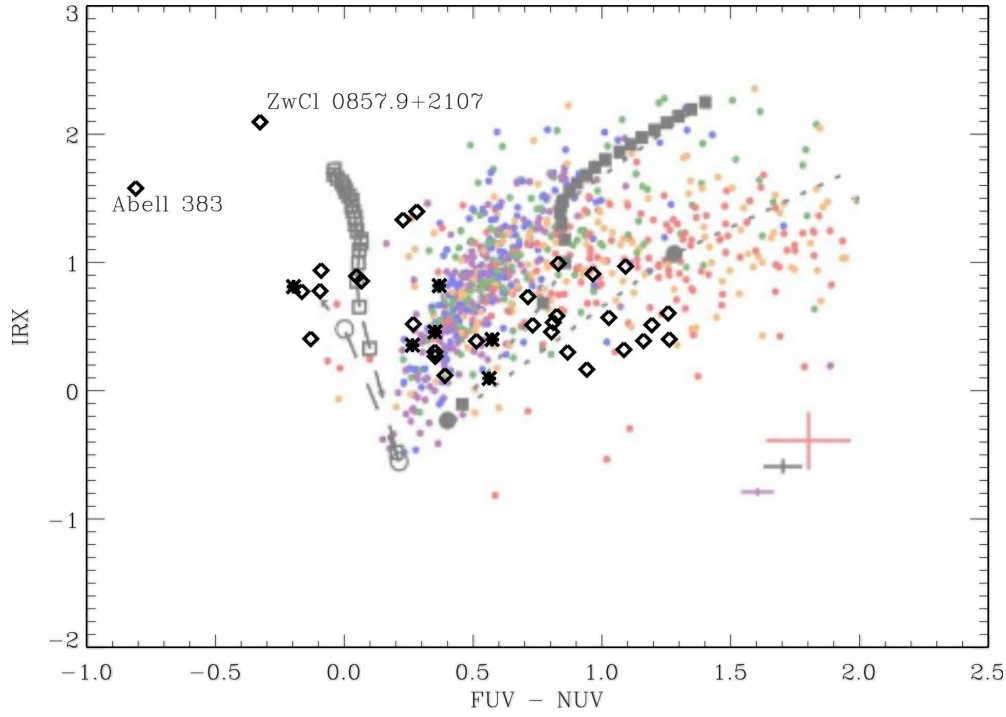


Fig. 13.— IR excess and UV color. The IR excess (IRX) is defined in Johnson et al. (2007a) to be the ratio of IR to UV luminosity. Objects from the cool core sample of Hicks et al. (2010) are marked with X's. Figure 6a from Johnson et al. (2007a) is plotted in the background on this graph.

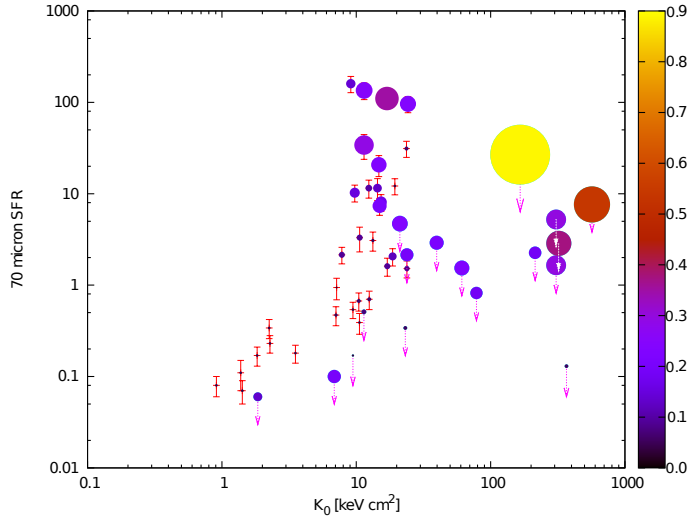


Fig. 14.— Relation between 70 micron SFR and central entropy. The objects are color coded and sized based on redshift (i.e. higher redshift, larger size). The color code ranges from redshift of 0.0 to 0.9. The “trend” that is seen in the lowest central entropy clusters is not a physical trend, but it is the same selection effect noted in Figure 4. Note that all BCGs in clusters with $K_0 > 30 \text{ keV cm}^2$ in this plot have only upper limits.